博士論文

Electron temperature and density profile measurement in spherical tokamaks started-up by radio frequency waves

（高周波波動で立ち上げられた球状トカマクにおける電子温度・密度分布計測）

冨樫 央

Abstract

In order to realize a fusion reactor, it is important to confine a plasma with high density and temperature for a long duration. Tokamak, which features high confinement performance, has been studied as a possible candidate of reactors. In particular, a spherical tokamak (ST) has high efficiency and stability in the plasma confinement. In conventional tokamaks, a central solenoid (CS) is used for the plasma current start-up. In STs, however, elimination of the CS or reduction in its size is necessary, and thus an alternative (non-inductive) start-up scenario must be established. Non-inductive start-up experiments using radio frequency (RF) waves have been performed successfully in conventional tokamaks. In order to demonstrate the RF start-up scenario in STs, experiments using electron cyclotron waves (ECWs) have been carried out in MAST, QUEST, LATE, and so on. Additionally, experiments using lower hybrid waves (LHWs) have been performed in TST-2 and Globus-M. However, high current drive efficiency such as that seen in the conventional tokamaks has not been obtained.

The objectives of this study is to develop two diagnostic systems to reveal the features of bulk and fast electrons, which play critical roles in RF start-up plasmas. We also aim at elucidating the characteristics peculiar to RF start-up plasmas by applying the developed systems to TST-2 and QUEST. In LHW-driven ST plasmas, profiles of electron temperature T_e and electron density n_e, which are fundamental plasma parameters, had not been measured. Then, a high-performance Thomson scattering (TS) diagnostic system has been developed to measure the profiles of TST-2 plasmas. We have also developed a scheme to measure the electron temperature anisotropy because it reflects the slowing down of fast electrons and the confinment of the bluk electrons. Information of hard X-ray (HXR) radiation is also important because it reflects absorption profile of LHWs and energy range and effective temperature of fast electrons generated by the LHWs. Thus an HXR diagnostics system is also developed. In QUEST, detail of the electron temperature and density profiles is investigated by upgrading the system.

While TS measurements on standard tokamak plasmas are not so difficult, the measurements becomes difficult in RF start-up ST plasmas because of their low densities and resultant weak signals. It was impossible to measure TST-2 LHW-driven plasmas by the previous TS system. In order to improve the signal-to-noise ratio (SNR), two schemes were carried out in the present study. Firstly, coaxial multi-pass TS scheme was developed. The performance of the multi-pass TS system was investigated by Raman scattering measurement, and up to twice higher SNR was expected compared with that obtained by the conventional single pass TS scheme. Secondly, replacement of the photon detectors (avalanche photodiodes (APDs)) and optimization of the applied voltage enable additional increment in the SNR. Although the genuine multi-pass scheme was not used in the present study because of optics stability problem, a double-pass TS scheme was used to obtain T_e anisotropy at the plasma center. It was found that T_e in TST-2 LHW-driven plasmas is isotropic within about

10 % error. We developed an HXR diagnostic system composed of an NaI scintillator, a photomultiplier tube (PMT), and an acrylic lightguide to achieve a high energy resolution and insensitiveness to the external magnetic fields generated by TST-2.

In TST-2, TS measurements were performed for LHW-driven plasmas with a plasma current of 25 kA, which is the highest current in LHW-driven ST plasmas so far. Here an outboard-launch capacitively coupled combline (CCC) antenna was used. As a result, T_e and n_e profiles were obtained for the first time in LHW-driven ST plasmas. n_e showed a peaked profile with 7×10^{17} m^{-3} near the plasma center, while T_e profile was hollow with around 10 eV at the core region and around 50 eV at the peripheral region. The HXR measurements showed a tendency, where effective temperature of fast electrons increases with plasma current in the range of 10–100 keV. Energy flux profile of HXR integrated over 15–100 keV obtained for the plasmas with $I_p \sim 10$ kA showed that the flux at the inboard side is higher than that at the outboard side.

In QUEST, TS measurements were performed for 300 kW/28 GHz ECW-driven plasmas with limiter configuration. In spite of the high plasma current of approximately 70 kA, which is same level as the world record, resultant T_e and p_e were low (several eV and less than 1 Pa, respectively), while n_e was 1.3×10^{18} m^{-3} near the plasma center. In compact torus (CT) injection experiments, TS measurements were performed during the CT injection for the first time, and increase of the central n_e by a few times was observed.

In ST plasmas started-up by RF in TST-2 and QUEST, pressures of bulk electrons obtained by the TS measurements are much lower than the plasma equilibrium pressures. Taking the results of the HXR measurements into account, it is suggested that the plasma equilibria are dominated by minor fast electrons generated by RF in both TST-2 and QUEST.

In summary, a high performance coaxial multi-pass TS diagnostic system was developed and the performance was evaluated by Raman scattering measurement. The HXR diagnostic system was developed and effective temperature of fast electrons and energy flux profile were obtained successfully in TST-2. Using the developed high performance TS measurement system, the T_e and n_e profiles of LHW-driven ST plasmas were measured for the first time. In addition, no significant anisotropy was found near the plasma center. As a result, it is suggested that plasma equilibrium is different from that in the conventional tokamaks, and minor fast electrons are dominant in the equilibrium. Similar equilibrium is obtained in QUEST. For detailed understanding of LHW-driven plasmas, it is necessary to establish a theory such as three-fluid axisymmetric equilibrium model.

Contents

List of Figures

List of Tables

Chapter 1

Introduction

1.1 Fusion energy

Fusion energy can be produced by fusion reaction of atomic nuclei and the amount of the energy is equal to the mass defect (i.e., $E = \Delta mc^2$). A representative example of energy production is the sun, whose energy source is derived from fusion reaction of four hydrogen atoms. So far, many studies have been performed in order to utilize the fusion energy for electric power generation. For a fusion reactor on the earth, the use of fusion reaction between deuterium (D) and tritium (T), isotopes of hydrogen, is the most attractive reaction from the point of view of fusion cross section. D-T fusion reaction is described as (see Fig. 1.1),

$$\mathrm{D} + \mathrm{T} \rightarrow {}^{4}\mathrm{He}\ (3.5\ \mathrm{MeV}) + \mathrm{n}\ (14.1\ \mathrm{MeV}). \tag{1.1}$$

The released energy is much lager than the ionization energy of a hydrogen atom of 13.6 eV by approximately 10^6 times. In addition to such large amount of available energy, a DT fusion reactor also has the following advantages: (1) deuterium and lithium, which can be converted to tritium, exist inexhaustibly in nature, (2) no runaway reactions occur in principle, and (3) CO_2 and long lived radioactive materials are not produced.

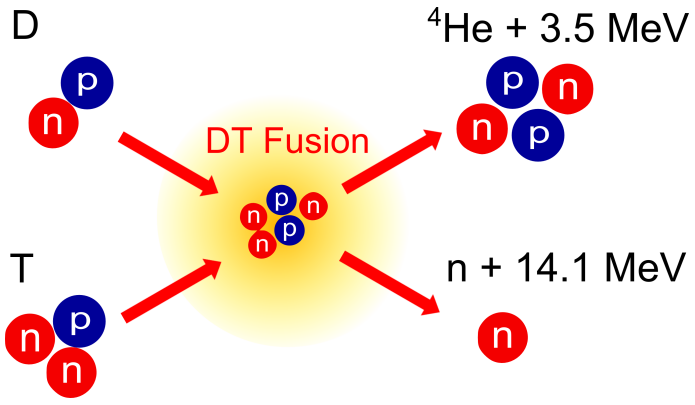

Fig. 1.1: A schematic drawing of D-T fusion reaction.

1.2 Tokamak and spherical tokamak

The phase of matter changes from solid to liquid, and to gas as the temperature increases, and then the intermolecular forces decrease. In a state with much higher temperature, the atoms of gaseous matter are ionized and break up into electrons with negative charges and ions with positive charges. Such state of being ionized gas is called plasma, and also called the fourth state of matter. In macroscopic scale, ions and electrons have almost the same charge numbers and charge neutrality is preserved in plasma. On the other hand, since each plasma particle has the electric charge in microscopic scale, plasma can be confined in a volume and the behavior can be controlled by an appropriate magnetic field configuration. Although the behavior of the plasma in the magnetic field is very complex, it is expected to induce fusion reaction continuously by confining with high density and high temperature DT plasmas.

The word "tokamak" is a Russian abbreviation of toroidal chamber with magnetic coils. The shape of a tokamak plasma is a torus, and such a configuration is formed by toroidal and poloidal magnetic fields [1]. The toroidal magnetic field is formed by a solenoid coil deformed into a torus shape, namely toroidal coils. The poloidal magnetic field in a tokamak is formed by toroidal current in the plasma. If the magnetic field has only toroidal component, the plasma particles cannot be confined, because the curvature of the toroidal field lines invokes charge separation of electrons and ions, resulting in a rapid loss of plasma particles. The superposition of the toroidal and poloidal field components (i.e., helical magnetic field lines) forms closed magnetic flux surfaces so that the charge separation is canceled.

In order to drive the toroidal current for producing poloidal fields and sustain the plasma for a sufficient duration, there are several kinds of plasma heating and current drive methods: (1) using inductive electric field generated by the central solenoid (CS), (2) injection of high energy neutral particle beams (NBI), (3) injection of high power radio frequency (RF) waves in several appropriate frequency ranges, and so on [2, 3]. ITER, international collaborative tokamak device aiming at a fusion gain of $Q = 10$ is now under construction in France to explore the physics of burning (reacting) plasma. Here Q is defined as ratio of produced thermonuclear power to supplied heating power.

A spherical tokamak (ST) is a tokamak with a low aspect ratio of $A = R/a < 2$ while A > 3 in conventional tokamaks, where R and a represent major and minor radii of the plasma, respectively. Figure 1.2 shows the comparison of a conventional tokamak and an ST [4]. As a measure of the efficiency of magnetically confined plasmas, the plasma beta $\beta = \langle nT \rangle / (B^2/2\mu_0)$ is often used, where μ_0 is the permeability of vacuum, B is the magnetic field strength. n and T are the plasma density and temperature, respectively, and their product is the plasma pressure p. When the beta is high, a relatively high pressure plasma is confined by a relatively low magnetic field strength. Therefore, higher beta is considered to be preferable for a reactor, where a certain pressure is required for fusion reactions. When the beta becomes high, the pressure becomes high and the plasma tends to be unstable. The maximum stable value of β is given by the Troyon limit [5] and the extended β limit including an elongation κ of the plasma cross section is as follows [6].

$$\beta_{\max} = 0.072 \left(\frac{1 + \kappa^2}{2A} \right). \tag{1.2}$$

Thus, an TS with a low aspect ratio A can sustain a high β and it is attractive for a fusion reactor from the view point of manufacturing cost of the device including the toroidal coils [8].

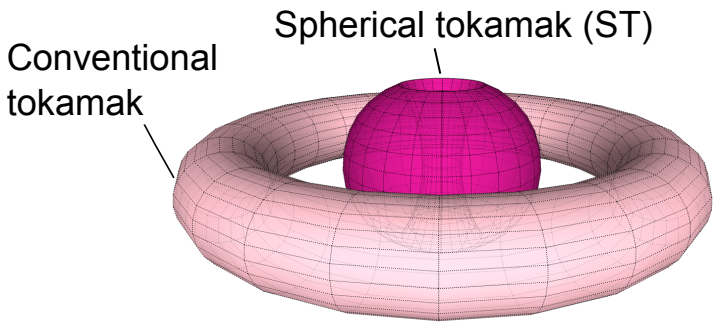

Fig. 1.2: Comparison of the ST plasma and conventional tokamak.

Moreover, an ST features a relatively higher elongation κ and that leads to a higher density limit and a high bootstrap current fraction [9,10] than those in conventional tokamaks. These features are also favorable for an efficient fusion reactor.

In conventional tokamaks, a central solenoid (CS) is used for plasma current start-up, but in STs, elimination of the CS or the reduction in its size is necessary for the realization of a reactor. Therefore, an alternative (non-inductive) start-up scenario must be established, and it is one of the most important issues. The most promising candidate for the non-inductive start-up scenario is the utilization of RF waves. RF start-up experiments have been performed in many devices so far and some results are described in the next section.

1.3 Review of non-inductive plasma start-up experiments

RF start-up experiments were performed successfully for the first time in WT-2 tokamak (Kyoto university, reported in 1983) [11,12]. Plasma current I_{p} reached up to approximately 5 kA. Two types of RF waves with different ranges of frequency: electron cyclotron wave (ECW) and lower hybrid wave (LHW) were utilized for the plasma start-up and current ramp-up, respectively. In 1984, achievement of current ramp-up to 100 kA in PLT tokamak (PPPL) was reported [13]. A high confinement mode (H-mode) plasma was created non-inductively for the first time in JT-60U tokamak (QST, reported in 2002) [14,15]. Similar to the WT-2 scheme, the plasma is sustained by ECW, and I_{p} is ramped up to 400 kA with the superposition of LHW power. After that, neutral beam injection (NBI) for additional heating and current drive was added, and formation of an H-mode plasma with a high bootstrap current fraction of at least 90% was accomplished.

Plasma experiments in ST have been widely performed since the late 20th century. Non-inductive start-up by ECW power was achieved for the first time in CDX-U (PPPL in 1992). A plasma current of 1.05 kA was generated by approximately 8 kW ECW power. About a decade later, similar experiments were performed in LATE at Kyoto university (first reported in 2004) [16]. Then the plasma current of 4 kA was sustained for 4 seconds by 10 kW /2.45 GHz microwave pulse. Recently, the current reached to 10.5 kA by 58 kW ECW injection and current drive by electron Bernstein wave (EBW), which is converted from the ECW, was confirmed [17, 18]. Also in medium-sized STs, MAST (CCFE) and QUEST (Kyushu university), similar experiments have been performed and plasma currents up to 73 kA and 66 kA were reported, respectively [19–25]. Current ramp-up experiments by using LHW power have been performed in small-sized STs, TST-2 (the university of Tokyo) and Globus-

M (Ioffe institute) [26–29]. In TST-2, three types of antenna for LHW excitation were used so far, and it is reported that the plasma currents reached up to 15 kA, 10 kA, 16 kA, respectively. In addition, non-inductive start-up scenarios by utilizing plasma merging (in MAST and UTST (the university of Tokyo) [30, 31]) and coaxial helicity injection (CHI) (in NSTX (PPPL) [32]) have been studied. Recently, conceptual design of SlimCS, a fusion DEMO reactor aiming at demonstration of fusion power production, was reported, and its economic feasibility was discussed [33, 34]. The design is based on tokamak device with a low aspect ratio and it is planned that the plasma current is started-up by the use of reduced-size CS and ECW.

1.4 Objectives and outline

One of the problems in the development of a low aspect ratio tokamak reactor is that an optimum start-up scenario has not been established. Our group has been promoting the establishment of the start-up scenario by LHW and ECW in TST-2 and QUEST, respectively. In order to find out the limit of current drive efficiency in the optimum scenario, it is necessary to iterate experiment and simulation.

Profiles of electron temperature T_e and electron density n_e are fundamental plasma parameters and the measurement of them is important for the evaluation of plasmas. Since these parameters contributes to the energy stored in plasmas, they are obviously important in evaluating performance of a plasma device. Profiles of n_e and T_e are also necessary in calculating the propagation, mode conversion, and absorption profiles of waves. In order to simulate the behaviors of a wave, we need these profiles as the boundary condition of the simulation. Since electron temperature anisotropy reflects confinement of bulk electrons and slowing down of the fast electrons, it is important to measure the anisotropy when these effects are considered. Information of hard X-ray (HXR) radiation is also important because it reflects absorption profile of LHWs and energy range of fast electrons generated by the LHWs. Effective temperature of fast electrons and energy flux profile of HXR are useful for the analysis of plasma equilibrium and interaction between bulk electrons and fast electrons.

In order to measure profiles of n_e and T_e, Thomson scattering (TS) diagnostic systems were developed in TST-2 and QUEST. In TST-2, TS measurements have been performed for Ohmically heated plasmas successfully. However, no TS measurements have been performed for RF-driven plasmas because of 10–100 times lower density than that for OH plasmas, leading to poor signal-to-noise ratio (SNR) in the measurement. Here, it is not desirable to increase the plasma density because LHW cannot access high density region due to mode conversion to other types of wave (i.e., fast waves). In the present study, therefore, we try to improve the SNR in the TS measurement by a few techniques: application of a coaxial multi-pass TS diagnostic system, improvement and optimization of the detection system, and accumulation of TS signals obtained from reproducible discharges. In addition, a coaxial double-pass TS diagnostic system is developed to measure T_e anisotropy. In QUEST, in order to perform detailed measurement, spatial points are increased from 6 to 12, and accuracy in the measurement timing is improved from ± 50 ms to $\pm\ 1\ \mu$s .

In order to measure HXR radiation due to fast electrons generated by LHWs, an HXR diagnostic system is developed in the present study. The system should have the capability of profile measurement and the sensitive energy range from a few tens to a few hundreds of keV. In TST-2, there are some viewing ports with 3 mm thick borosilicate glass windows with transmissivity of about 60 % for a 30 keV HXR photon. However, the diameter of the

window is not large because of the thin glass, and the measurable line-of-sight is limited by TF coils. Therefore, the detection system should be placed inside the TF coils and should be compact to measure the profile. In the previous study, several types of HXR systems were developed. However, all the systems seem to be not suitable for the present purpose. A system using a CdTe semiconductor detector and a system using a small NaI scintillator and an avalanche photodiode (APD) can be set inside the TF coils, but the electromagnetic noise was too large to measure low energy HXRs and it was also difficult to eliminate the noise. A system with a small scintillator and a small photomultiplier tube (PMT) showed a poor energy resolution and a low SNR. Although the system with a large scintillator and a large PMT shows a high energy resolution and a high SNR, the profile measurement is impossible because such a large system cannot be placed inside the TF coil. To make matters worse, signal amplification of a PMT is significantly affected by the magnetic field inside the TF coils. Therefore, a new HXR diagnostic system, where a large scintillator, a large PMT, and a thick acrylic lightguide are used, is developed in the present study.

For the analysis of plasmas in TST-2, three types of codes are used, i.e., EFIT, GENRAY, CQL3D. EFIT is an equilibrium reconstruction code, which gives us information on pressure, magnetic surfaces, and magnetic axis position by using the result of magnetic measurements. GENRAY is a ray-tracing code, which calculates propagation and absorption of LHWs for given initial conditions (e.g., temperature and density profiles of electrons and ions, the result of EFIT code, and position and angle of launched waves). CQL3D is a Fokker-Planck code, which calculates the time evolution of velocity distribution function of electrons. From the simulation, a current density profile is obtained. The results of these simulations are compared with the experimental results to improve the reliability of the simulations and to understand the physics of start-up plasma. The total plasma current is one of such parameters. In addition, modeling of hard X-ray (HXR) measurement is available in CQL3D. Thus, we measure the energy flux profile of HXR, which reflects current density profile, and the results can be compared with that from the simulation.

In summary, the main objectives in this thesis are listed below:

1. Development of a coaxial multi-pass TS diagnostic system and detection system to improve the signal to noise ratio: The performance is tested quantitatively and the practicability is evaluated.

2. Measurement of n_e and T_e profiles of TST-2 LHW-driven plasmas: The profile is compared with the results of EFIT. In order to investigate whether significant T_e anisotropy occurs or not, a coaxial double-pass TS diagnostic system is developed and the measurement is performed. The obtained profiles are used as the input data of GENRAY and CQL3D.

3. Development of an HXR diagnostic system with a wide viewing field and with a relatively high energy resolution: Measured effective temperatures of fast electrons are used to study the plasma equilibrium and the interaction between the bulk electrons and the fast electrons. The measured HXR energy flux profiles are compared with the simulation result of CQL3D.

4. Measurement of n_e and T_e profiles of QUEST ECW-driven plasmas: The equilibrium is evaluated and compared with that in TST-2. Similar measurements are performed for Ohmically heated plasmas with compact torus injection, which is an advanced fueling method, and the characteristics and the performance are evaluated.

This thesis consists of seven chapters. Chapters 2 and 3 describe the development of Thomson scattering and a hard X-ray diagnostic systems on TST-2. Experimental results on TST-2 and QUEST are shown in chapters 4 and 5, respectively. Chapters 6 and 7 present the discussion and the conclusions.

Chapter 2

Development of Thomson scattering diagnostics on TST-2

Thomson scattering (TS) measurements have been performed on TST-2 for about ten years [35–38]. However, all the target plasmas were Ohmically heated plasmas. Some modifications were applied in order to measure the low density non-inductively started-up plasmas. In this section, overview of the previous TS measurement system, which has been operated so far, and the modifications are described. A similar TS system has been constructed in QUEST, and thus detailed information about this system is omitted. The detail is described in Refs. [39, 40]

2.1 Principle of Thomson scattering measurement

Thomson scattering is the elastic scattering of an incident electromagnetic wave by a free electron. The wavelength of the scattered wave is the same as that of the incident wave. When the electron is moving, the observed wavelength is shifted by the (relativistic) Doppler effect. As shown in Fig. 2.1, a vector **k** is defined as

$$\mathbf{k} = \mathbf{k}_\mathrm{s} - \mathbf{k}_\mathrm{i}, \tag{2.1}$$

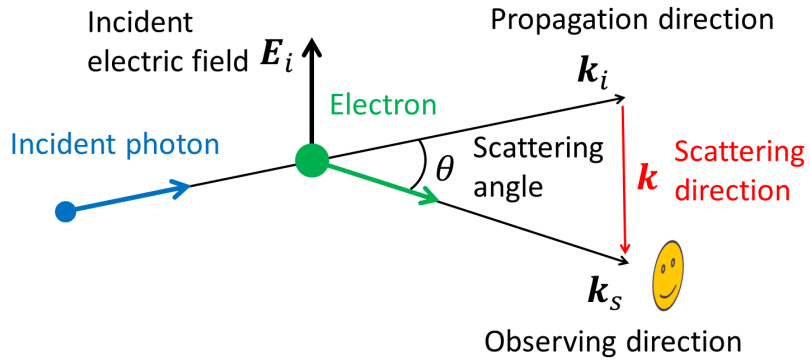

Fig. 2.1: Vector diagram of scattering.

where $\mathbf{k}_\mathrm{s}$ and $\mathbf{k}_\mathrm{i}$ are the wave number vectors of the scattered and incident waves, respectively. In the TS measurement of plasmas, laser light is used as the incident wave. In plasmas, the typical normalized correlation length is $\alpha = 1/|\mathbf{k}|\lambda_D$, where λ_D is the Debye length representing the scale of shielding of an external electric potential, and it is described as follows [41],

$$\lambda_D = \sqrt{\frac{\epsilon_0 k_B T_e}{n_e e^2}}. \tag{2.2}$$

In the case of $\alpha << 1$, the correlations between all contributing particles can be ignored, and then the whole scattered power equals the sum of power scattered by each electron, and the scattering is classified as incoherent scattering. The wavelength spectrum of incoherent TS includes information on the velocity distribution function of electrons in the plasma. Assuming that the velocity distribution function of electrons is a Maxwell distribution in thermal equilibrium, electron temperature T_e is estimated from the width of the distribution. Moreover, since the amount of scattered light is proportional to the electron density n_e, the absolute electron density can be obtained when the system throughput is absolutely calibrated.

Intensity of the detected TS signal for each channel of the polychromater, S_i^{TS} is written as

$$S_i^{\mathrm{TS}} = AGPr_0^2 n_\mathrm{e} \int S_\mathrm{R}^{(2)}(T_\mathrm{e}, \lambda) f_i(\lambda) d\lambda \left(\frac{dI_\mathrm{TS}}{d\Omega} \right) \Bigg|_{\beta=\pi/2}, \tag{2.3}$$

where A is the instrumental coefficient given by $C_\mathrm{T} \times L_\mathrm{s} \times \delta\Omega$ (C_T is the total transmission efficiency of the incident and collection optics, L_s is the scattering length, $\delta\Omega$ is the observation solid angle), G is the gain of the amplifier, P is the incident laser energy, r_0 is the classical electron radius, and f_i is the spectral sensitivity of the i-th channel. $S_\mathrm{R}^{(2)}$ is the second order approximate relativistic spectral density function of Thomson scattering (per unit wavelength), which is given by [42]:

$$\begin{aligned} S_\mathrm{R}^{(2)}(\epsilon) =& S_\mathrm{N}(\epsilon) \left[1 - \frac{7}{2}\epsilon + \frac{\alpha\epsilon^3}{2(1-\cos\theta)} - \frac{1}{8\alpha}\left(\frac{39}{8} - 5\cos\theta \right) + \frac{1}{8}\left(29 + \frac{5}{1-\cos\theta} \right)\epsilon^2 \right. \\ & \left. - \frac{1}{16(1-\cos\theta)}\left(28 - \frac{1}{1-\cos\theta} \right)\alpha\epsilon^4 + \frac{\alpha^2\epsilon^6}{8(1-\cos\theta)^2} \right], \end{aligned} \tag{2.4}$$

where

$$S_\mathrm{N}(\epsilon) = \left(\frac{\alpha}{\pi} \right)^{1/2} \frac{1}{\sqrt{2(1-\cos\theta)}} \exp\left\{ \frac{-\alpha\epsilon^2}{2(1-\cos\theta)} \right\}. \tag{2.5}$$

Here, $\alpha \equiv m_\mathrm{e}c^2/2T_\mathrm{e}$, θ is the scattering angle, and $\epsilon = (\lambda_\mathrm{s}/\lambda_\mathrm{i} - 1)$, which represents the relative shift in wavelength of the scattered light, where λ_i and λ_s are the incident and scattered wavelengths, respectively. $dI_\mathrm{TS}/d\Omega$ is the angular distribution of the differential cross section of Thomson scattering:

$$\frac{dI_\mathrm{TS}}{d\Omega} = \frac{3}{8\pi}\sin^2\beta, \tag{2.6}$$

where β is the angle between the directions of the laser polarization and the observer. Figure

2.2 shows spectra calculated by the above equation for a few given temperatures.

Figure 2.3 shows the arrangement of a conventional TS diagnostic system, which consists of a high energy pulse laser, a light collection system, and spectrometers. Although T_e measurement from TS is one of the most reliable diagnostics [43–46], the reliability is guaranteed only in a high density plasma because the obtained signal intensity depends on n_e. Thus, in the measurement of low density plasmas such as TST-2 RF started-up and sustained plasmas, some breakthrough schemes are needed to perform highly reliable T_e and n_e measurements.

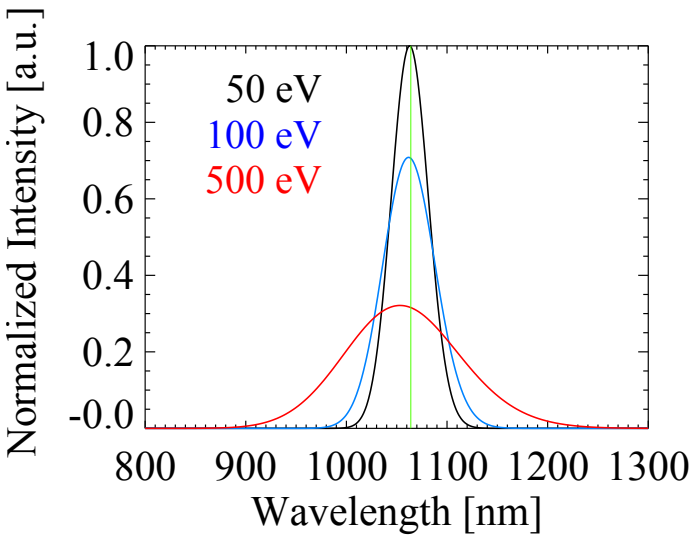

Fig. 2.2: Spectra of TS for the cases with electron temperatures of 50 eV (black), 100 eV (blue), and 500 eV (red). The incident laser wavelength is 1064 nm (green), and the scattering angle is $\theta = 120^\circ$.

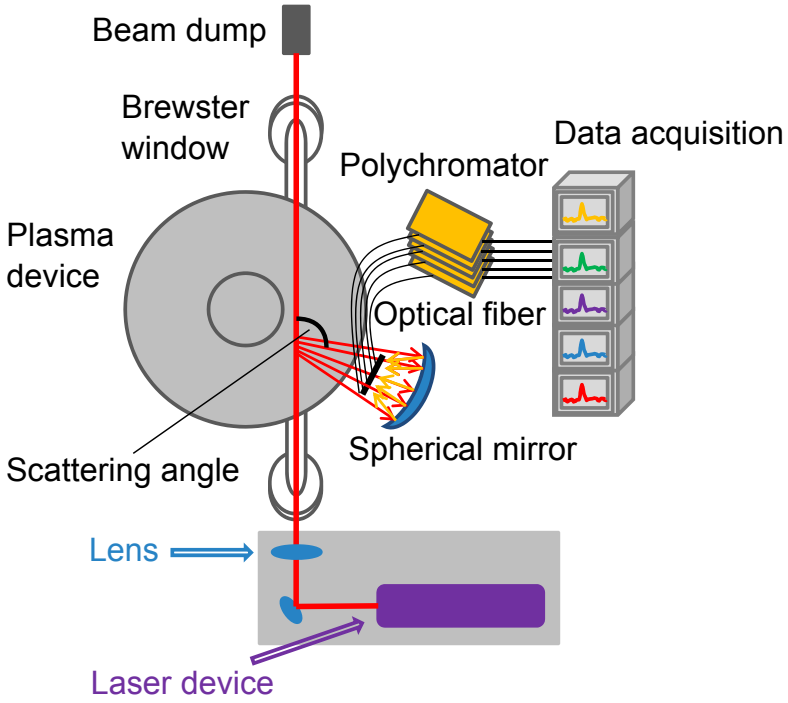

Fig. 2.3: A schematic diagram of a conventional TS diagnostic system.

2.2 Optical system

Table 2.1 shows the specification of the Yttrium-Aluminum-Garnet (Nd:YAG) laser used in TST-2 (YG981E, Quantel). Since the intensity of TS light is very weak compared with the incident laser energy, an intense laser with energy of a few Joules is used. In TST-2, radiation through windows is mainly visible light, and thus we used an infrared YAG laser with the wavelength of 1064 nm and the short pulse duration of approximately 10 ns to avoid shot noise of the background light and to improve the signal-to-noise ratio (SNR). Since the incident laser and collection optics are located on the (horizontal) midplane of TST-2, it is found from Eq. (2.6) that polarization direction of the laser should be vertically-polarized.

Parameter	Values
Wavelength	1064.1 nm
Repetition rate	10 Hz
Pulse energy	1.6 J
Pulse width	~ 10 ns
Beam diameter	~ 10 mm
Beam divergence	~ 0.5 mrad
Polarization ratio	95
Energy stability	±2 %
Pointing stability	$< 50\ \mu$rad

Tab. 2.1: Specification of the YAG laser in TST-2.

The collection optics consists of an optical window, a spherical mirror, and optical fibers. Table 2.2 shows the parameters of the configuration in TST-2 and scattering condition for the case of scattering near the plasma center (i.e., at $R = 360$ mm). The parameters are the scattering angle, the length of scattering volume, the solid angle of scattered light toward the spherical mirror, the diameter of the fiber, the numerical aperture of the fiber, and the magnification of the spherical mirror, respectively. A part of the scattered light passes through the optical window. They are collected by the spherical mirror, and focused on an optical fiber array, where ten fibers are aligned on the midplane (see Fig. 2.4). The size of the scattered light beam collected into each fiber (i.e., scattering length) determines the spatial resolution in the plasma.

Parameters	Values
Scattering angle	$\sim 120^\circ$
Scattering length	~ 5.8 mm
Solid angle	~ 0.19 sr
Fiber core	$\phi 2.0$
Fiber N.A.	0.37
Magnification	~ 2.5

Tab. 2.2: Parameters of the collection optics and the scattering condition for the case of scattering at the plasma center.

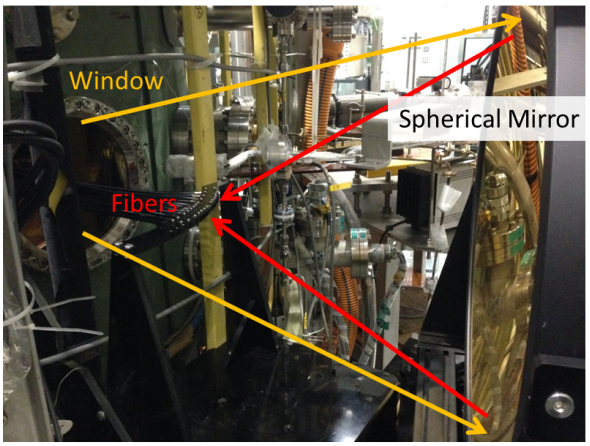

Fig. 2.4: Photograph of the collection optics.

Since the laser intensity is much stronger than the scattering light, laser light entering the detectors via unwanted or unexpected path can be a serious noise. Such unwanted light is called “stray light”. Stray light becomes a crucial problem for TS measurement if no provision is taken. Stray light is caused by the spread laser beam whose diameter is larger than that of an optical component, and the beam is reflected by the outer frame of the component or passes through outside the component. When the light enter a fiber or a polychromator directly, it becomes stray light noise. The stray light generated at the atmosphere side is

easily extinguished by a blackout curtain, a shading box and so on. On the other hand, the stray light generated inside the vacuum vessel is difficult to eliminate, because once it is generated, it is difficult to distinguish it from the TS light. Using some baffle plates in the entrance tube was effective to some extent. In many TS diagnostic systems, main source of the stray light comes from the beam dump. In these cases, baffle plates in the exit tube also help us to eliminate the stray light. However, it should be noted that the return light from the baffle plates can be a new stray light source. In TST-2, small baffle plates at the exit tube became the stray light source, thus they were removed. In addition, double-pass TS scheme (described in Sec. 2.6), the baffle plates at the entrance tube also increased the stray light strength. Therefore, only non-fixed baffle plates located outside the vessel and linearly movable shutters located at the root of both tubes are used in the present system. Amount of the stray light is still high for the edge measurement points. A spatial filter is useful to shut out the peripheral part of the laser beam profile, and we are now developing one.

The polychromator in TST-2 consists of seven convex lenses, six sets of an interference filter and an avalanche photodiode (APD), and a detection circuit (Fig. 2.5). Each interference filter works as a band-pass filter. The detection circuit is designed so that a fast time response and low thermal noise are achieved by optimizing input resistance in current-to-voltage conversion. The resultant pulse width (FWHM) of a YAG laser signal is 10 ns, which is similar to that of the original pulse width [47]. Figure 2.6 shows the sensitivity spectrum of each wavelength channel in the polychromator, and Table 2.3 shows the central wavelength of the transmission band for each filter. The filter numbers written in Fig. 2.5, Fig. 2.6 and Tab. 2.3 correspond to each other.

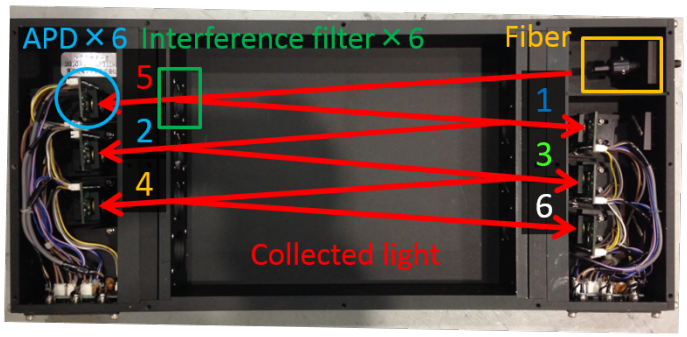

Fig. 2.5: Photograph of a polychromator. The top panel is removed to show the inside.

Filter	Wavelength
#1	1059 nm
#2	1055 nm
#3	1050 nm
#4	1040 nm
#5	1020 nm
#6	1070 nm

Tab. 2.3: The center wavelength of transmission band of the six interference filters.

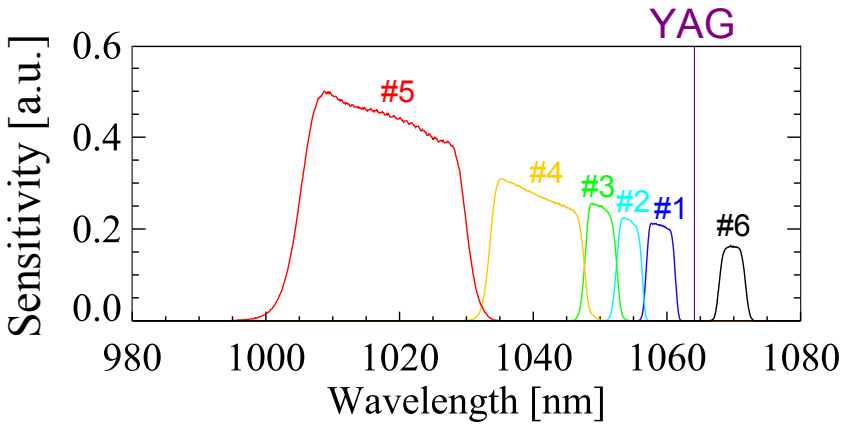

Fig. 2.6: Sensitivity spectra of the six (wavelength) channels in the polychromator.

2.3 Acquisition and analysis of data

The six signals from APDs and the trigger signal are recorded by an oscilloscope (DL7480, Yokogawa Meters & Instruments) with a sampling rate of 1 GHz and a band width of 500 MHz. Plasma discharge timing is adjusted so that laser is fired at arbitrary timing. Up to five spatial points can be measured simultaneously, and 15 spatial points in the region R = 197–546 mm are available. Firstly, the background signal including the stray light is subtracted from the obtained signal. The background signal is acquired by averaging over multiple (around 100) signals, which are taken just after a plasma discharge. Secondly, the remaining signal is fitted to a template function, which is given by the product of a Gaussian function, and step function-like hyperbolic tangent [38]. Typical waveforms of Raman scattering signal and the fitting function are shown in Fig. 2.7. Since the peak position (i.e., timing) and the pulse width are known, the free parameters in the fitting are only the amplitude and the offset. The amplitudes obtained from the six wavelength channels in each polychromator is used for the following Maxwell fitting to estimate T_e and n_e.

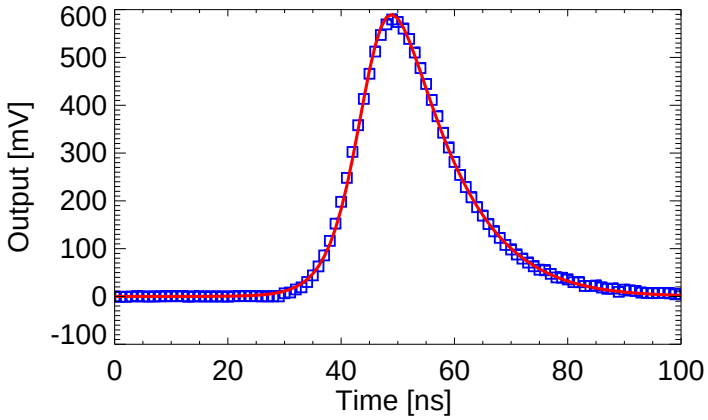

Fig. 2.7: Typical Raman scattering signal (blue squares) and the fit (red curve).

2.4 Calibration

2.4.1 Relative calibration in polychromator

In order to measure the wavelength sensitivity of each filter (as shown in Fig. 2.6) in a polychromator, calibration using monochromatic light made by a spectrometer and a standard light is performed. Figure 2.8 shows the setup of the calibration. The standard light radiates light with a known (i.e., calibrated) intensity as a function of wavelength (see Fig. 2.9), and light with an arbitrary wavelength is extracted by the spectrometer. The light is introduced to the polychromator through a fiber and responses of the detector signal is recorded while scanning the wavelength.

Since the calibration of the polychromators by using the spectrometer is performed in a room different from that of plasma measurement (i.e., the TST-2 machine room), the wavelength sensitivities often deviate from the calibrated ones because of some reasons, e.g., change in the ambient temperature. Therefore, additional calibration using another standard light is performed at least once every day of the TS measurement. Figure 2.10 shows a photograph of this in-situ calibration setup. The standard light is mounted on the spherical mirror and a diffuser is placed in front of the optical window. The light from the standard light source is scattered on the diffuser and is transmitted to the polychromator via the spherical mirror and the fibers. This light enables us to calibrate the relative sensitivity among 6 wavelength channels in each polychromator. Moreover, since fluctuation of the light intensity is quite small (less than 1 % fluctuation at every calibration), absolute sensitivity of the detection system can be derived by comparing the amount of the detected light with that in Raman scattering (absolute) calibration. It should be noted that long-term change of the spectral transmissivity of the optical window and interference filter itself after the calibration using the spectrometer cannot be corrected by this in-situ calibration. In TST-2, such distortion has not been seen. On the other hand, in QUEST, spectral transmissivity of the window decreased by 30 % in maximum in the previous tests. Thus, periodic cleaning of the window surface is necessary in QUEST.

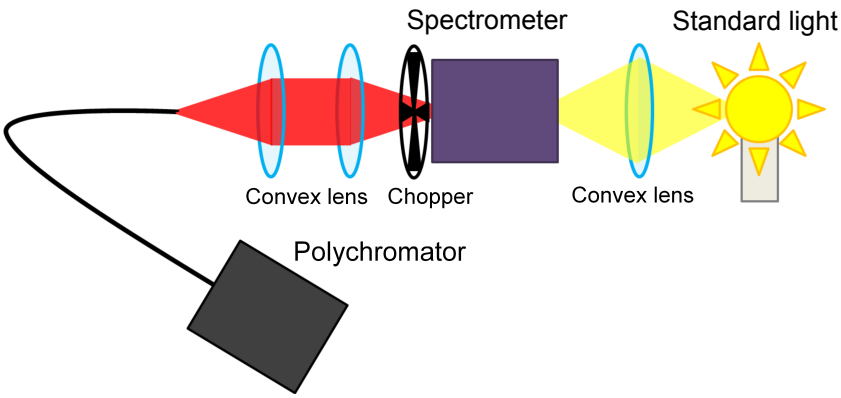

Fig. 2.8: A schematic arrangement of calibration of polychromators.

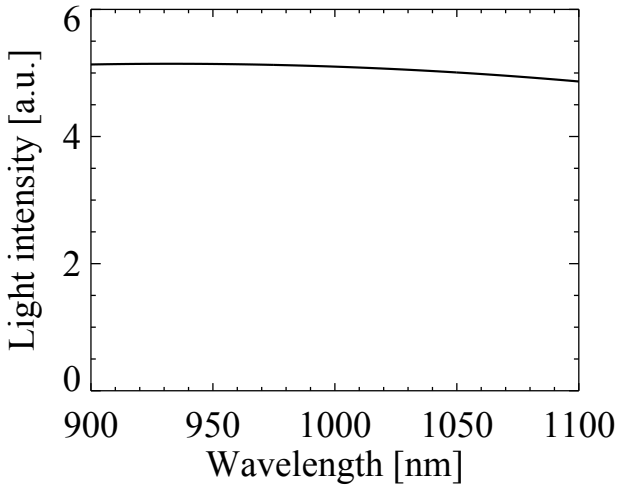

Fig. 2.9: Intensity distribution of the standard light used in TST-2.

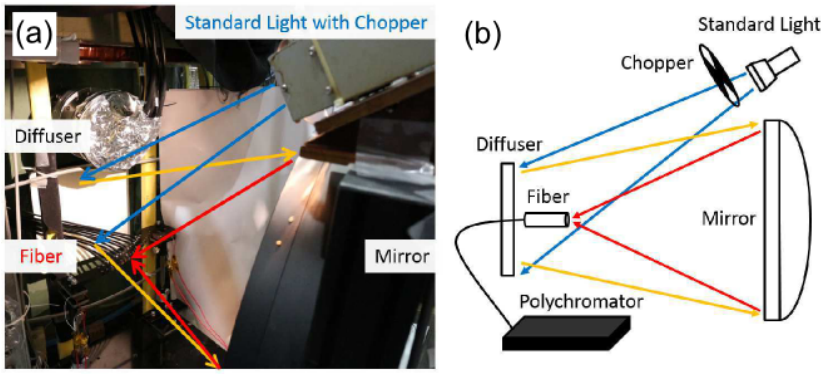

Fig. 2.10: Photograph of the in-situ calibration setup (a) and its schematic diagram (b). The setup consists of a standard light, a chopper, a diffuser, a spherical mirror, and a fiber [48].

2.4.2 Absolute calibration by rotational Raman scattering (RRS)

Although the electron density n_e is proportional to the number of TS photons, which corresponds to signal intensity, the absolute value of n_e cannot be derived only by TS measurement because the true value of AGP in Eq. (2.3) is unknown. In order to measure AGP (i.e., the relationship between n_e and the integrated intensity), the absolute calibration by rotational Raman scattering (RRS) is carried out. The calibration is performed by filling the TST-2 vacuum vessel with nitrogen gas, and all the other setup is the same as that in the TS measurements. When we know the pressure, the RRS intensity can be calculated as described in the following.

The angular dependence of RRS light intensity I_{RRS} is different from that of I_{TS}, and nearly isotropic:

$$\left(\frac{dI_{\mathrm{RRS}}}{d\Omega}\right) = \frac{3}{8\pi}\frac{6+\sin^2\beta}{10}. \tag{2.7}$$

RRS signal intensity detected by each interference filter in the polychromater, S_i^{RRS} is written by the following equation [49, 50]:

$$S_i^{\mathrm{RRS}} = AGPn^{\mathrm{N}} \sum_J w_J^{\mathrm{N}} \sigma_J^{\mathrm{N}}(\lambda_J^{\mathrm{N}}) f_i(\lambda_J^{\mathrm{N}}) \left(\frac{dI_{\mathrm{RRS}}}{d\Omega}\right)\Bigg|_{\beta=\pi/2}, \tag{2.8}$$

where suffix N stands for nitrogen, J is the initial rotational angular momentum quantum number, w_J^{N} is the population of the initial rotational state, and σ_J^{N} is the cross section of RRS including Stokes $J \to J+2$ and anti-Stokes $J \to J-2$ transitions. Note that the ratio of angular distributions in TS (Eq.(2.6)) and RRS (Eq.(2.7)) integrated over the solid angle of our collection system was calculated to be 1.41, which is only a few percent difference compared with that with $\beta = 90^\circ$ (1.43) [35]. The wavelength shifts of the Stokes and anti-Stokes RRS are described as

$$\frac{1}{\lambda_{J\to J+2}} - \frac{1}{\lambda_0} = (2B_0 - 3D_0)(2J+3) + D_0(2J+3)^3, \tag{2.9}$$

$$\frac{1}{\lambda_{J\to J-2}} - \frac{1}{\lambda_0} = (2B_0 - 3D_0)(2J-1) - D_0(2J-1)^3, \tag{2.10}$$

where λ_0 is the wavelength of the incident laser, B_0 is the rotational constant, and D_0 is the centrifugal distortion constant. Several constants for molecular nitrogen are listed in Tab. 2.4.

	B_0 (m^{-1})	D_0 (m^{-1})	g_J (even J)	g_J (odd J)	γ (10^{-30} m^3)
N_2	1.99×10^2	5.74×10^{-4}	6	3	0.66

Tab. 2.4: Constants to calculate RRS cross section for nitrogen.

In thermal equilibrium at a temperature T, w_J^{N} is written as

$$w_J^{\mathrm{N}} \simeq \frac{1}{W} g_J (2J+1) \exp\left\{ -B_0 J(J+1) \frac{hc}{k_{\mathrm{B}} T} \right\}, \tag{2.11}$$

where g_J is the statistical weight factor which depends on the nuclear spin. The normalization factor W is determined from the condition:

$$\sum_{J=0}^{\infty} w_J^{\mathrm{N}} = 1. \tag{2.12}$$

The cross sections of Stokes and anti-Stokes RRS are written as

$$\sigma_{J\to J+2}^{\mathrm{N}} = \frac{7(2\pi)^4}{45} \frac{\gamma^2}{(\lambda_{J\to J+2}^{\mathrm{N}})^4} \frac{3(J+1)(J+2)}{2(2J+1)(2J+3)}, \tag{2.13}$$

$$\sigma_{J\to J-2}^{\mathrm{N}} = \frac{7(2\pi)^4}{45} \frac{\gamma^2}{(\lambda_{J\to J-2}^{\mathrm{N}})^4} \frac{3J(J-1)}{2(2J+1)(2J-1)}, \tag{2.14}$$

where γ is the polarization anisotropy given in Tab. 2.4. In addition, depolarization effect should be included in the calculation of RRS cross section. The polarization dependence of the scattering cross section is given by [51]

$$\sigma_{J\to J'}^{\mathrm{N}\,\prime} = \sigma_{J\to J'}^{\mathrm{N}} \left[(1-\rho)\cos^2\phi + \rho \right], \tag{2.15}$$

where ϕ is the angle between the polarizations of incident and scattered light and ρ is the depolarization factor whose theoretical value is $\rho_{\mathrm{theory}} = 0.75$. In our experimental configuration, the depolarization effect was investigated by rotating polarizer and the experimental value of $\rho_{\mathrm{exp}} = 0.69$ was obtained [38]. When ρ_{theory} and ρ_{exp} are different, modification of the Raman cross section $\sigma_{J\to J'}^{\mathrm{N}}$ is necessary and the weighted cross section L is given by [52]

$$L = \sigma_{\perp}\epsilon_{\perp} + \sigma_{\parallel} = \left(\frac{3}{7}\epsilon_{\perp} + \frac{4}{7} \right) \sigma_{J\to J'}^{\mathrm{N}}, \tag{2.16}$$

where $\epsilon_{\perp}$ is the relative efficiency in polarization, i.e., $\epsilon_{\perp} = \rho_{\mathrm{exp}}/\rho_{\mathrm{theory}}$. Therefore, $\epsilon_{\perp}$ is calculated as $\epsilon_{\perp} = 0.69/0.75 = 0.89$ in TST-2. Figure 2.11 shows the calculated cross section of Stokes and anti-Stokes RRS cross sections.

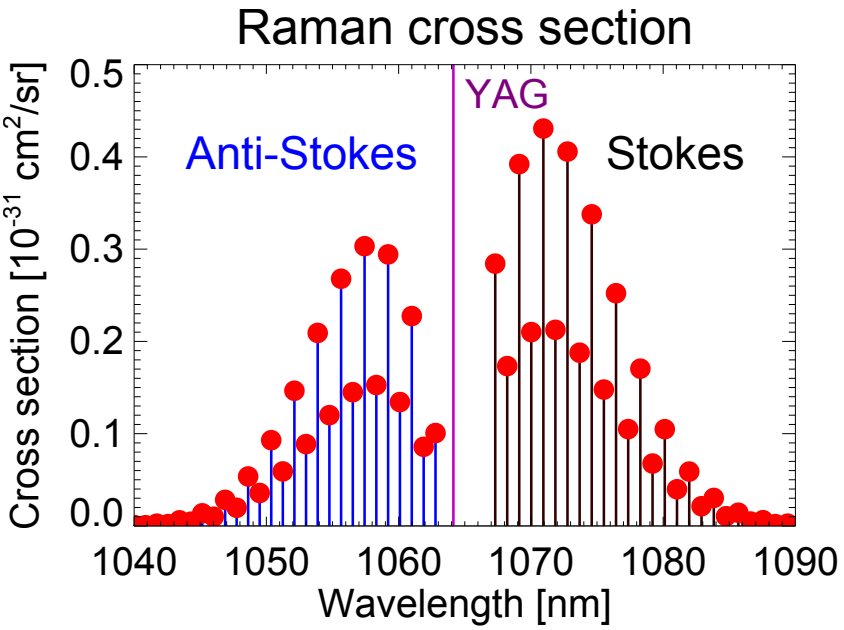

Fig. 2.11: Calculated cross sections of Stokes and anti-Stokes RRS.

RRS measurements with nitrogen gas pressures of 0, 15, and 31 Torr were performed. Figure 2.12 shows the result of the pressure dependence of the ratio of the signal intensity S^{RRS} to effective RRS cross section σ_{R}, which is defined as the weighted cross section L including the spectral sensitivity and the angular distribution of the RRS light. The slope of this linear function corresponds to the product AGP in Eq. (2.8). Resultant ratio of the TS signal intensity to the electron density for each measurement position is shown in Fig. 2.13

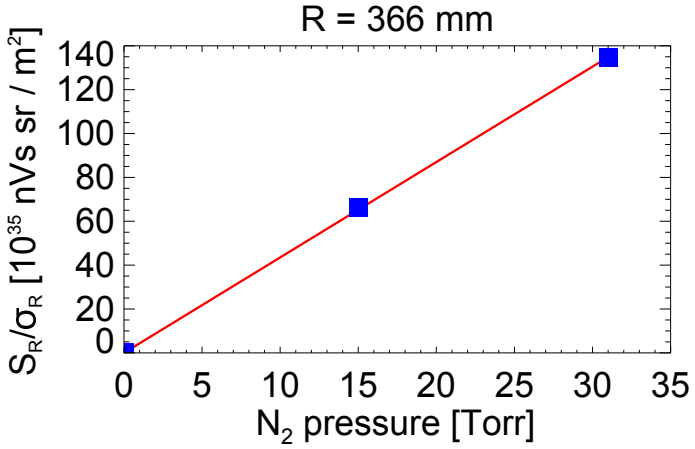

Fig. 2.12: Pressure dependence of the ratio of signal intensity S^{RRS} to RRS cross section σ_{R} for channel #2.

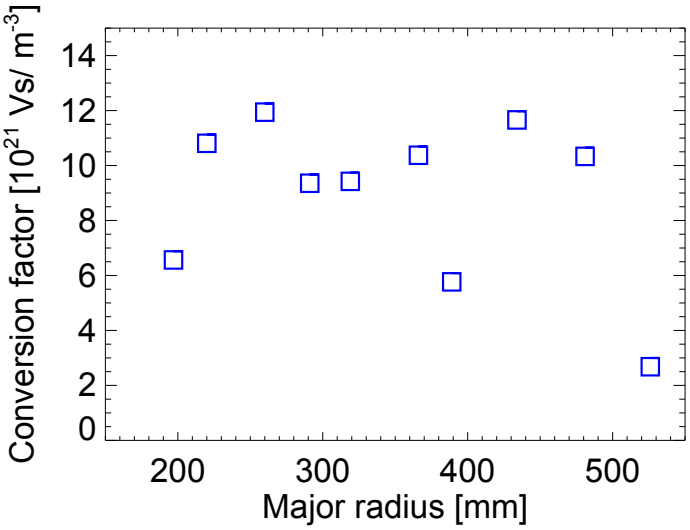

Fig. 2.13: Profile of ratio of the TS signal intensity to the electron density which were calibrated by the RRS measurement.

2.5 Estimation of errors

In TST-2 TS measurement, obtained signals in a polychromator are fitted to a Maxwell distribution function with the free parameters: the amplitude and width, to estimate n_e and T_e. This fitting is processed by the use of CURVEFIT function in IDL language [53], which is a weighted least squares method, and the following squared residual is minimized.

$$J = \sum_{i=1}^{n} \frac{(y_i - f(\lambda_i))^2}{\sigma_i^2}, \tag{2.17}$$

where y_i and $f(\lambda_i)$ are signal intensity and estimated value in i_{th} channel, respectively. The residual in each channel is weighted by $1/\sigma_i^2$, where σ_i is given by accumulation of Poisson noise due to the scattered light and stray light and random noise due to thermal fluctuations of a resistance in the detection circuit. The weight is re-adjusted without changing the relative weight so that the normalized chi-square becomes 1. ΔT_e and Δn_e are calculated from the error propagation law, and they are proportional to the adjusted σs.

Since the fitting is nonlinear in terms of the fitting parameters, the results have a dependence on the initial estimation of the T_e and n_e, and the obtained T_e and n_e might be incorrect when the initial estimates are far from the correct T_e and n_e. In order to avoid such a situation, we prepared 36 combinations of the initial estimates, and the optimum set is chosen by comparing obtained fitting errors. As a result, apparent discrepancies in the Maxwellian fitting disappeared.

One of the major causes of error in the TS measurement is the sensitivity uncertainly of APD detectors. The sensitivity depends on the ambient temperature and the typical dependence is shown in Fig. 2.14. The specification and the previous measurement (see Ref. [38]) reported that the bias voltage to an APD should be changed by approximately 2.5 V when there is one degree temperature change. The relationship between the voltage and temperature yielding a constant gain is shown in Fig. 2.15. Gain increment per one degree is plotted in Fig. 2.16. It is indicated that the influence of temperature variation starts to increase

when the bias voltage increases beyond $V_{G=100}$. Thus, a treatment to avoid such gain change is necessary to use the APD at a high gain condition. In the present study, TS measurements were performed under the control of the temperature with the variation of less than ±0.5 degree by using an air conditioner and a fan.

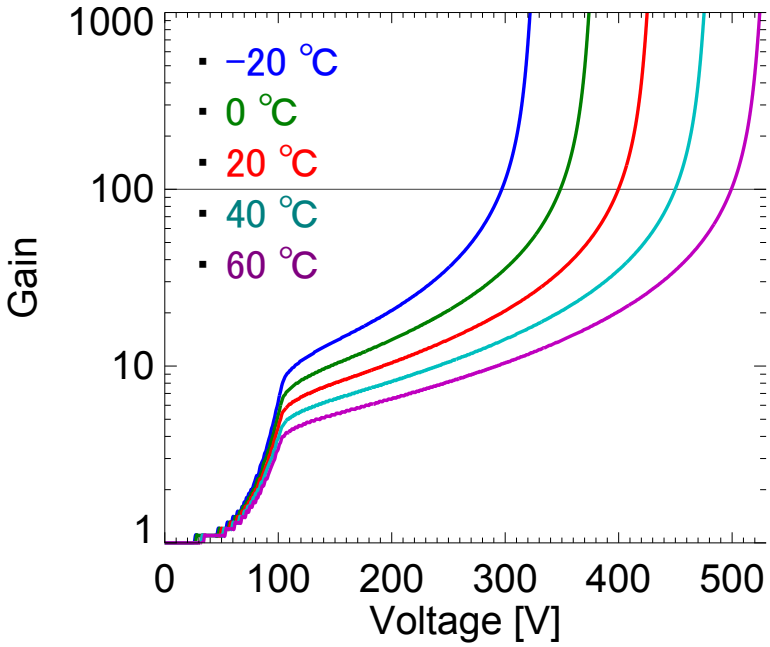

Fig. 2.14: Bias voltage dependence of APD gain for various temperatures.

2.6 Techniques for improvement of measurement accuracy

2.6.1 Optimization of detecting system

In the previous system, silicon avalanche photodiodes (Si APD: S8890-30, Hamamatsu photonics) had been used. In 2010, a new APD (S11519-30) which has a higher sensitivity around YAG wavelength (1064 nm) was released. Then the previous APD was replaced by the new one and the performance was compared each other by using a standard light. The setup is similar to that in relative calibration of the polychromator described in the previous section (Fig. 2.10). Typical detected signal is shown in Fig. 2.17. The bias voltage was scanned to investigate the behavior of signal, noise and the SNR, and to find out the optimum voltage. The signal amplitude is defined as the peak-to-peak value of the signal, and the noise amplitude is given by the standard deviation of background noise (i.e., without the light). The test was performed for both previous and new APDs, where the same polychromator and the same interference filter with a central wavelength of 1060 nm were used. The results are shown in Fig. 2.18.

The signal amplitude increases nonlinearly with the bias voltage. On the other hand, the noise is almost constant until a certain voltage. Above the voltage, rapid increase of the noise starts due to avalanche breakdown. By the replacement, the signal amplitude increased while the noise was similar, and 2.4 times higher SNR was obtained in each bias

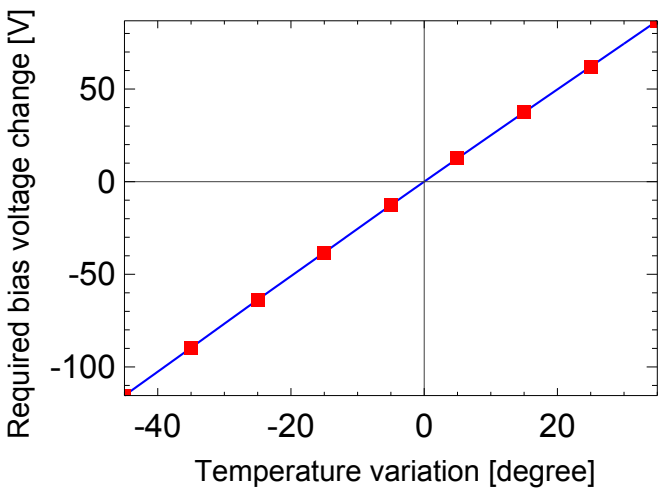

Fig. 2.15: Relationship between bias voltage change and temperature to hold a given gain.

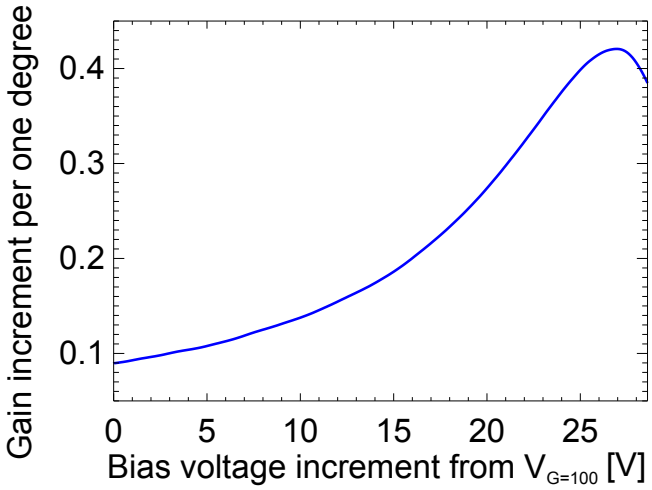

Fig. 2.16: Gain increment per one degree. $V_{G=100}$ represents the voltage where the gain equals 100.

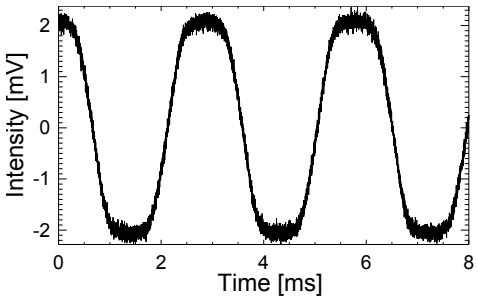

Fig. 2.17: Typical waveforms of a new APD under the setup shown in Fig. 2.10. Note that the oscillation is caused by a chopper.

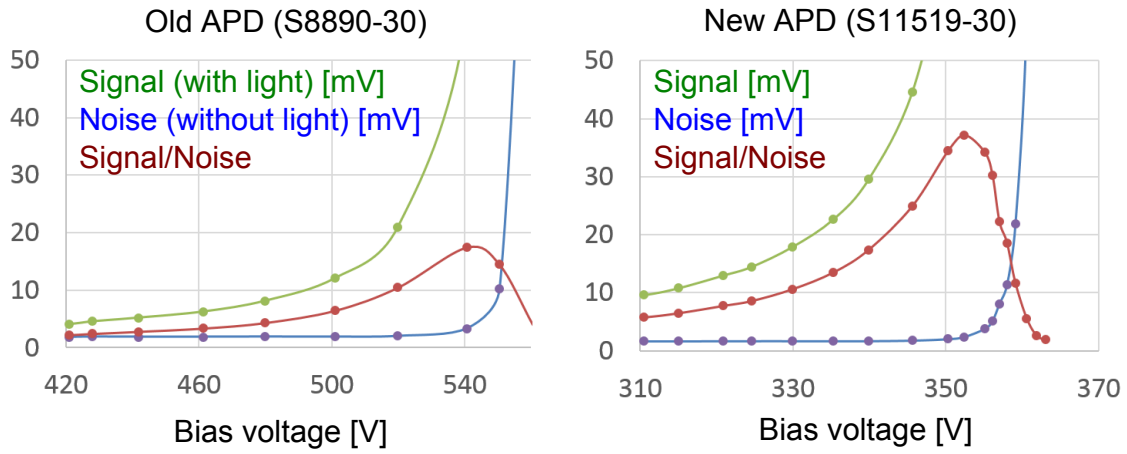

Fig. 2.18: Dependence of the signal amplitude (green), the noise amplitude (blue), and the SNR (red) on the bias voltage for the previous APD (left) and the new one (right).

voltage where gain becomes 100. The magnification of 2.4 is similar to the efficiency ratio of 2.5 calculated from the typical specifications. In addition, SNR in the optimum voltage for the new APD was 2.1 times larger than that for the previous one. Note that the influence of ambient temperature variation (±0.1 degree) and ripple in the bias voltage (±5 mV) were negligible, and the setup seems to be stable since the signal amplitude variation of another APD was within 4 % during the test. At the test, position and angle of each APD were optimized so that the whole focused light enter the effective area of each APD. Normalized Raman scattering signals for both APDs are shown in Fig. 2.19. Time response for the new APD is 17 ns (FWHM) and that for the previous one is 15 ns. The broader pulse width is not crucial to the present TS measurements.

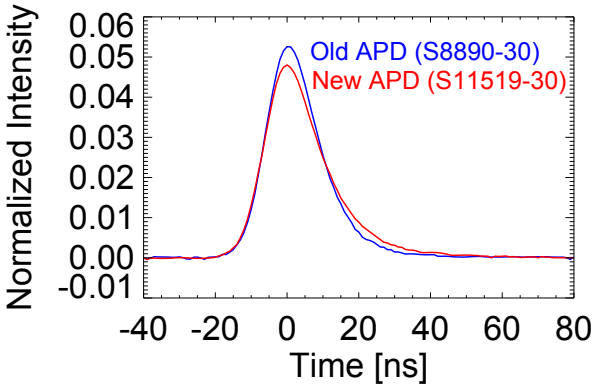

Fig. 2.19: Waveforms of the normalized Raman scattering signals detected by both APDs [48].

After the replacement, calibration of the polychromator using the spectrometer was performed, and the resultant sensitivity spectra are shown in Fig. 2.20. Absolute value of each wavelength channel is normalized by integrated value of the spectrum for channel #1, and spectra for the new APDs is additionally multiplied by the magnification of 2.4. Higher sensitivity and flatter spectrum around 1064 nm can be seen for the new APDs. Note that lower value for channel #5 indicates a constant bias voltage applied to the APDs is lower

than optimum voltage for channel #5.

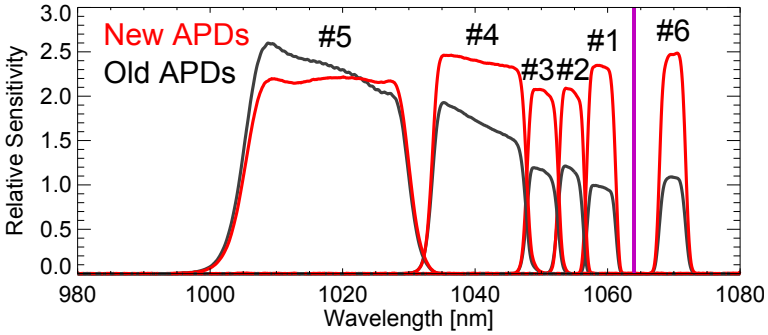

Fig. 2.20: Sensitivity spectra of the six (wavelength) channels in a polychromator with old APDs (black) and new APDs (red).

2.6.2 Multi-pass Thomson scattering scheme

In conventional (single pass) TS systems, the laser pulse is damped after passing through the plasma. On the other hand, the laser pulse is reused many times by making multiple round trips in multi-pass TS systems. As a result, multiple TS signals are obtained by one laser injection. When the round trip length is long (e.g. 150 m), TS measurement with a high time resolution (> 1 MHz) can be carried out. On the other hand, when time interval between adjacent round trips is much shorter than the time scale of T_e and n_e variations, accumulation of multiple TS signals is effective to improve the SNR. In addition, difference in temperatures for plasmas with anisotropic velocity distribution function can be measured in a special case (described in next section).

In TEXTOR, enhancement of probing laser energy by using a multi-pass TS system has been performed successfully for the first time [54, 55]. In the configuration, however, the laser beam path is slightly different at each pass in the optical system, where a laser pulse passes on non-coaxial paths. Thus, the number of passes is limited and it is difficult to improve the spatial resolution. Alternative scheme to solve the problems is utilization of a coaxial multi-pass system, where an optical cavity with a Pockels cell and a polarizer is used. Such systems were designed and tested on JT-60U, GAMMA 10, and so on [56–59], but no quantitative description of the performance was reported. In TST-2 TS system, where the optical system is compact, the coaxial multi-pass TS scheme could be used to improve the SNR in the TS measurement of low-density LHW-driven plasmas. Then, a coaxial multi-pass TS system was designed and tested, and performance of the system was evaluated from TS measurements for Ohmically heated plasmas [60–63].

For further improvement of SNR in the multi-pass TS scheme, a new optical system was designed, and it was tested by Raman scattering measurement [48]. The designed optical system is shown in Fig. 2.21. The cavity consists of the minimum necessary components, i.e., two concave mirrors, two Brewster windows, a Pockels cell, and a PBS. Here, the Pocklels cell is upgraded to new one (PKC21-25, Inrad Optics) with a large diameter (25 mm) and high transmissivity (more than 98 %). The concave mirrors are also changed to those with f = 2000 and 3000 mm, and the interval is made longer than that of the previous cavity to extend the permissible maximum discharge time in the applied voltage to

the Pockels cell and to avoid the laser pulse from going out of the cavity. In order to increase the injection laser energy, the laser pulse firstly enter the plasma without meeting mirror #1. In addition, the Pockels cell driver was modified to solve the problem of remaining voltage (see Ref. [60]). The new circuit is shown in Fig. 2.22. In this circuit, a power supply is added to adjust the offset voltage to the Pockels cell. In order to confirm the successful control of polarization, the light passing through the PBS in the backward path was measured by a photodiode (the setup is shown in Fig. 2.21). Then, the two supplied voltages were optimized so that the remaining voltage to the Pockels cell becomes 0 V, and the amount of the return light becomes the minimum. As a result, the intensity of the returned light was less than 1 % of the laser power injected into the cavity. Therefore, it is demonstrated that polarization of the laser is controlled by the Pockels cell successfully. Note that the power level of 1 % would not damage the laser rod.

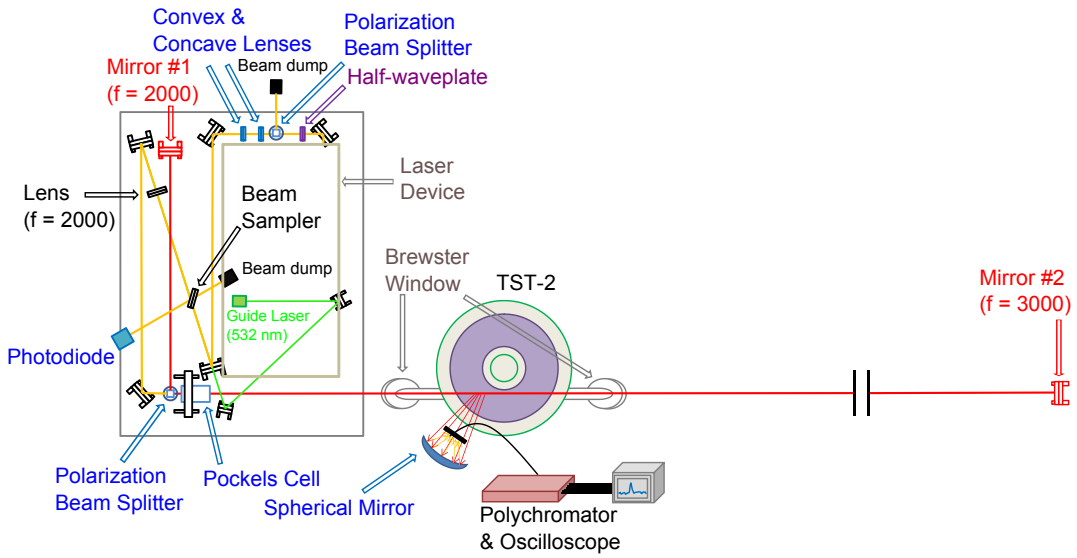

Fig. 2.21: A schematic drawing of the upgraded multi-pass TS optical system. Position and size of the components except for those on the optical bench are not precise.

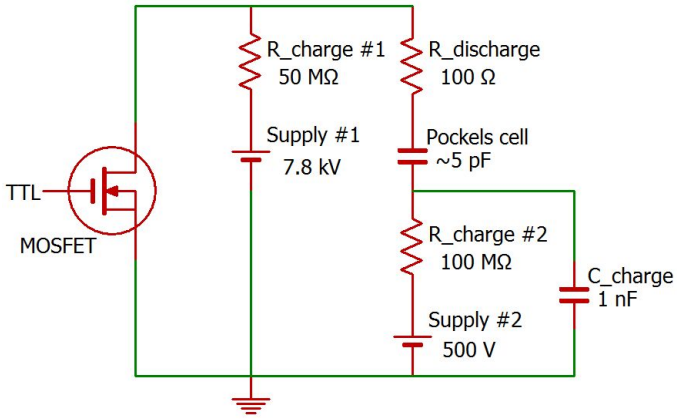

Fig. 2.22: Circuit diagram of a new Pockels cell driver.

Multi-pass Raman scattering measurements were performed to evaluate the performance of the cavity. Figure 2.23 shows the obtained signal, which is averaged over 256 laser shots. The figure also shows the fit obtained by summing the template waveforms whose amplitudes are adjusted to reproduce the signal. The total intensity becomes 10 times higher than that for the first one. Hereafter, this enhancement (as a function of accumulation number) is referred to as an effective gain (Fig. 2.24). Estimated loss for each round trip was around 20 %.

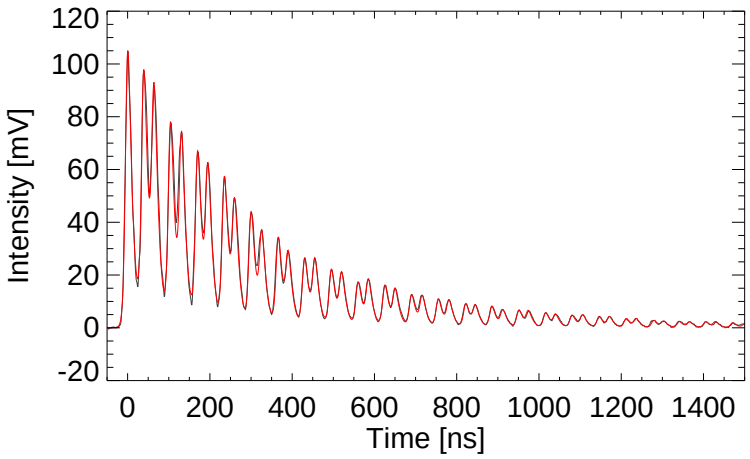

Fig. 2.23: Multi-pass Raman scattering signal (black) and the fit (red) [48].

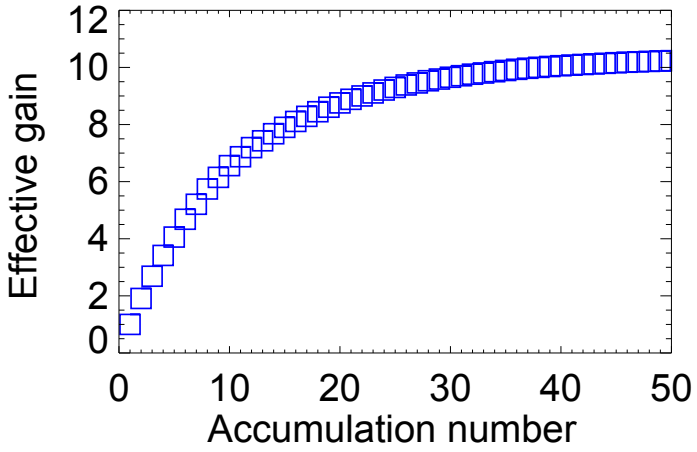

Fig. 2.24: Effective gain as a function of accumulation number.

Figure 2.25 shows the calculated SNR for the background noise dominant case described above. In our system, T_e anisotropy can be measured (the detail is described later). Thus, the forward and the backward signals should be analyzed independently to resolve the anisotropy. Each SNR becomes the maximum by accumulating the first five or six signals in each path, leading to 1.5 times higher SNR (blue and green squares in Fig. 2.25). For plasmas with isotropic T_e, both forward and backward TS signals can be used to obtain one Maxwellian distribution function. In that case, approximately 2 times larger photon number is expected, leading to further improvement of the SNR.

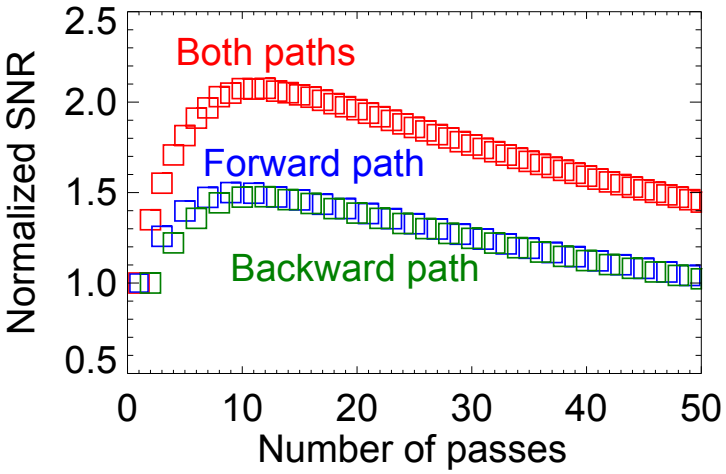

Fig. 2.25: Normalized SNR as a function of number of passes. Blue and green squares represent SNRs improved by accumulating multi-pass signals in the forward and the backward paths, respectively. Red squares show the case with a scattering angle of 90 degrees. Each SNR is normalized by that in the first pass [48].

In the present research, a coaxial multi-pass TS measurement system was developed and the performance was evaluated quantitatively. However, some problems in the optical system are still remaining. One of them is related to the beam profile of the YAG laser used

in the system. The profile is distorted and shows a hot spot, which is high energy density area, and the optical components can be damaged in the multi-pass scheme. In fact, a small spot of the damage at the PBS was seen two times in the multi-pass scheme with the injection energy of 0.8 J, while the PBS is tolerant to the Gaussian beam with the same energy and the same (expected) diameter as those of the YAG laser beam. One solution for this problem is the replacement of the laser by a laser without a serious hot spot. This is a future option. Deviation of the laser beam in the cavity from the coaxial path is found day-by-day, which leads to serious loss of the efficiency at more than several round trips. The deviation occurs due to unstable optical components (i.e., optical elements and the holder) used in TST-2. Since successful (non-coaxial) multi-pass scheme has been reported in TEXTOR, where more precise alignment is required, it is probably possible to improve the stability.

2.6.3 Double-pass TS scheme and temperature anisotropy measurement

Unlike the multi-pass TS scheme, a double-pass TS scheme, where the laser pulse makes only one round trip, does not require a complicated optical control. The optical system is almost the same as that of multi-pass scheme but mirror #1 is replaced by a beam dump (Fig. 2.26).

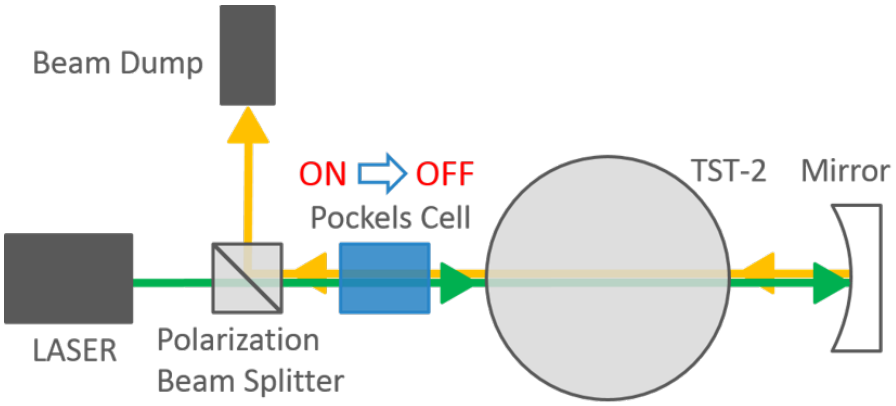

Fig. 2.26: A schematic drawing of a coaxial double-pass TS optical system.

In our system, T_e anisotropy in the direction of the magnetic field can be measured by applying a TS scheme, where the laser pulse makes more than one round trip. Figure 2.27 shows a schematic configuration of the magnetic field and the laser path in a TS diagnostic system. In TST-2, $\Delta\mathbf{k}$ for forward and backward paths are almost perpendicular and parallel to the magnetic field line $\mathbf{B}$, respectively. Since T_e in the direction parallel to $\Delta\mathbf{k}$ ($= \mathbf{k}_s - \mathbf{k}_i$ in the figure) is measured in TS diagnostic, $T_{e\perp}$ in the forward path and $T_{e\parallel}$ in the backward path are measured in TST-2.

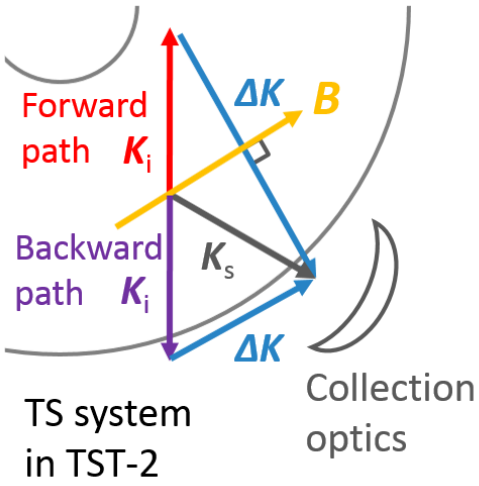

Fig. 2.27: A schematic diagram of a configuration of the magnetic field and the laser path in TS diagnostic.

In the past, a double-pass TS measurement system has been developed in TST-2, where a convex lens and a concave mirror are used and the laser pulse makes a round trip along non-coaxial paths. Using the system, the anisotropy measurement for Ohmically heated plasmas and test for in-situ calibration of spectra of the interference filters in the polychromator have been performed successfully [64–70]. In the present research, the coaxial double-pass TS system with higher spatial resolution and reliability owing to the coaxial path was applied to investigate the anisotropy in the LHW-driven TST-2 plasmas.

Chapter 3

Development of hard X-ray diagnostics on TST-2

3.1 Principle of hard X-ray measurement

Spectrum of Bremsstrahlung X-ray photon in a Maxwellian plasma is described by the following equation [71].

$$4\pi j(\nu) = {n_\mathrm{e} n_\mathrm{i} Z_\mathrm{eff}}^2 \left(\frac{e^2}{4\pi\epsilon_0}\right)^3 \left(\frac{32\pi^2}{3\sqrt{3} m_\mathrm{e}^2 c^3}\right) \left(\frac{2m_\mathrm{e}}{\pi e T_\mathrm{e}}\right)^{1/2} \exp\left(-\frac{h\nu}{eT_\mathrm{e}}\right) g_\mathrm{f}, \tag{3.1}$$

where ν, n_e, n_i, T_e, Z_eff, ϵ_0, $\mathrm{m_e}$, c, T_e, h and g_f are the frequency of the X-ray photon [Hz], the electron and ion densities [m^{-3}], electron temperature [eV], effective ion charge number, vacuum permittivity [F/m], speed of light [m/s], Planck constant [m^2 kg/s], and the Gaunt factor (approximately unity), respectively. The unit is photon number per unit frequency (energy) per unit volume per unit time. Figure 3.1 shows angular distribution of Bremsstrahlung from an electron with different energies, which depends on initial vectors of velocity and acceleration of the electron. In fusion research, measurements of hard X-ray (HXR) photons with energies higher than about 10 keV have been performed to investigate the behavior of fast electrons. In particular, HXR diagnostics is often applied to a plasma driven by the LHW which produces fast electrons [72–75]. Such high energy components cannot be measured by TS diagnostics, and then HXR diagnostics becomes effective means to study the LHW. Spatial profile and energy spectrum of HXR photons are related to the deposition profile and wavenumber spectrum of the LHW. The typical detection schemes are a semiconductor detector and the combination of a scintillator and a photomultiplier tube (PMT).

3.2 Configuration

3.2.1 Components

In this research, an HXR diagnostic system with high spatial and energy resolutions has been developed in order to measure the emission profiles and the energy spectrum of HXR. These are necessary to obtain detailed information on the propagation and absorption of LHW. The system consists of an NaI(Tl) scintillator with the diameter and width of one

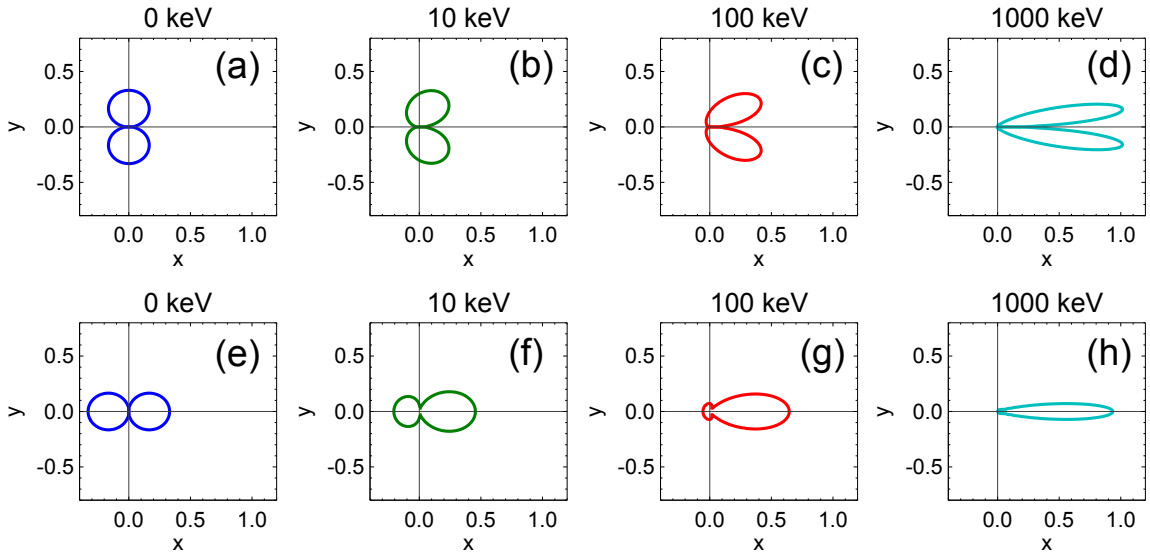

Fig. 3.1: Angular distributions of Bremsstrahlung from an electron with energies of 0, 10, 100, and 1000 keV. In (a)-(d) both the initial velocities and the accelerations are along x-direction. In (e)-(h) the initial velocity vectors are along x-direction and the accelerations are along y-direction.

inch (Type 4B4, OKEN (see Fig. 3.2)) and a PMT with the effective photoelectric surface diameter of 25 mm (H10426, Hamamatsu photonics (see Fig. 3.3)). The vacuum vessel of TST-2 is made of 6 mm thick SUS304, which blocks HXRs with energies less than about 10 keV. We use a viewing port with a 3 mm thick borosilicate glass window, which shows a higher transmissivity for HXRs. Energy dependence of the transmissivity of the glass window is shown in Fig. 3.4. Measurement chords are located on the midplane of TST-2. All the chords do not look at large plasma facing components (PFCs) such as outboard limiters or RF antennas, where large amount of HXR is radiated from the surface due to collision of electrons with the PFC. Such HXR radiation often becomes non-negligible background noise in HXR measurements.

Many of the supporting, connecting, holding components used in the system are made by a 3D printer (BS01+, bonsai lab. (see Fig. 3.5)). The 3D printer enables us to make the components quickly, which are sometimes difficult to be made in machine work.

3.2.2 Light transmission by a lightguide

Since the PMT gain is sensitive to the ambient magnetic field, it should be located far from the coils. On the other hand, there is a TF coil around the line-of-sights in TST-2, and it is difficult to have many chords with a conventional system located outside the TF coil (configuration and name of the coils in TST-2 are defined in Fig. 4.2). The effect of the ambient magnetic field on PMTs is a common problem not only for HXR diagnostics but also for neutron diagnostics. In the past, optical thin fibers and thick solid (straight) lightguides were used to avoid influence of the magnetic field [73, 76, 77]. However, the fiber can deteriorate the detection efficiency and SNR may become poor in the present scheme. In addition, the straight lightguide is not suitable for our case. In the present study, then, schemes using two types of lightguides are considered, i.e., a thin flexible liquid lightguide and a thick solid (curved) acrylic lightguide. In both schemes, the scintillator is located

Fig. 3.2: NaI (Tl) scintillator (Type 4B4, OKEN) used in the experiments.

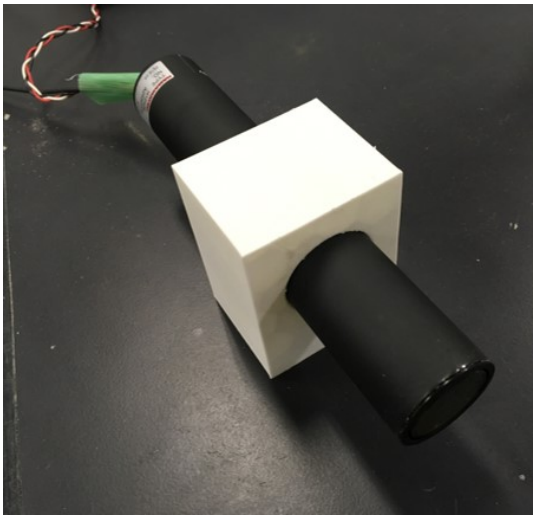

Fig. 3.3: Photomultiplier tube (H10426, Hamamatsu photonics) used in the experiments.

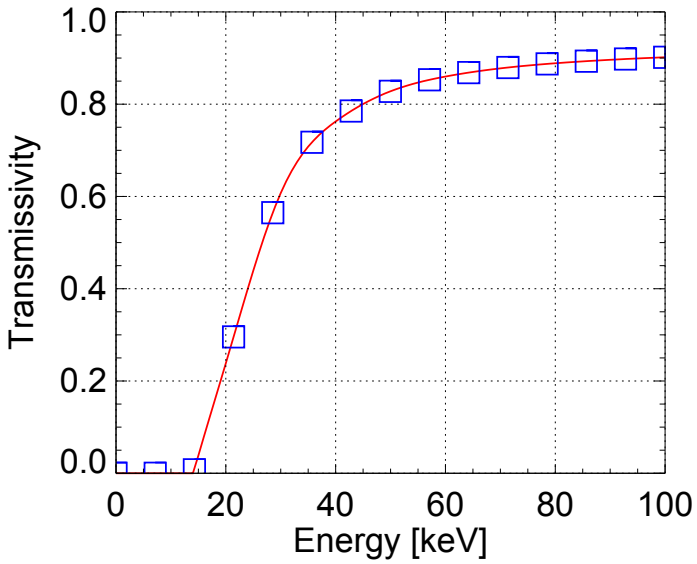

Fig. 3.4: Transmissivity of hard X-ray for a 3 mm thick borosilicate glass.

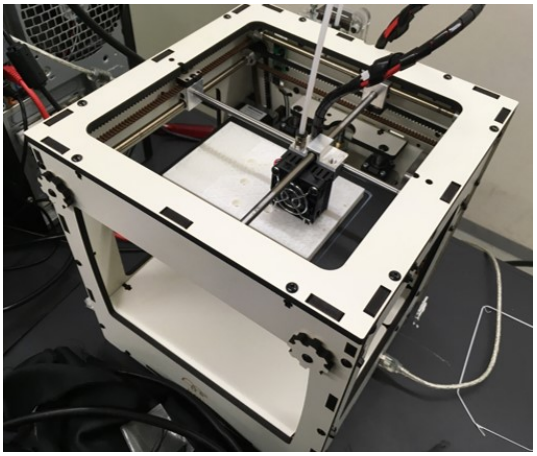

Fig. 3.5: 3D printer (BS01+, bonsai lab.).

inside the TF coil, and the scintillation light is transmitted by the lightguide to the PMT located far from there. As a result, the thick solid lightguide was adopted because of the high efficiency. Plasma experiments were performed in the system. The remaining part of this section is devoted to the theoretical studies on each lightguide.

First, the thin flexible lightguide was tested. Since such lightguide is versatile, it is easy to use and easy to get it with low-cost. However, the diameter is much smaller than that of the scintillator, and then large amount of the scintillation light is lost, leading to the deterioration of energy resolution due to noises. The diameter of a flexible liquid lightguide used in TST-2 (Edmund optics, #53-691) is 5 mm. Thus, the efficiency at the joint is approximated by the area ratio $S_{\text{lightguide}}/S_{\text{scintillator}} = \pi r^2_{\text{lightguide}}/\pi r^2_{\text{scintillator}} = (2.5\text{ mm})^2/(12.7\text{ mm})^2 \sim 4\%$, which can cause crucial difficulty in the HXR measurements. In order to improve the efficiency, utilization of a connection light guide, which is attached between surfaces of the scintillator and the lightguide, was considered. This connection lightguide has a truncated cone shape and each diameter at the top and bottom sides is the same as that of the two surfaces to be connected. The connection lightguide is made of acrylic glass (PMMA). In order to investigate the efficiency of the connection lightguide and determine the optimum length, 3D ray tracing simulation was performed. Figure 3.6 shows the position and vector of simulated rays at the incident surface of the connection lightguide. Refractive indexes for the scintillator, the connection lightguide, and the flexible lightguide are 1.85, 1.51, and 1.45, respectively. Note that optical grease with the refractive index (N = 1.45) is applied at each joint surface. In the simulation many light sources, each of which is characterized by the starting position (blue points in Fig. 3.6) and the initial direction of the ray, are selected at random. Figure 3.7 (a) plots position of rays at the incident surface (blue) and position of rays which reach the exit surface (red). Examples of the ray tracing expressed in one dimension is shown in Fig. 3.7 (b). It can be seen that almost all of the rays can not reach the exit surface. Efficiency of the connection lightguide, i.e., transmissivity is obtained

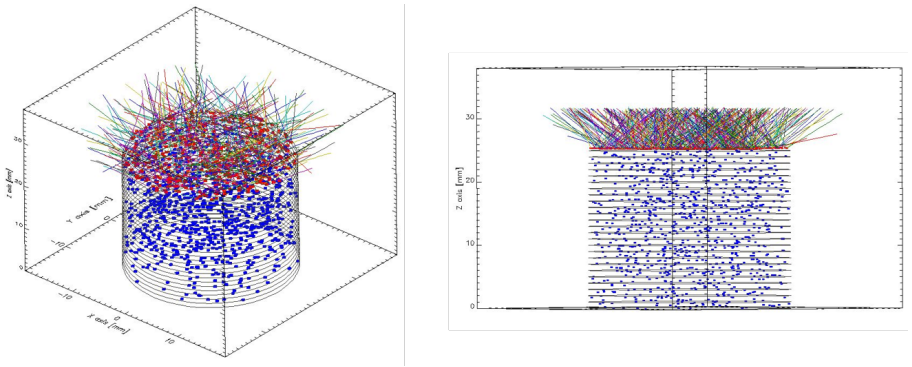

Fig. 3.6: Simulated light rays emitted from the surface of an NaI scintillator.

from the simulation, and lightguide length dependence of the transmissivity is represented in Fig. 3.8. The transmissivity becomes maximum at the length of 8 mm and the value is approximately 6%. The resultant transmissivity is very low and not so different from the transmissivity of 4 % in the case without lightguide. Therefore, the combination, where the connection lightguide and the flexible lightguide are used, is not adopted.

Secondly, a thick solid lightguide, where higher efficiency is expected, was considered instead of the thin flexible lightguide. When a straight lightguide is used, a TF coil interferes

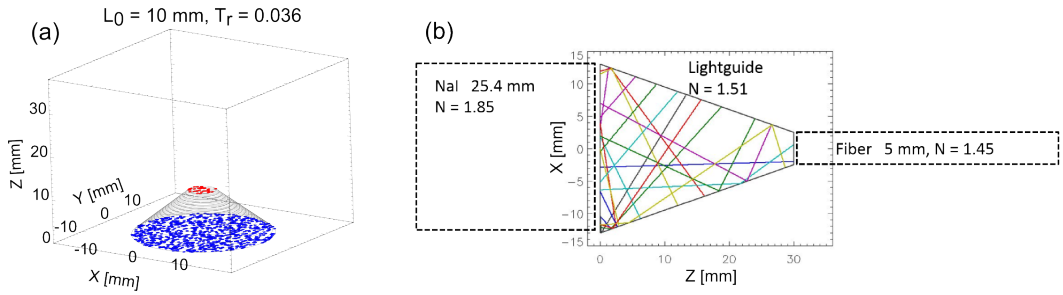

Fig. 3.7: Rays in a connection lightguide inserted between the scintillator and the lightguide. Refractive indexes for the scintillator, the connection lightguide, and the flexible lightguide are 1.85, 1.51, and 1.45, respectively.

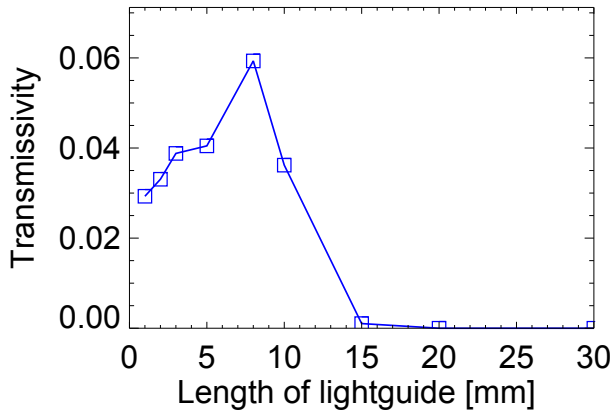

Fig. 3.8: Total transmissivity as a function of the length of the connection light guide.

with the optical path. Thus, the lightguide should be curved. In order to investigate the characteristics of a curved lightguide and to determine the optimum shape for the HXR measurements in TST-2, similar simulation was performed. As a matter of convenience, straight and curved sections are separated in the simulation. Diameter of the lightguide is set to be 25 mm. Figure 3.9 shows setup of the ray tracing simulation. The lightguide consists

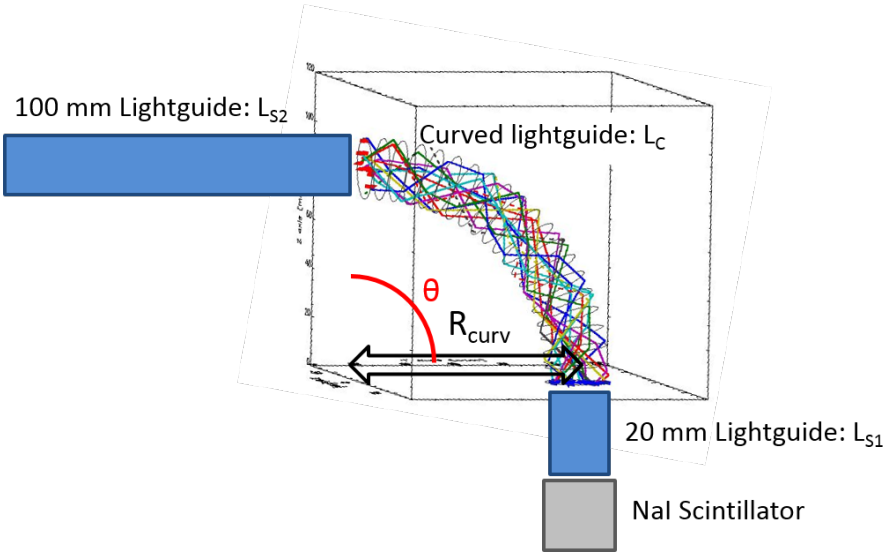

Fig. 3.9: Rays in a curved lightguide. The definitions of θ and R_{curv} are shown. The short and long lightguides and the curved one are referred as L_{S1}, L_{S2}, and L_C, respectively.

of 20 mm straight section L_{S1}, curved section L_C with the curvature radius R_{curv} and the angle θ, and 100 mm straight section L_{S2}. First, curvature radius dependence of the transmissivity was checked with a fixed angle ($\theta = 90°$). Figure 3.10 shows the result in three cases: (1) only L_C, (2) L_C and L_{S2} , and (3) whole lightguides. As a result, transmissivity becomes higher as curvature radius increases for all cases, but the difference is not significant. Since lightguides with large R_{curv} are expensive due to some difficulties in processing, the shortest R_{curv} was adopted. Then angle dependence of the transmissivity for small and large R_{curv} cases is simulated as shown in Fig. 3.11. In both cases ((a) and (b) in Fig. 3.11), total transmissivity becomes lower as the angle θ increases, and the decrement in the small R_{curv} case is larger than that in the large R_{curv} case. Thus resultant angle θ is determined to be 40°, where the smallest permissible θ of 35° and a little margin of 5° are taken into account.

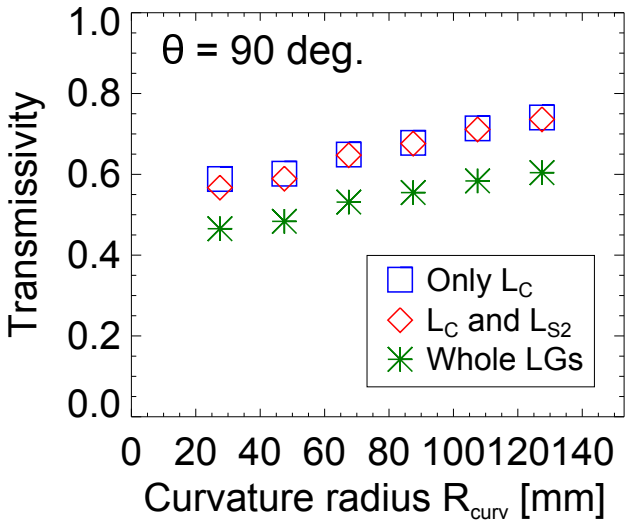

Fig. 3.10: Curvature radius R_{curve} dependence of the transmissivity. Angle θ is fixed at 90 degree. Blue squares represent the transmissivity for the curved section alone, red diamonds represent that for the lightguides including two straight sections, and green asterisks represent the total transmissivity including loss at the scintillator surface due to the difference of diameters for the lightguide and the scintillator.

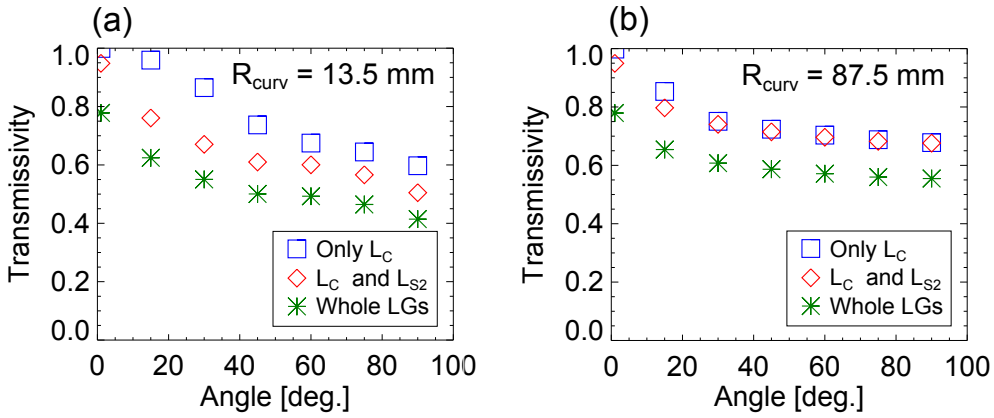

Fig. 3.11: Angular dependence of a curved lightguide. Curvature radius R_{curv} is fixed to be 13.5 mm (a) and 87.5 mm (b), respectively.

3.2.3 Degradation of PMT gain due to magnetic fields

Figures 3.12 and 3.13 show a schematic drawing and photographs of the present HXR measurement system, respectively. In order to mitigate degradation of PMT gain due to magnetic fields, the PMT is located at about 30 cm distance from the TF coil position. The influence is investigated here and Fig. 3.14 shows signals of Co-57 radioactive isotope with the peak of 122 keV detected by two systems with different PMT positions, i.e., 30 cm (a) and 10 cm (b) distance from the TF coil position. Under the TF coil current started from 8 ms, no significant perturbation in the signal is seen in the former case, while up to 70 % degradation is shown in the latter case. Detailed analysis for the former case is performed as shown in Fig. 3.15, and it is confirmed that effect on the photoelectron peaks is less than ±1 %. Note that when several types of coils are energized with currents similar to those in LHW-driven plasma discharges in TST-2, such perturbation is not shown in the former case (i.e., the present system).

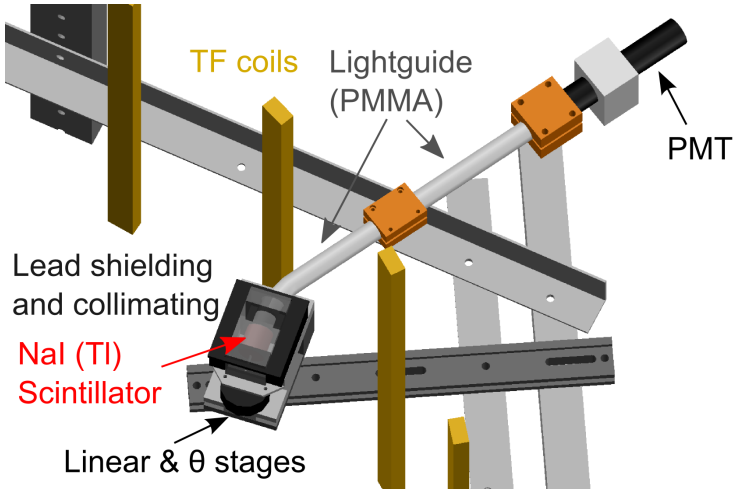

Fig. 3.12: A schematic drawing of a hard X-ray measurement system in TST-2.

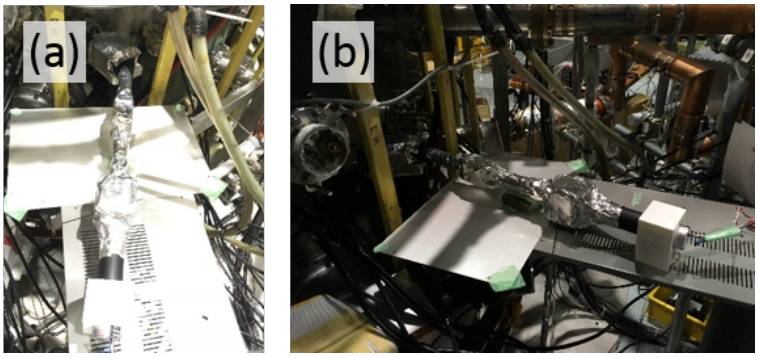

Fig. 3.13: Photograph of the HXR system installed on TST-2.

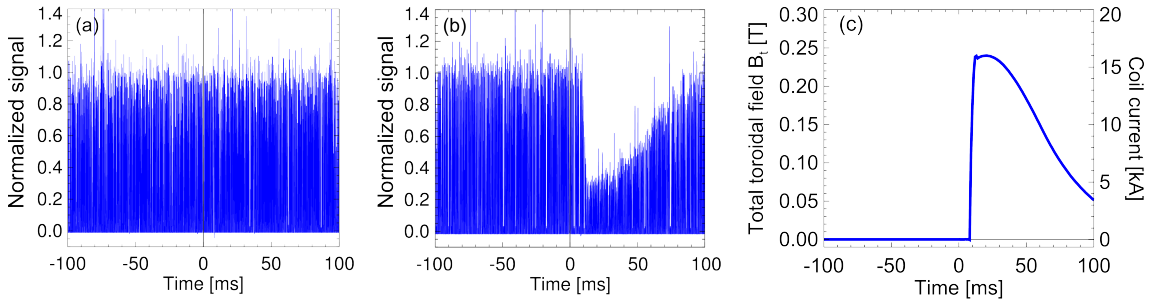

Fig. 3.14: Signals of Co-57 radioactive isotope ((a) and (b)) under the influence of the toroidal magnetic field (c), which starts from 8 ms. The distances between the PMT and a TF coil for (a) and (b) are about 30 cm and 10 cm, respectively, and the present system corresponds to the former case.

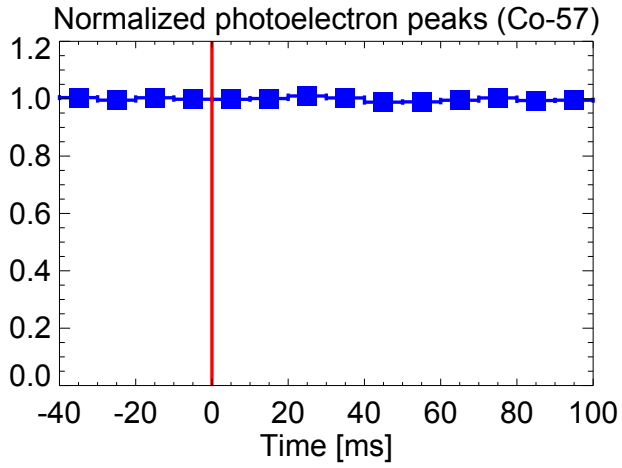

Fig. 3.15: Normalized photoelectron peaks of Co-57 radioactive isotope per 10 ms obtained by using the present system under the influence of the toroidal magnetic field, which starts from 8 ms. Perturbation of the peaks is less than ±1 % and significant degradation of the PMT gain is not shown.

3.2.4 Collimation and shielding

Front part of the system is shown in Fig. 3.16. The scintillator is shielded by lead with the width and height of 50 mm × 50 mm. Pinhole part with 20 mm thick is removable and pinholes with the diameter of 2, 3.5, and 5 mm are prepared. Thickness of the lead shielding in this system is in the range of 8–20 mm except for a hollow lightguide insertion space with the length of 40 mm. Figure 3.17 shows energy dependence of HXR transmissivity of lead shields with different thicknesses. Effective electron temperature of 50 keV was obtained in the previous system, where simple HXR measurement is available by a set of the scintillator and the PMT located several meters far from the vacuum vessel. In such plasmas, since fast electrons with more than 200 keV hardly exist, the thickness of 8 mm is sufficient to shield the scintillator from HXR photon. The front part can be rotated (with the rotation axis located at the center of pinhole exit) by using a θ stage. A linear stage is also equipped to guarantee a wide range of tangency radius R_{tan}, which is defined in Fig. 3.18. The linear-stage enables the system to move in parallel to the window surface of the port. Sample set of measurement chords in the experiment is represented in Fig. 3.19. In order to confirm the actual chords, a calibration system including a pinhole and a visible laser was developed as shown in Fig. 3.20. The measurement angles agree well with those obtained from the drawing (Fig. 3.21 (b)). Relationship between θ and R_{tan} is plotted in Fig. 3.21 (a).

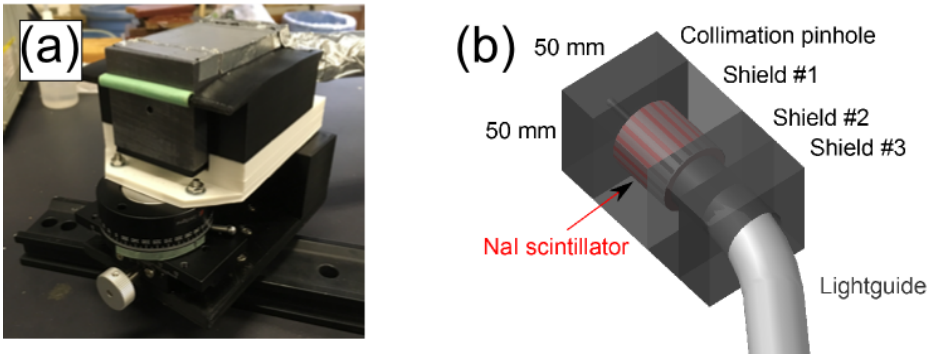

Fig. 3.16: A photograph (a) and a schematic drawing (b) of front part of the HXR system. The part consists of lead blocks for collimation and shielding, a theta stage, and a linear stage.

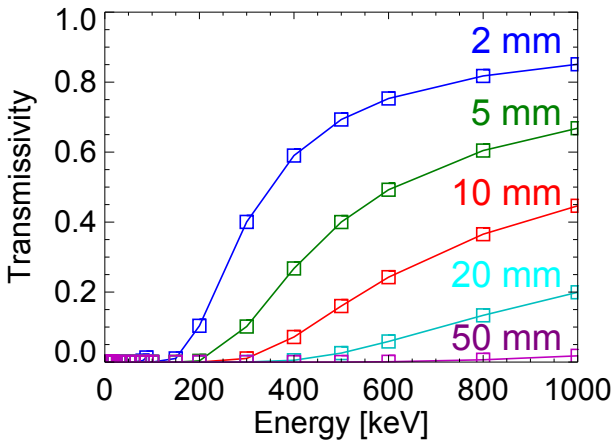

Fig. 3.17: Transmissivity of hard X-ray for lead blocks with the thickness of 2, 10, 20, and 50 mm.

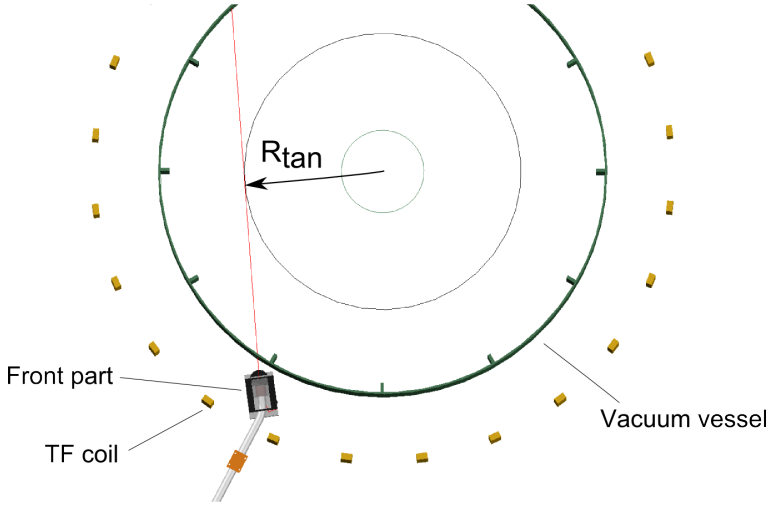

Fig. 3.18: Definitions of tangency radius R_{tan}.

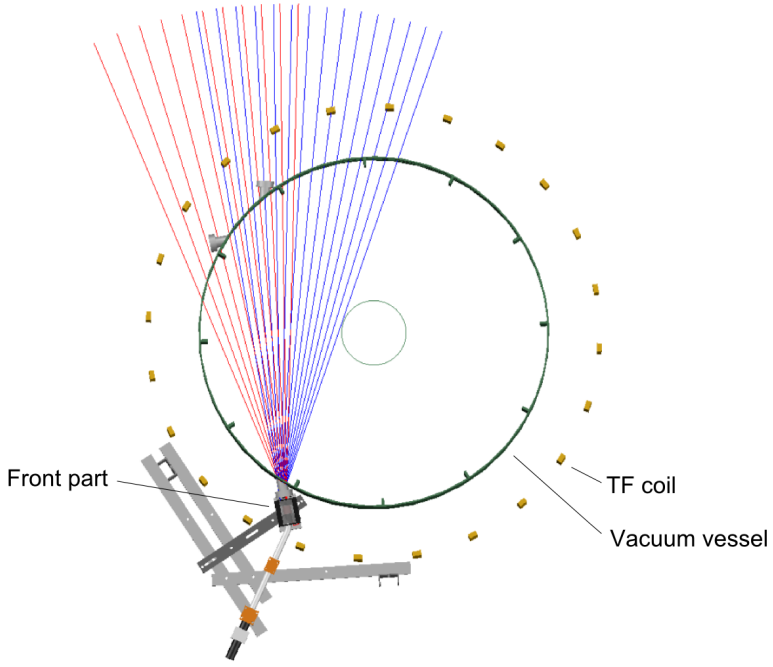

Fig. 3.19: Example sets of measurement chords in the HXR system. The linear stage position can be changed to cover a wide range (e.g. red chords and blue chords).

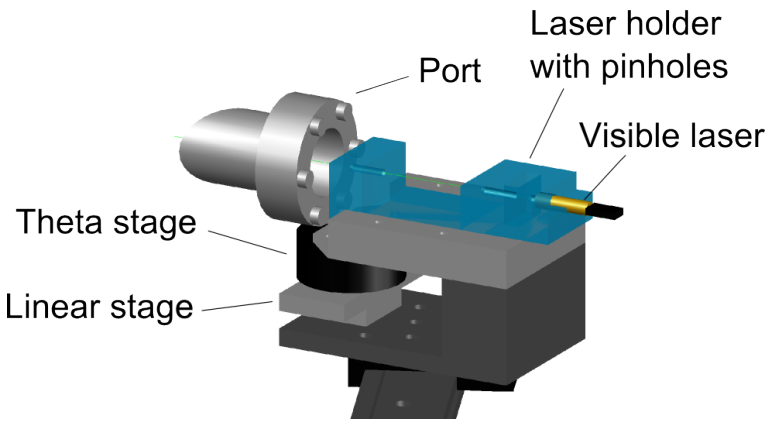

Fig. 3.20: A schematic drawing of the line-of-sight calibration system for HXR diagnostic.

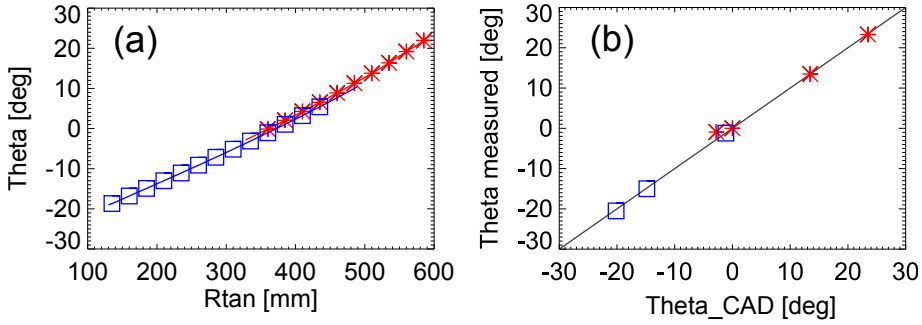

Fig. 3.21: Result of line-of-sight calibration for two sets of measurement chords (red asterisks and blue squares). Each tangency radius of the symbol corresponds to the measurement chord in Fig. 3.19 and the curve shows the measurement range. (b) represents measured theta (symbols) and the setting theta. The black line indicate the ideal case.

3.3 Data acquisition and analysis

Since the time scale of photoelectric effect is very short, pulse width of HXR signal is determined by the response times of the PMT and the circuit. The pulse width is about 1 μs (see Fig. 3.22). In order to detect each photon in the signal, we adopt the following 5 steps. (1) An analysis time window (typically 1 ms) is set and the offset is subtracted. (2) The maximum in the signal is found out and a pulse (i.e., a photon) to represent the maximum (i.e., a peak) is calculated by fitting a template function having freedoms of amplitude (height) and peak time. Here a short time window of 0.2 μs before and after the maximum is used for the fitting to search the true peak time. (3) The obtained peak time and amplitude are stored. (4) The fitting function representing the peak is subtracted from the whole signal. (5) The process returns (2) if the maximum in the remaining signal is still higher than a given threshold value. The stored times and amplitudes of detected HXR photons are used for the analysis. In order to judge whether the photon detection is reasonable or not, a judgment coefficient (JC) is used, where JC is defined as the standard deviation of the residual σ_r normalized by average amplitude of the fitting function μ_N, and this is expressed as unit of the percentage, i.e., JC = $\sigma_r/\mu_N \times 100$. The upper limit of JC is set to be 50 % in the analysis. Therefore, peaks with JC of less than 50 % are used in the analysis. Peaks with JC of greater than 50 % are subtracted in (4), but those are not used in the following analysis. Figure 3.22 shows the fitting result for some pulses with different JCs. The time period to calculate JC is 0.8 μs, which covers the period where the fitted function is greater than $1/e^2$ of the peak. Note that since a pulse with higher amplitude is prior in the analysis, energy spectrum could be distorted if pulse pile-up (i.e., overlap) occurs frequently. Therefore, it is desired to suppress such pile-up. The effect of pile-up is discussed in later.

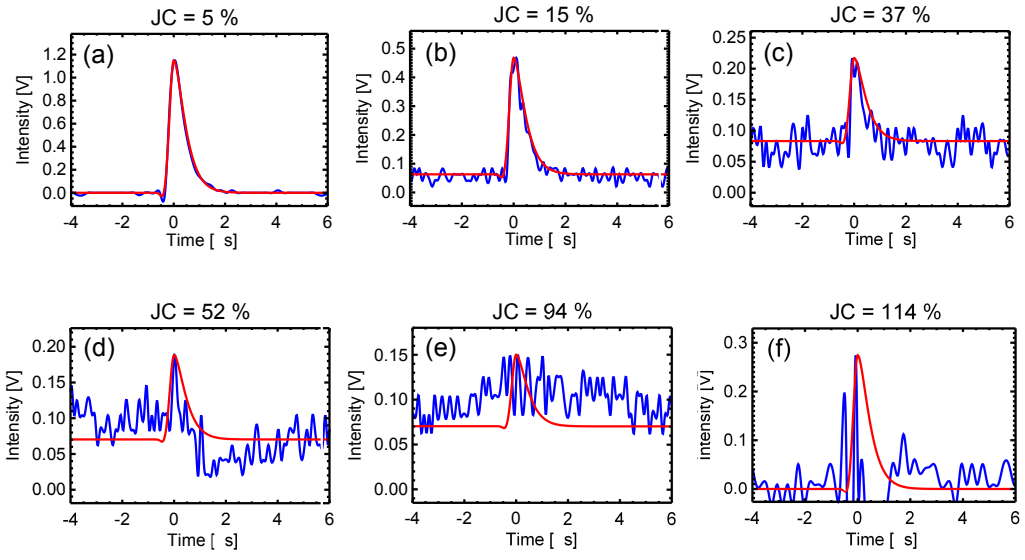

Fig. 3.22: Samples of fit to PMT signal waveform with different JCs. Signal with JC less than 50 % is counted as an HXR signal peak.

Figure 3.23 shows an example of the photon detection result for Co-57 radiation signal, and the enlarged views for Co-57, Ba-133, and Cs-137 are shown in Fig. 3.24. The resultant spectra using the detected photons are shown in Fig. 3.25. Since photoelectric peaks for

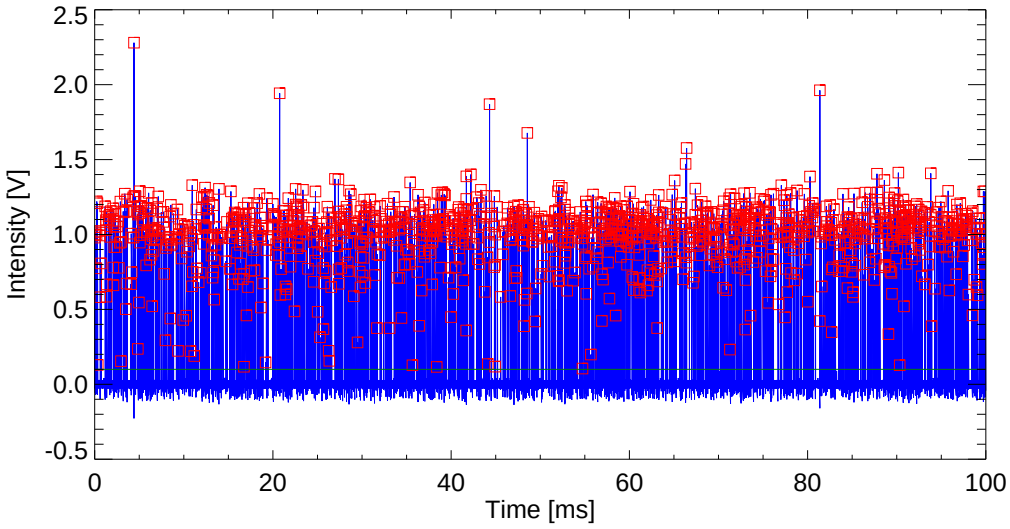

Fig. 3.23: Photon detection for Co-57 radiation signal. A horizontal green line shows the threshold value. The blue waveform shows the measured signal and the red symbols represent the detected pulse amplitudes.

Co-57 and Cs-137 are well known and seen clearly at 122 and 662 keV, respectively, energy calibration was performed by using the peaks, which are derived from Gaussian fit to the photoelectric peak in the spectrum. Figure 3.26 shows the calibration result and the relative error, which is defined as the full width at half maximum (FWHM) of the Gaussian fit. The horizontal axes in Fig. 3.25 are expressed in energy using this calibration result. The vertical green lines represent expected photoelectric peaks for each radioactive isotope. The relationship between energy E_{HX} and voltage V_{HX} in the system is slightly different from a linear function and it is expressed as a power function, i.e., $E_{\mathrm{HX}} = 67 \times V_{\mathrm{HX}}^{1.055}$. Energy resolution in the system is expected to be around ±10 % in the measurement range for TST-2 plasmas.

Performance test of lightguide was carried to compare the four cases: (1) without lightguide (scintillator is attached to PMT directly), (2) with a straight lightguide, (3) with a curved lightguide, and (4) with both lightguides (similar setup to that in the plasma measurements). Co-57 radiation was measured and the result is shown in Fig. 3.27. When all the signals are normalized by the voltage of the photoelectric peak for the case (1), efficiencies for the other cases (2)–(4) are calculated to be 48, 33, and 24 %. The efficiency of the setup in the plasma measurements (case (4)) is lower than that in the simulation by about twice. The unexpected loss may occur at the joint surface (connected by optical grease) and at the side surface of lightguide due to irregularity caused in machine work. Nevertheless, energy resolution is not so bad and the errors are within about ±10%. In addition, background noise due to the detection circuit and ambient light is similar to the bit noise in the data acquisition, and Co-57 signal intensity corresponding to 122 keV is about a hundred times greater than the noise level.

Here, distortion effect due to Compton scattering was investigated. When an HXR photon with 380 keV enters a scintillator, photoelectric peak occurs at the same energy. On the other hand, energy spectrum due to Compton scattering shows a continuum energy spectrum with an edge calculated by the Klein-Nishina's formula, and the energy range is lower

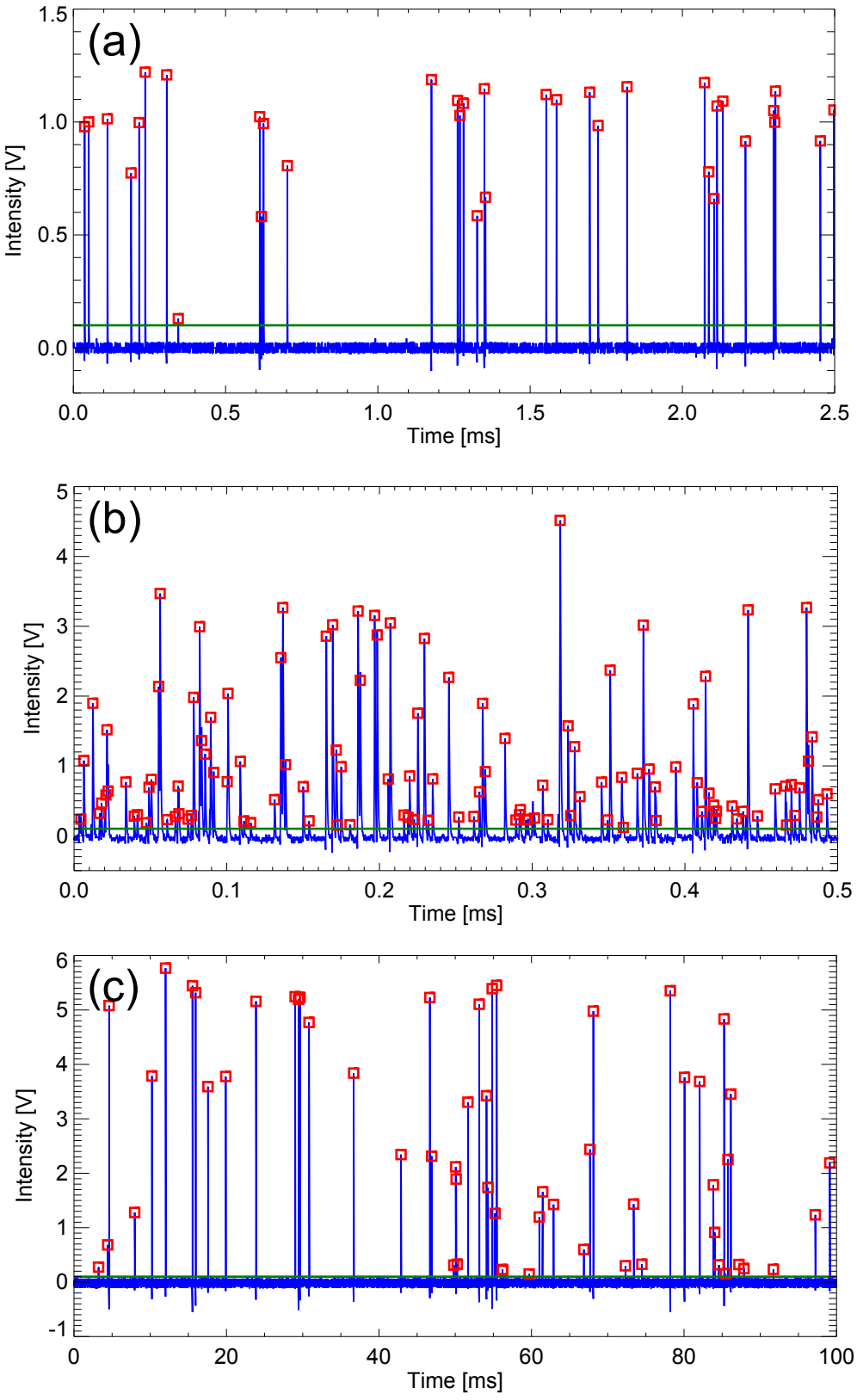

Fig. 3.24: Signal from Co-57 (a), Ba-133 (b), Cs-137 (c) with the peak points (red squares). Green lines represent the threshold in the photon detection.

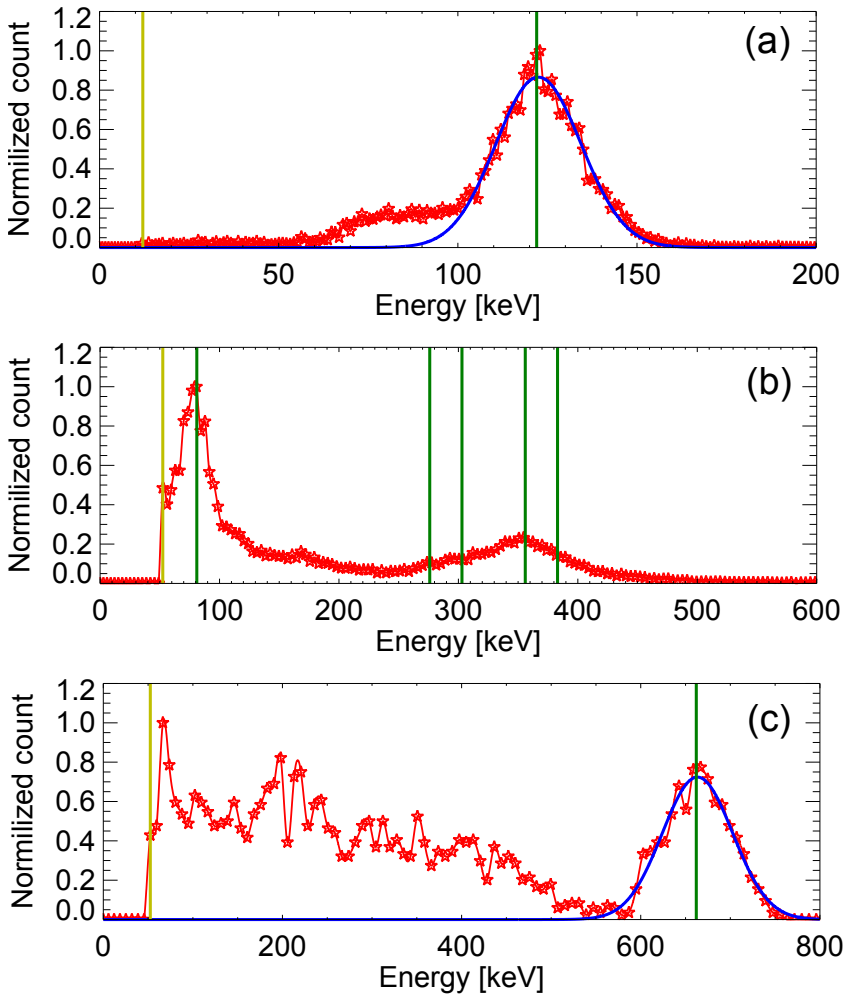

Fig. 3.25: Energy spectra of Co-57 (a), Ba-133 (b), and Cs-137 (c). Relationship between signal intensity and the energy was determined by the photoelectric peaks of Co-57 and Cs-137. Vertical green lines describe the major energies of Co-57 (122 keV), Ba-133 (81, 276, 303, 356, 383 keV), and Cs-137 (662 keV).

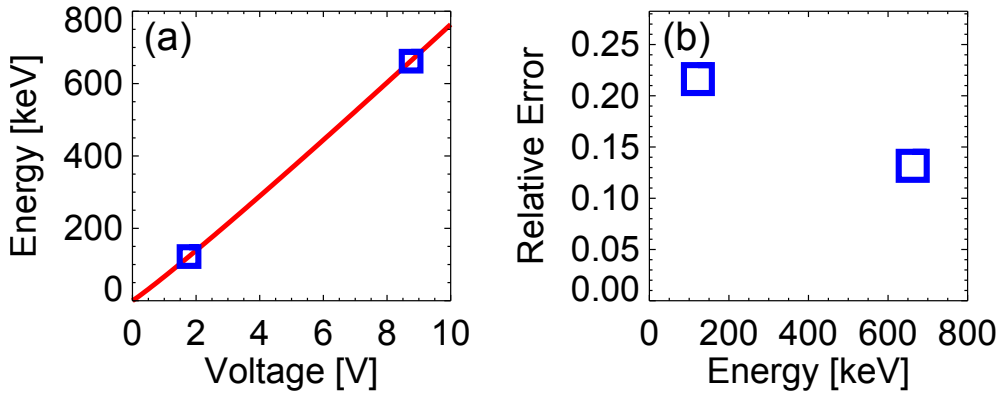

Fig. 3.26: Calibration result. Relative errors at 122 and 662 keV defined by the FWHM of the Gaussian fit to photoelectric peak for Co-57 and Cs-137 are plotted in (b).

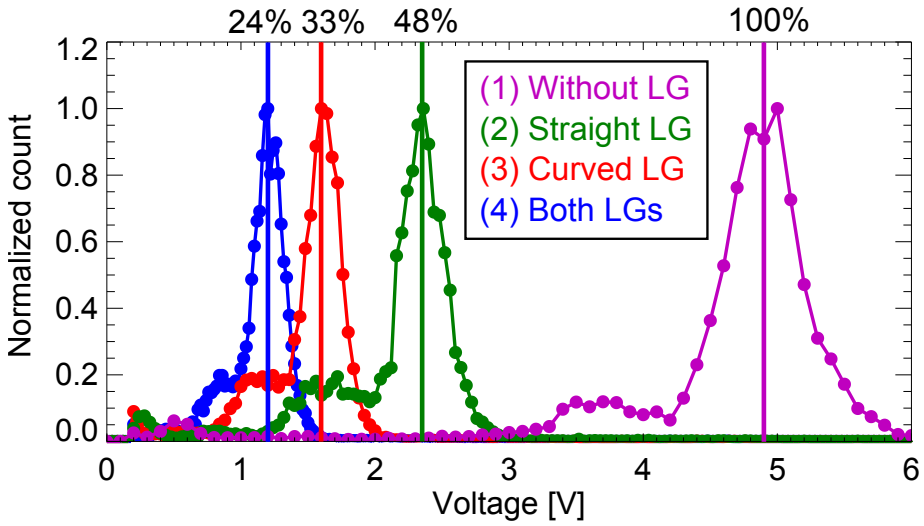

Fig. 3.27: Comparison of energy spectra of Co-57 in different setups: scintillator is attached to PMT directly (purple), through a straight lightguide (green), through a curved lightguide (red), through both lightguides (similar setup to that in the plasma measurements) (blue).

than the photoelectric peak (see Fig. 3.28 (a)). A ratio of cross section of the photoelectric effect to that of the Compton scattering is calculated as shown in Fig. 3.28 (b). This figure indicates that Compton scatting occurs more frequently in higher energy. Based on the ratio, the energy spectrum expected from scintillation light for a given energy spectrum was simulated. Four types of HXR energy spectra with different effective electron temperatures (50, 100, 500, and 1000 keV) were given. Each true (input) spectrum and simulated result are shown in Fig. 3.29. Remarkable distortion is not seen at low energies and the effect is not serious for the cases T_{eff} = 50 and 100 keV. On the other hand, since high energy HXR photons are more significantly (or heavily) affected by the Compton scattering, the distortion effect (flatting effect in low energy side) becomes significant for plasmas with T_{eff} = 500 and 1000 keV. However, reabsorption of the scattered X-rays is not taken into account in this simulation, and this effect should be included for such high energy cases.

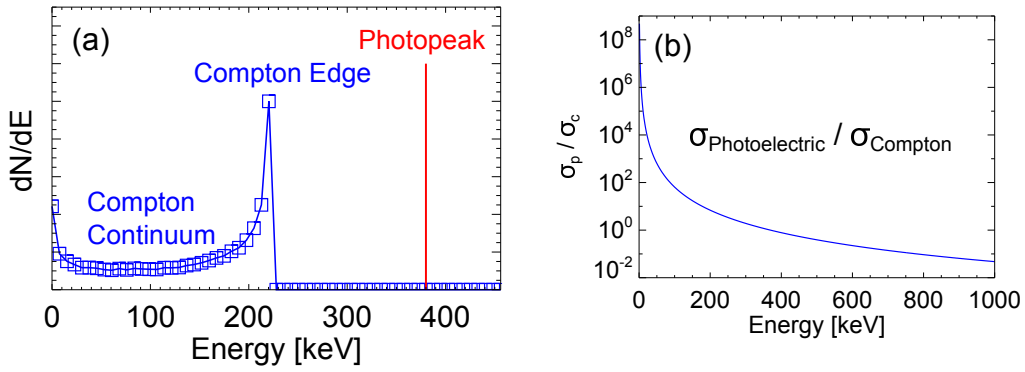

Fig. 3.28: A schematic drawing of an ideal energy spectrum for a X-ray source with the energy of 380 keV (a). (b) shows the ratio of scattering cross-section for photoelectric effect to that for Compton scattering.

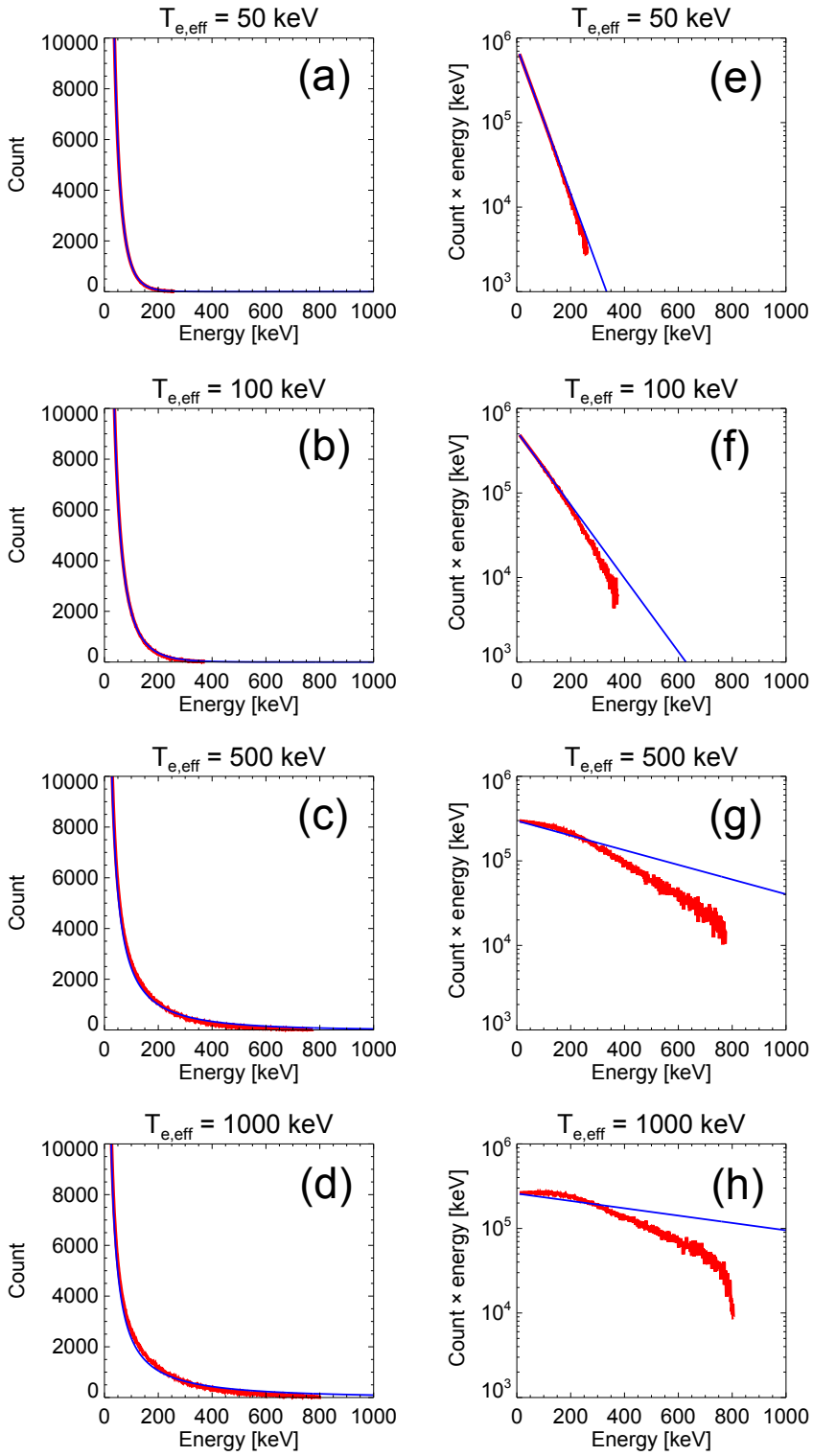

Fig. 3.29: Distortion of the energy spectrum due to the Compton effect for various effective temperature. Red data show the simulated values with the Compton effect and blue curves represent true spectrum.

In order to confirm validity of the analysis method and investigate characteristics of energy spectra obtained from pile-upped pulses, numerically generated pulses are analyzed. Simulated pulses with 1 μs width are generated so that each peak position with averaged pulse interval $\overline{\Delta t_{\mathrm{pulse}}}$ is selected at random and its amplitude is determined to obey Maxwell distribution function with a given effective temperature. Result of the simulation is shown in Fig. 3.30. In the case (a), each $\overline{\Delta t_{\mathrm{pulse}}}$ is set as 0.5 μs, where almost all of the pulses pile-up, and different temperatures are given (25, 40, 55, and 70 keV). Broken lines and diamonds in this figure represent the input energy spectra and the analysis result (output), respectively. Due to the pile-up effect, number of the pulses for higher energy is overestimated, while number of the pulses for lower energy is underestimated, leading to distorted spectra. On the other hand, it is indicated that the analyzed effective temperatures (slopes of the spectra) are similar to those of input spectra within the error of about 10 keV. Figure 3.30 (b) shows analysis result for input spectra with different $\overline{\Delta t_{\mathrm{pulse}}}$s (100, 10, 5, 2, 1, and 0.5 μs) and constant temperatures (50 keV). In the case of $\overline{\Delta t_{\mathrm{pulse}}}$ = 100, 10, and 5 μs, significant distortion of the spectra is not seen and input spectra seem to be reproduced. When $\overline{\Delta t_{\mathrm{pulse}}}$ approaches the pulse width or becomes more shorter, the spectrum is distorted as shown in Fig. 3.30 (a). Although total energy flux is ideally preserved, absolute value of energy flux obtained from pile-upped HXR signals is not analyzed due to the ambiguity. On the other hand, obtained effective temperature is used in the present analysis.

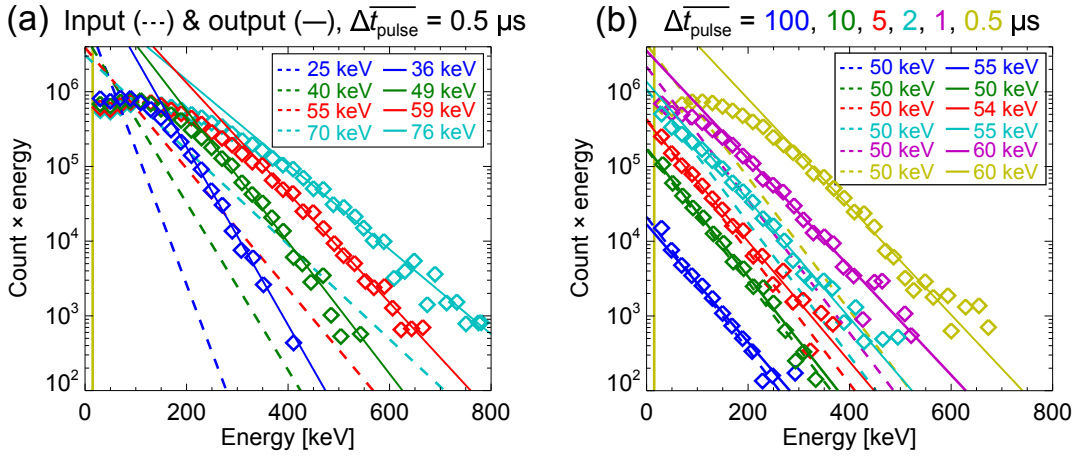

Fig. 3.30: Energy spectra analyzed from simulated HXR signals. Broken lines represent the input spectra and diamonds represent the output spectra with the slopes (i.e., analyzed effective temperatures) plotted as solid lines. These spectra are obtained from two types of conditions: different given temperatures (25, 40, 55, and 70 keV) and constant averaged pulse interval $\overline{\Delta t_{\mathrm{pulse}}}$s (0.5 μs) (a), and fixed temperatures (50 keV) and given $\overline{\Delta t_{\mathrm{pulse}}}$s (100, 10, 5, 2, 1, and 0.5 μs) (b).

Chapter 4

Experiments on TST-2

4.1 Experimental setup

The TST-2 spherical tokamak [78] was constructed at the University of Tokyo and various experiments have been performed since 1999. Figure 4.1 shows the photograph of TST-2. Typical parameters of TST-2 are as follows: major radius $R \leq 0.36$ m, minor radius $a \leq 0.23$ m, aspect ratio $A \geq 1.5$, toroidal magnetic field strength at the center of the plasma is $B_{\mathrm{T}} < 0.3$ T. For Ohmic discharges, typical plasma current is $I_p \sim 100$ kA and the discharge duration is $t_{\mathrm{pulse}} \sim 30$ ms. For the started-up discharges using LHW with the frequency of 200 MHz, $I_p < 25$ kA, and $t_{\mathrm{pulse}} \leq 100$ ms [26]. As shown in Fig. 4.2, 24 turns of the toroidal field (TF) coil are used for the generation of the toroidal field B_{T} and 239 turns of the Ohmic (OH) coil in the center stack of TST-2 are used for the Ohmic heating and current generation. 5 pairs of the poloidal field (PF) coils to sustain a tokamak configuration and a pair of horizontal (H) coils to control the vertical position of the plasma are installed around the vacuum vessel of TST-2. For the pre-ionization of the gas, we use electron cyclotron heating (ECH) whose frequency is 2.45 GHz and the maximum power is 5 kW.

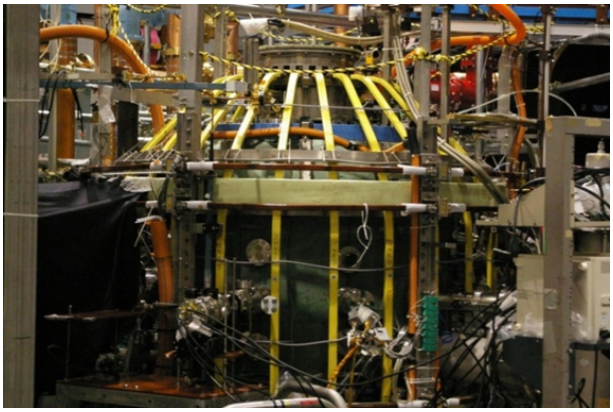

Fig. 4.1: Photograph of TST-2.

Plasma current for Ohmic heating is produced by the OH coil which is a solenoid coil located in the center stack of TST-2. The current passing through the OH coil induces magnetic fields inside OH coil. When the current varies over time, the magnetic field also

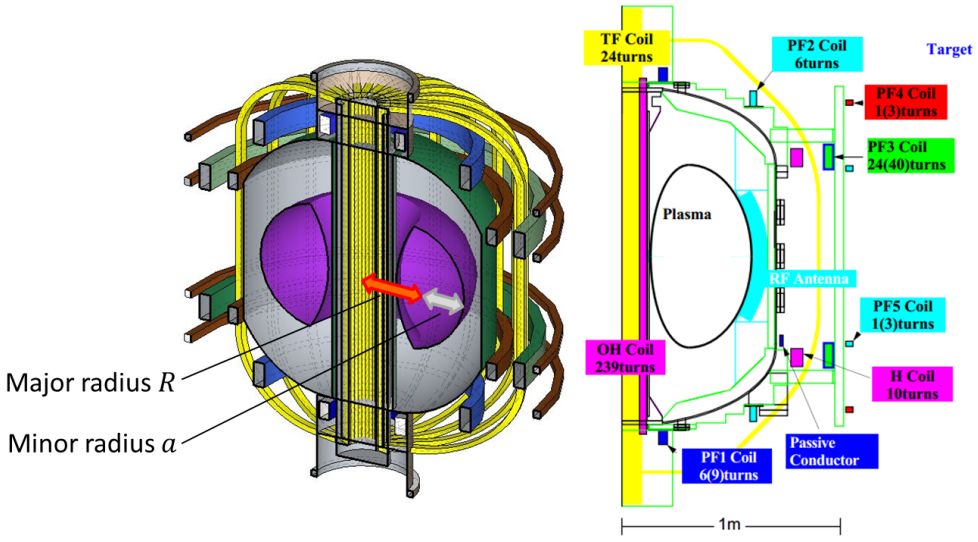

Fig. 4.2: Schematic drawing of TST-2.

shows temporal variation, and then the inductive electric field is produced along the toroidal direction by Faraday's law. The electric field generates plasma current I_p, and the plasma is heated by resistive dissipation (Ohmic heating). In order to maintain such a unidirectional current, the OH coil current must have a permanent unidirectional temporal variation, but this is not realistic. Moreover, since plasma resistivity is proportional to $T_e^{-3/2}$, the efficiency of Ohmic heating becomes low at high electron temperature.

In plasma, each electron moves along a magnetic field with gyro motion and the gyro-frequency is called the electron cyclotron (EC) frequency $\omega_{ce} = eB/m_e$. When the frequency of a wave is the same as the EC frequency of local electrons in the plasma, the wave is called electron cyclotron wave (ECW) and absorbed there. In Ohmic discharges, ECW is mainly used for pre-ionization. The lower hybrid wave can accelerate electrons along a magnetic field with high efficiency by the mechanism of Landau damping. Thus, LHW is usually used for the plasma current drive. In TST-2, two capacitively-coupled combline (CCC) antennas located at the outboard side on the midplane and at the topside of the plasma are used as the launchers of LHW (Fig. 4.3).

Various diagnostics are available or under development on TST-2. Electron density and temperature profiles are measured by the TS diagnostics. Line-integrated electron density is measured by a microwave interferometer. Plasma current, coil currents, magnetic fields, and magnetic flux are measured by several kinds of magnetic coils. Electron density, electron temperature, and floating potential in the edge region are measured by Langmuir probes. The temperature of impurity ions is measured by visible spectroscopy. Visible images of plasma can be acquired by a CCD camera. Line emissions from atomic hydrogen are measured by H_α and H_β monitors. Surface barrier diodes (SBDs), a p-intrinsic-n (PIN) diode, and absolute extreme ultraviolet (AXUV) diodes are used to measure photon emission, primarily in the soft X-ray region. As an energy filter for the SBDs, several thin films are placed in front of the SBDs. The films are made of aluminum, polypropylene, and beryllium, of which main transparent energy ranges are 10–70 eV, greater than 200 eV, and greater than 1 keV, respectively. The AXUV has a sensitivity range of 7–6000 eV. The tokamak equilibrium reconstruction code EFIT [79] is implemented and used to provide current profile parameters

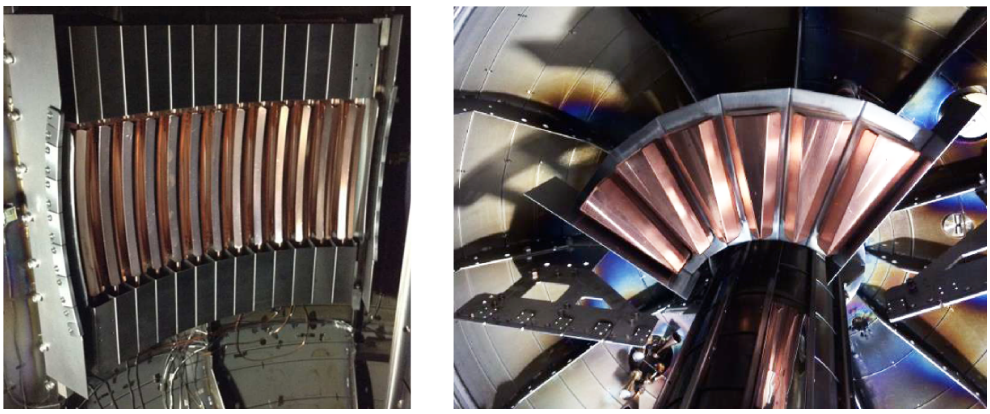

Fig. 4.3: Photographs of the outboard-launch CCC antenna (left), and the top-launch CCC antenna (right).

and plasma shapes in TST-2.

4.2 Non-inductively driven plasmas by LHW using outboard-launch CCC antenna

LH plasma current start-up experiments with the highest current in TST-2 is reported. The waveform is shown in Fig. 4.4. The plasmas are initiated by the ECW power of 3 kW and the currents are started-up and sustained by the 80 kW LHW excited using the outboard-launch antenna. Single pass TS measurements were performed for the plasmas. 7 TS signals from 7 discharges were averaged to improve the SNR and profiles with a total of 10 spatial points were obtained. Result of the profile measurements is shown in Fig. 4.5. A peaked n_e profile and a hollow T_e profile were obtained, and a flat p_e profile was shown. Temperatures both for the core region ($\sim$ 10 eV) and the inboard peripheral region ($\sim$ 50 eV) are obtained. Examples of the averaged TS signals and the results of the fitting to a Maxwell distribution function are shown in Figs. 4.6, 4.7, 4.8, and 4.9. Here, the backgrounds shown in each figure (black dotted curves) indicate the estimated noise including the stray light. Note that the backgrounds are estimated from the signals taken during laser injections after each discharge. It can be seen in Fig. 4.8 that the TS signals for R = 366 mm are fitted well to a Maxwellian distribution function with a temperature of about 10 eV. On the other hand, the TS signals for the two spatial channels at the inboard limiter side are relatively small as shown in Figs. 4.6 and 4.7. Nevertheless small peaks due to TS signals can be seen and the fittings (and the obtained T_es) seem to be valid within the errors. For the case of the spatial point R = 526 mm shown in Fig. 4.9, however, apparent TS signals cannot be seen, and the estimated values would be incorrect and thus it is not plotted in Fig. 4.5. In addition, TS signals at R = 459 mm cannot be also measured due to the significant stray light. Thus, electron temperatures at the outboard side were not available for this case, and it is desired to measure T_es there by eliminating stray light or using an alternative means (e.g. application of other line-of-sights where stray light is small). Purple vertical lines in the figure show the magnetic axes obtained from the EFIT code. Unlike results in the Ohmic plasma experiments (see Appendix A), each center position estimated from the profile seems to be located slightly inner side compared with the magnetic axis. Note that TS measurements were performed for many types of discharges with I_p of 5–25 kA, and similar profiles (i.e., the hollow T_e and the peaked n_e profiles) were found in all cases. These results are discussed in Chapter 6. In addition, there is a trend that higher T_e is obtained in the discharges with higher plasma current.

Coaxial double-pass TS measurements for similar LHW-driven plasmas (I_p = 10 kA) were performed [48]. Although LHW accelerates electrons along field lines, and the energy transfer to the bulk electrons can be asymmetric, the high collisionality of bulk electrons would eliminate the temperature anisotropy. The double-pass TS signals (at R = 366 mm) obtained from five reproducible discharges and the result of the Maxwellian fits for each pass are shown in Fig. 4.10. Two peaks corresponding to the forward and the backward passes are clearly shown in the wavelength channels close to the YAG wavelength. Although the stray light in the backward pass is significant, the signals are fitted well to a Maxwellian distribution function. The obtained temperatures are 15.3 $\pm$ 2.2 eV and 15.4 $\pm$ 1.8 eV, and the densities ($\sim 7.0 \times 10^{17}$ m^{-3}) agree within 10 % errors. Thus, it can be said that the bulk pressure does not have a significant anisotropy at the plasma central region.

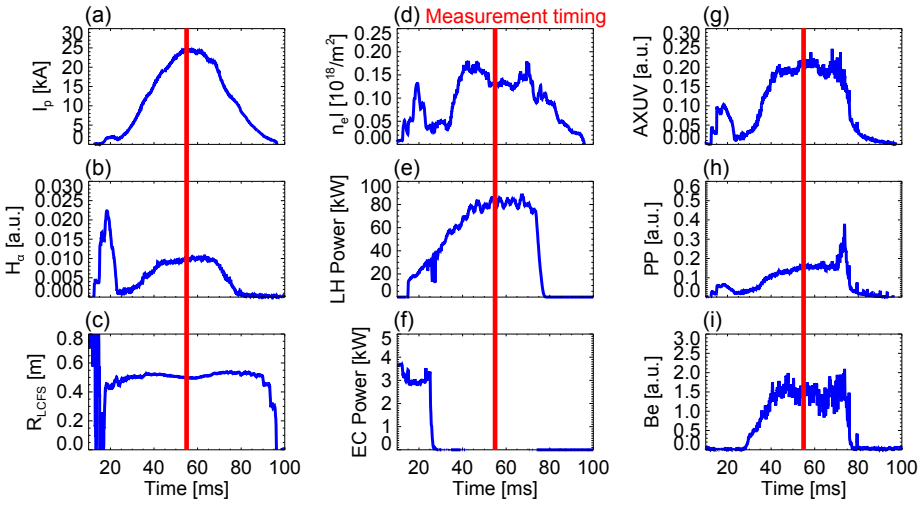

Fig. 4.4: Waveforms of a discharge sustained by the LHW from the outboard-launch CCC antenna: plasma current (a), signal of H_α (b), outboard radius of the LCFS at the midplane (c), line-integrated density at the midplane (d), LHW power (e), ECW power (f), signal of AXUV (g), and signals of the SBDs with thin films of polypropylene (h) and beryllium (i). Vertical red lines indicate the TS measurement timings.

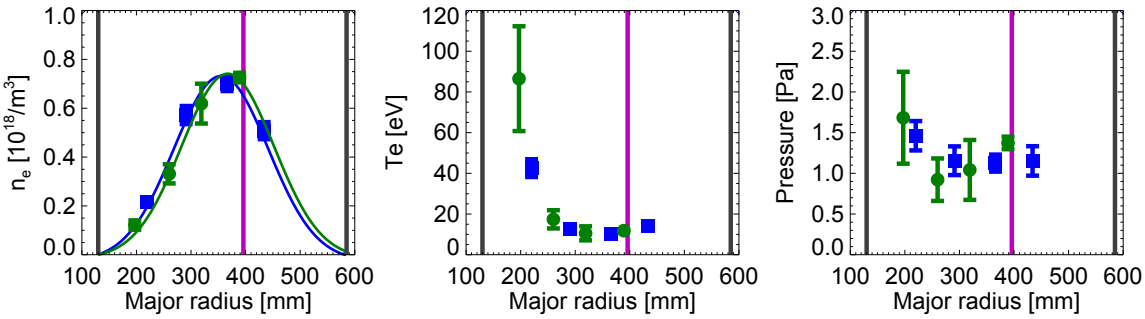

Fig. 4.5: Profiles of n_e (left), T_e (center), and p_e (right). Color of the symbols shows the set of spatial points in a simultaneous measurement. Black lines represent the inboard and outboard limiter positions and purple lines show the magnetic axes obtained from the EFIT code. The solid curve in the left shows the Gaussian fit.

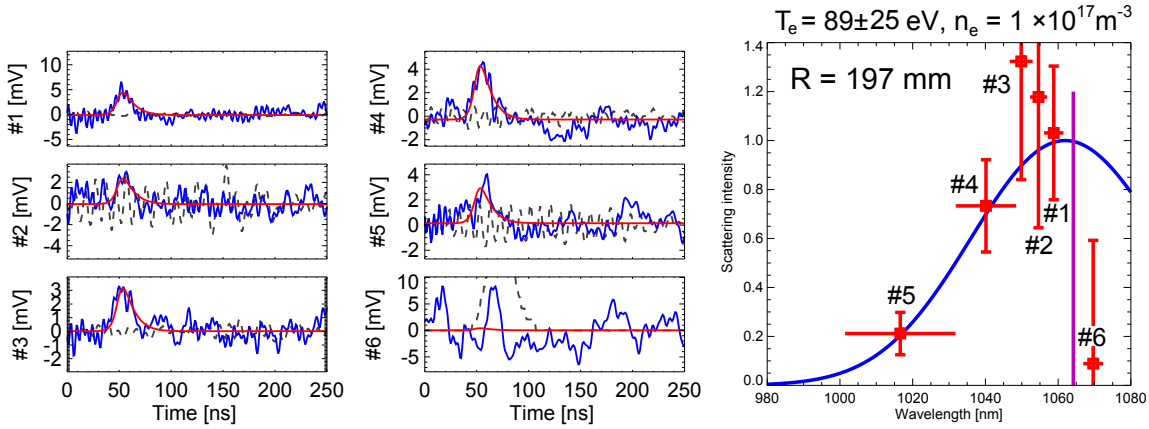

Fig. 4.6: Background-subtracted signals (blue curves), the fits (red curves), and the backgrounds (black dotted curves) are shown in the left six figures. Result of fitting into a Maxwellian distribution function is shown in the right figure. Here measurement position is R = 197 mm.

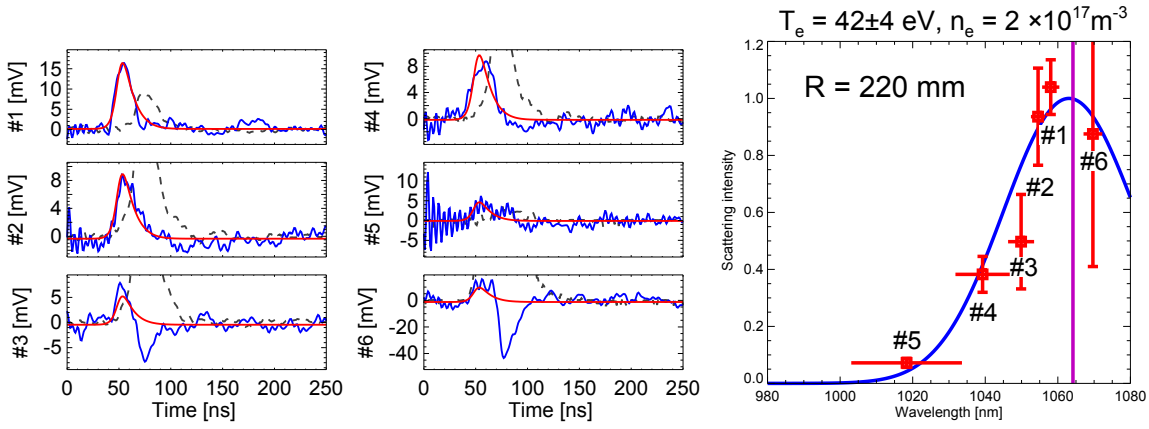

Fig. 4.7: Background-subtracted signals (blue curves), the fits (red curves), and the backgrounds (black dotted curves) are shown in the left six figures. Result of fitting into a Maxwellian distribution function is shown in the right figure. Here measurement position is R = 220 mm.

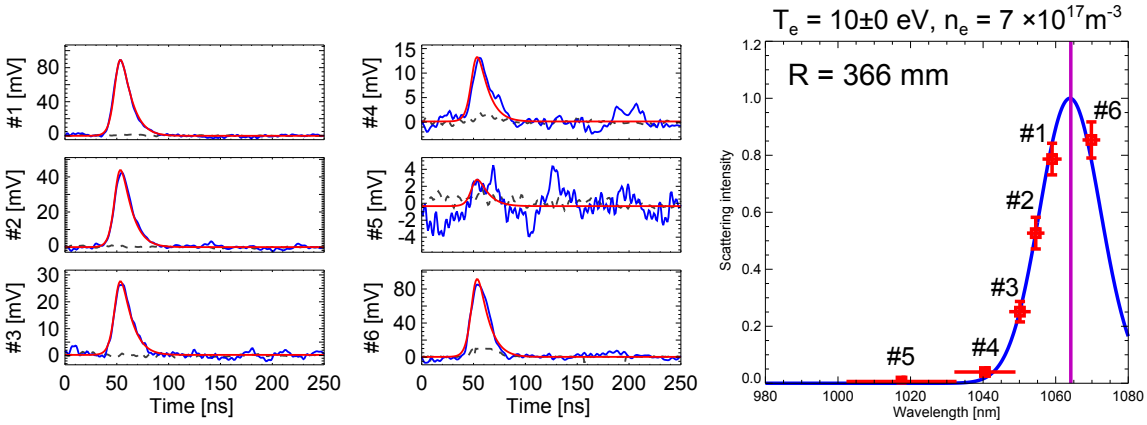

Fig. 4.8: Background-subtracted signals (blue curves), the fits (red curves), and the backgrounds (black dotted curves) are shown in the left six figures. Result of fitting into a Maxwellian distribution function is shown in the right figure. Here measurement position is R = 366 mm.

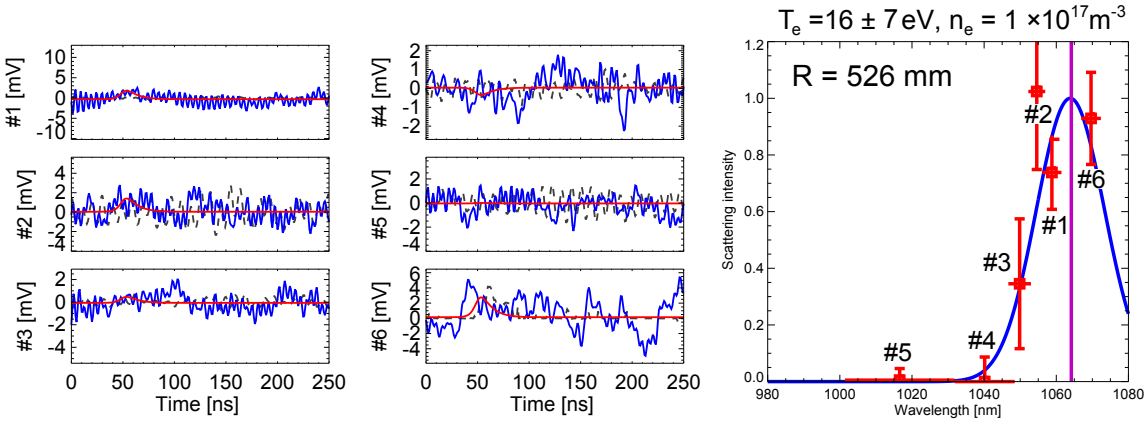

Fig. 4.9: Background-subtracted signals (blue curves), the fits (red curves), and the backgrounds (black dotted curves) are shown in the left six figures. Result of fitting into a Maxwellian distribution function is shown in the right figure. Here measurement position is R = 526 mm.

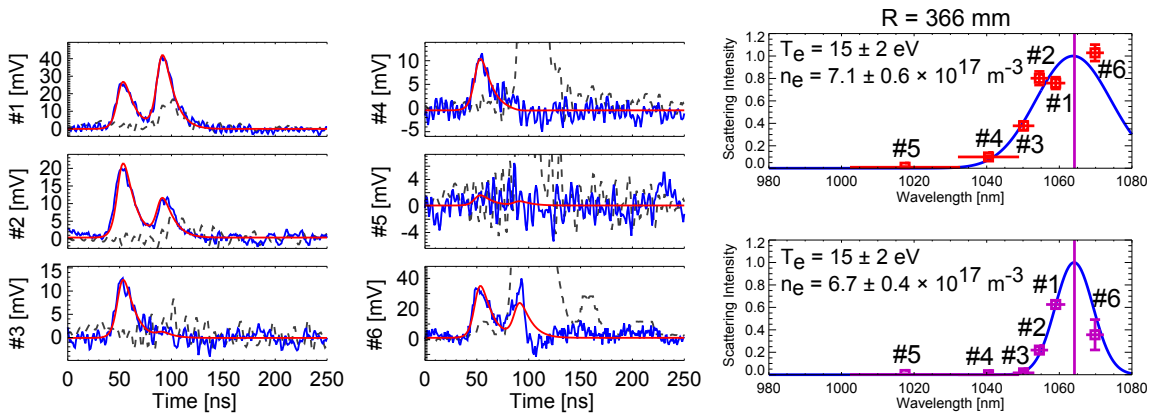

Fig. 4.10: Background-subtracted signals (blue curves), the fits (red curves), and the backgrounds (black dotted curves) are shown in the left six figures. Result of fitting into a Maxwellian distribution function is shown in the right figure.

In order to clarify the measurable low density limit of the developed TS diagnostic system, TS measurements with the measurement position near the plasma center (R = 366 mm) were performed for 5 reproducible discharges with low density. Figure 4.11 shows TS signals obtained by averaging those from the 5 discharges and result of the fit to a Maxwell distribution function. Apparent TS signals can be seen, while the stray light seems to be small and the electron temperature and density are estimated to be 35 ± 9 eV and $(2.5 \pm 0.3) \times 10^{17}$ m^{-3}, respectively. Measurement results obtained from one discharge without the average are shown in Fig. 4.12. Although resultant SNRs are inferior to those obtained from the averaged TS signals, similar values are estimated. For $n_e < 2.0 \times 10^{17}$ m^{-3}, apparent TS signal could not be seen. Therefore, it is suggested that measurable density limit of the system is around 2×10^{17} m^{-3}.

Here, we compare our system with that in other devices in terms of the low density limit. The TS diagnostic system in MAST is known as a high-performance system among conventional systems. However, as reported in 2015 [20], MAST plasmas with $n_{e0} \sim 3.0 \times 10^{17}$ m^{-3} could not be measured without averaging TS signals due to the measurable limit. Therefore, our system is similar or superior to the system in MAST in the point of view of the SNR. Note that laser energy and $L\Omega$ in the detection system for TST-2 and MAST TS systems are similar. Also in other conventional systems, laser energy and $L\Omega$ seem to be the same level [80–82], and the significant enhancement of these parameters is not easy. In QUEST, TS measurement has been performed successfully by accumulating many TS signals using a stable long pulse discharge [37]. However, such accumulation cannot be applied for short and unstable discharges, and other techniques (e.g., multi-pass TS scheme) are necessary. In TST-2, T_e and n_e in the edge are very important but difficult to be measured, and thus efforts to improve the performance have to be continued.

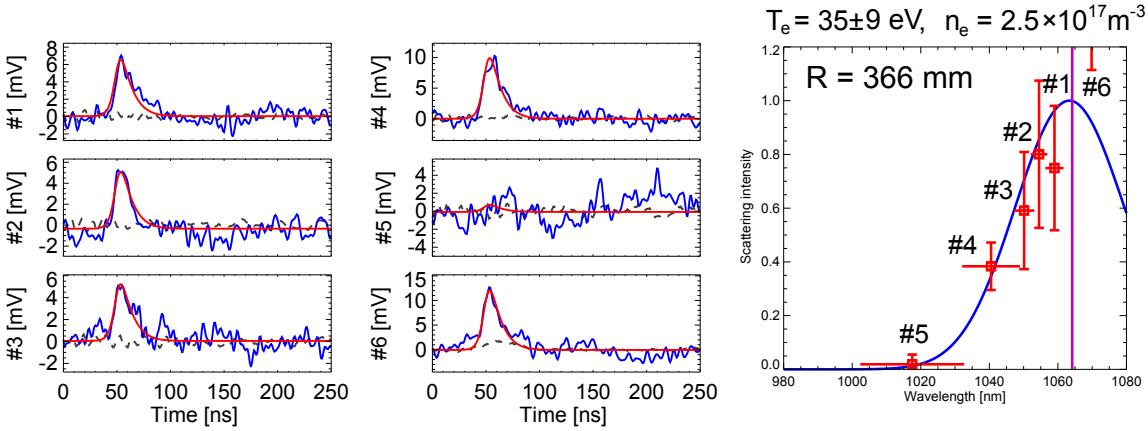

Fig. 4.11: Background-subtracted signals (blue curves), the fits (red curves), and the backgrounds (black dotted curves) are shown in the left six figures. Result of fitting into a Maxwellian distribution function is shown in the right figure.

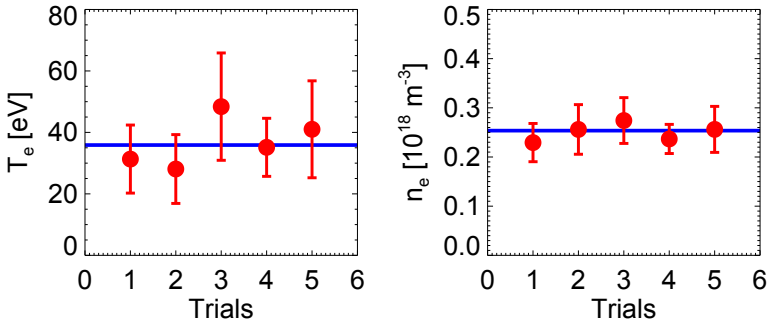

Fig. 4.12: Electron temperature (left) and density (right) near the plasma center (R = 366 mm) obtained for 5 plasmas (red dots). Each blue line represents result obtained from the TS signals averaged over those for the 5 discharges.

4.3 Non-inductively driven plasmas by LHW using top-launch CCC antenna

Top-launch CCC antenna was designed, fabricated, and installed on TST-2 [83]. Structure of the antenna is similar to that of the outboard-launch antenna, which shows sharp wavenumber spectrum for the excited waves and a low reflectivity at the input port. The behavior of propagation and absorption of waves in the TST-2 plasmas was simulated using the ray-tracing code GENRAY. In the simulation, target plasmas are assumed to have the same n_e and T_e profiles as those in the outboard-launch experiments. The simulation result shows that significant up-shift of the parallel refractive index occurs in the first pass and then the waves are significantly absorbed at the plasma core region without reaching the LCFS and without the succeeding reflection (or transmission) there. In such a situation (with strong absorption), bulk electron temperature T_e at the core can be much higher than that obtained in the scheme using the outboard-launch antenna. In order to demonstrate the performance of top-launch antenna, preliminary experiments were performed, where plasma current is started-up and sustained by the top-launch antenna alone. Waveforms of a discharge are shown in Fig. 4.13. Here, ECW power with a few kilowatts is injected throughout the discharge to prevent the electron density from reaching a density limit, where the plasma is disrupted (the details of the density limit and its suppression by ECW are described in Ref. [84]). In the preliminary experiments, current drive up to 12 kA was achieved [85], and coaxial double-pass TS measurements were performed for these plasmas. Contrary to the expectation, low T_e of 11 eV is estimated, which is similar to that obtained in the experiments using the outboard-launch antenna. Significant anisotropy at the core is not seen. In the peripheral region, however, due to the low density and strong stray light, the fitting seems to be too uncertain to evaluate the anisotropy. In order to improve the SNR, double-pass TS signals (two signals obtained in both paths) were analyzed assuming an isotropic T_e. Resultant profiles are shown in Fig. 4.14, and each shape is similar to that obtained in the experiments using the outboard-launch CCC antenna with similar current.

It is thought that the top-launch CCC antenna enables sufficient core absorption, higher plasma current, and central heating, but these are not observed in the preliminary experiments. This is probably because this antenna was designed by ray-tracing using GENRAY for plasmas generated by the outboard-launch antenna and such plasmas cannot be created by the top-launch antenna alone. Therefore, current ramp-up is expected by applying dual-

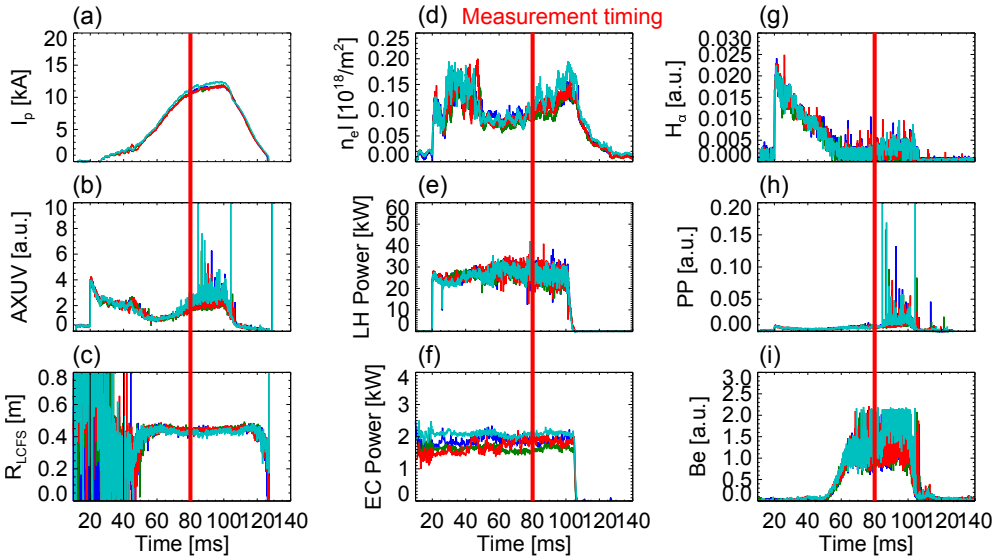

Fig. 4.13: Waveforms of discharges sustained by LHW from the top-launch CCC antenna: plasma currents (a), signals of AXUV (b), outboard radii of the LCFS at the midplane (c), line-integrated density at the midplane (d), LHW powers (e), ECW powers (f), signals of H_α (g), and signals of the SBDs with thin films of polypropylene (h) and beryllium (i). Vertical red lines represent the TS measurement timings. Waveforms of several discharges are plotted to show the reproducibility of discharges used for the signal accumulation.

antenna scheme.

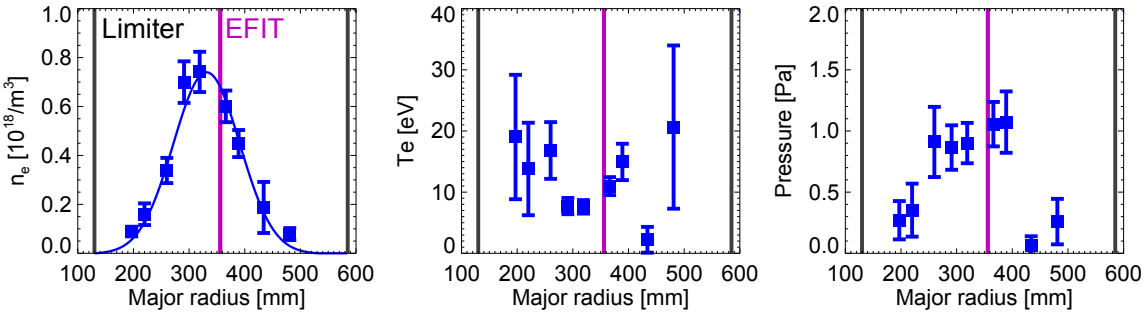

Fig. 4.14: Profiles of n_e (left), T_e (center), and p_e (right). Black lines represent limiters on both sides and purple lines show the magnetic axes obtained from the EFIT code. The solid curve in the left shows the Gaussian fit.

4.4 Hard X-ray measurements for LHW-driven plasmas

HXR profile measurements were performed for LHW-driven plasmas. Here, the target plasmas were generated to test the dual launch scheme where both the top and outboard launch antennas are used to excite LHWs. Note that the LHW power for the top-launch antenna is set to be quite low (a few kilowatts) in this case. Figure 4.15 shows the waveforms of typical discharges. In the HXR measurements, a 3.5 mm diameter pinhole was used. Then 7 reproducible discharges were analyzed for the profile measurement, and the other 7 discharges were used for the background measurement using the shielding without a pinhole. Front part of the diagnostic system was moved by the linear stage to prevent partial blocking of the fields of view by the viewing port tube. Figure 4.16 shows the HXR

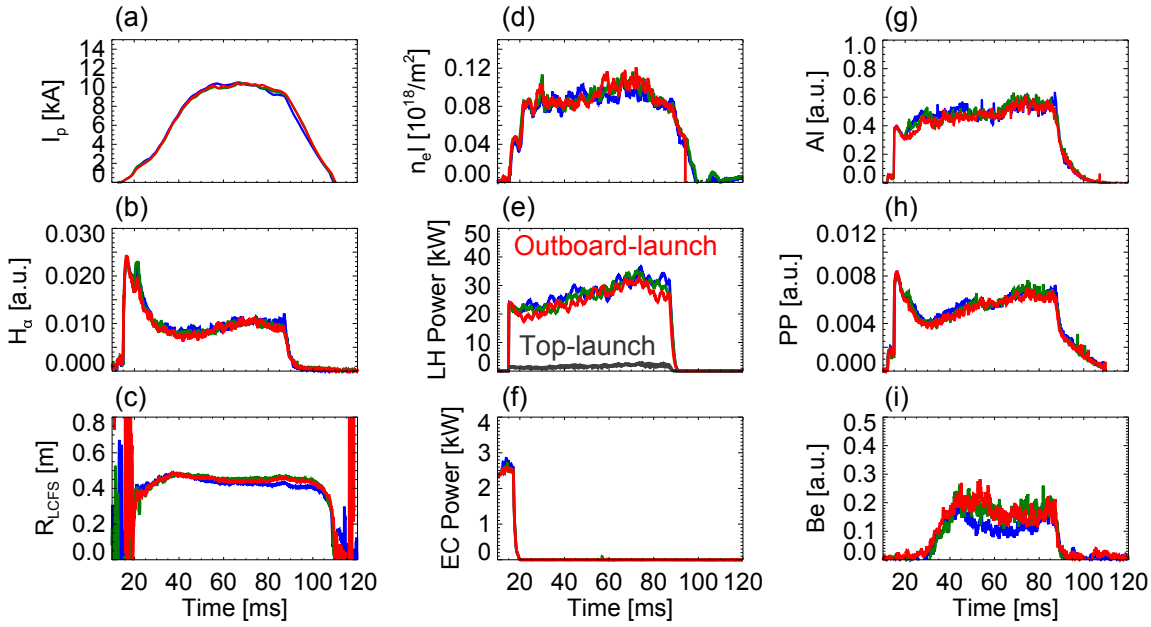

Fig. 4.15: Waveforms of discharges sustained by LHW from the outboard/top-launch CCC antennas: plasma currents (a), signals of H_α (b), outboard radii of the LCFS at the midplane (c), line-integrated densities at the midplane (d), LHW powers (e), ECW powers (f), and signals of the SBDs with thin films of aluminum (g), polypropylene (h), and beryllium (i).

signals. Background photons are not negligible and pile-up occurs in the second half of the discharge. The time evolution of energy spectra including the background measurements for chord #3 (R_{tan} = 360 mm) is shown in Fig. 4.17. The background is small and large distortion of the spectrum is not seen for 30–45 ms, while background photons with the peak around 60 keV are shown in the second half (45 ms –) and the spectra are distorted. Energy spectra for 7 chords for 30–45 ms are shown in Fig. 4.18. Effective T_e is estimated to be a few tens of keV for all the chords.

Figures 4.19 shows energy flux for 30–45 ms. The flux is defined as the energy divided by the solid angle (~ 0.024 sr), the area of the pinhole (9.6 mm^2), the time and the energy bin size used in the analysis (15 ms and 1 keV, respectively), having the unit of erg/cm^2/s/sr/eV. Here the effect of transmission spectrum of the window is corrected. It is indicated that the flux decreases with R_{tan}.

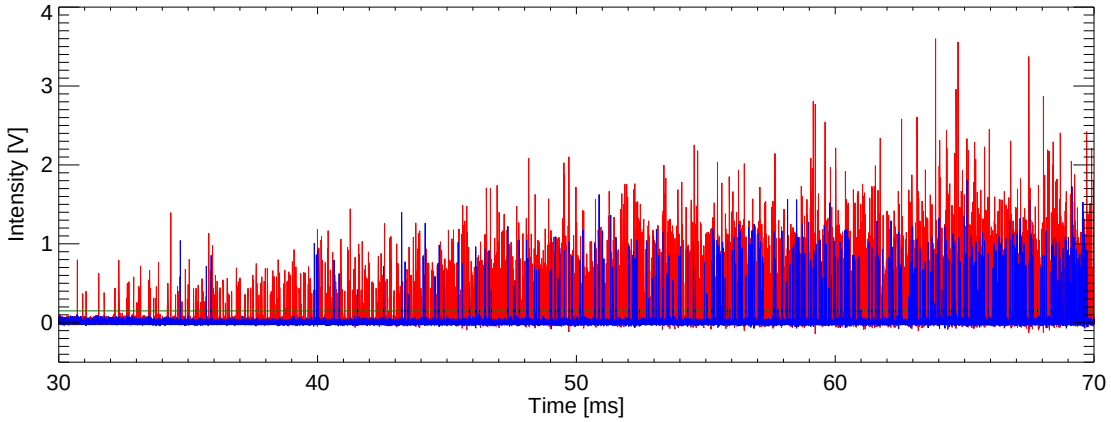

Fig. 4.16: HXR signals detected in the two setups with lead shielding including the 3.5 mm pinhole (red) and lead shielding without the pinhole (blue). Green horizontal line shows threshold (~ 10 keV) in the photon detection.

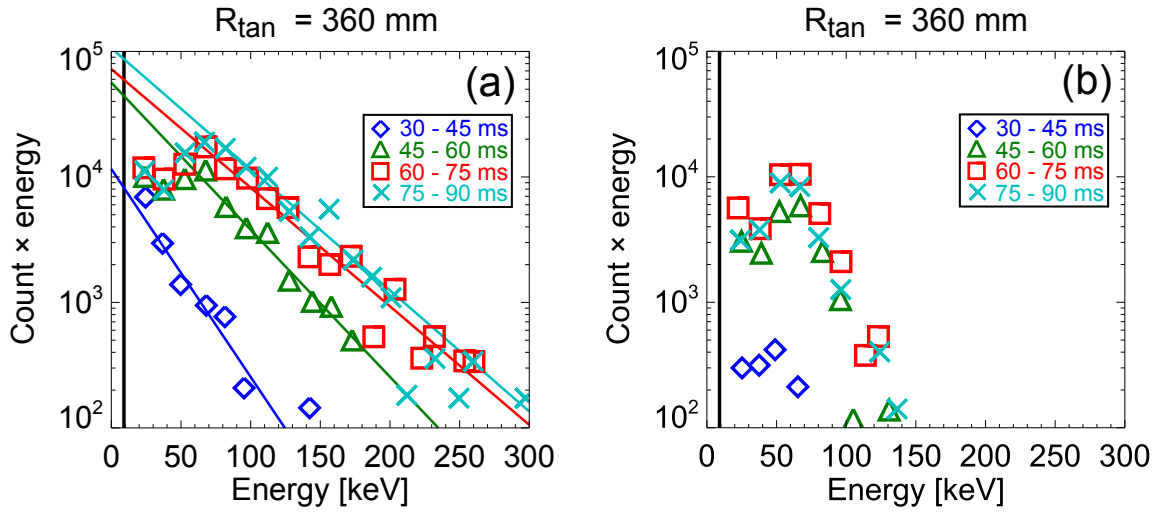

Fig. 4.17: Time evolution of the energy spectrum for chord #3 (R_{tan} = 360 mm) in the setups with pinhole (a) and without the pinhole (b). Each colored line represents the fitting and vertical black line represents the threshold in photon detection.

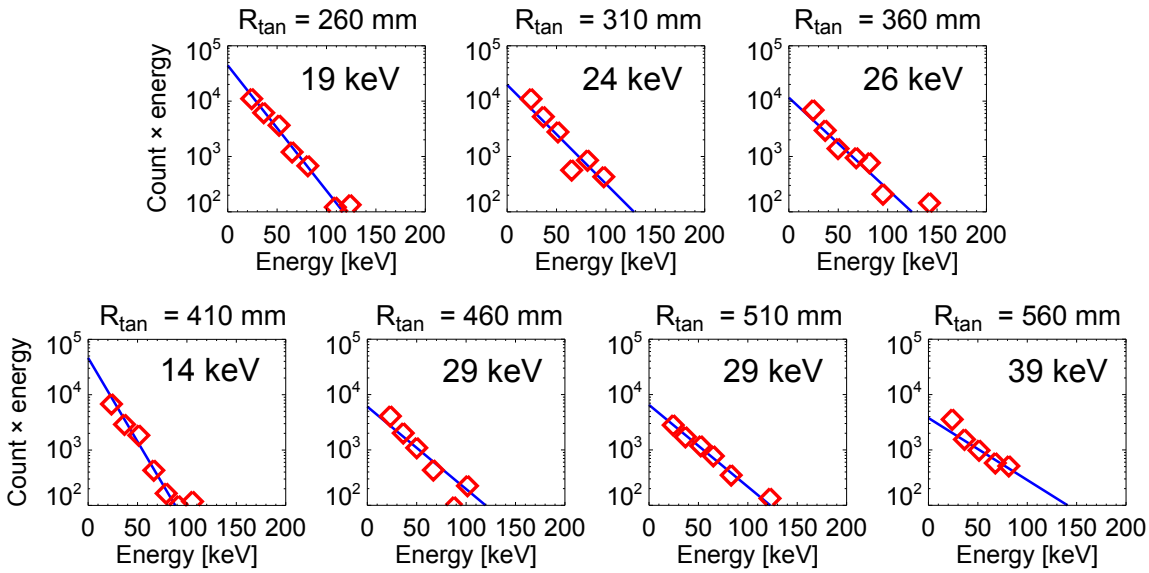

Fig. 4.18: Energy spectra for 7 chords for 30–45 ms (red squares). Each blue line shows the linear fit.

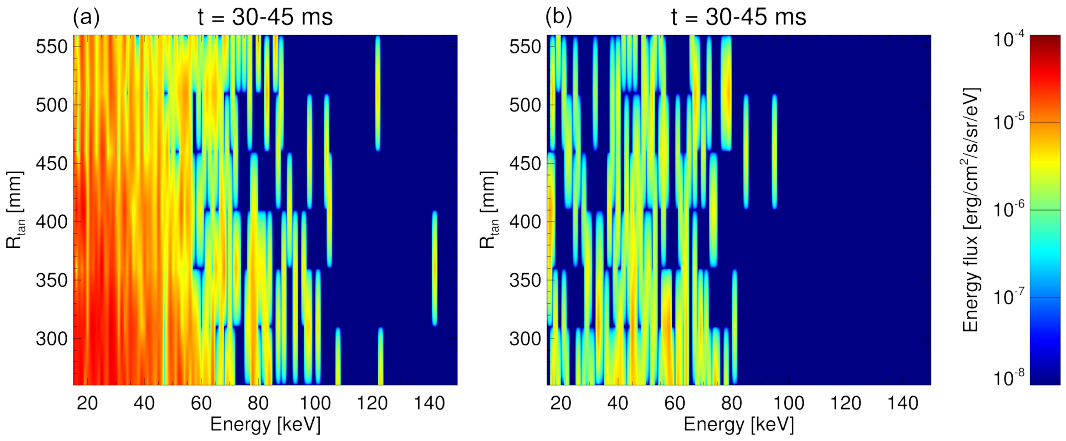

Fig. 4.19: Profiles of energy flux for 30–45 ms with pinhole (a) and without pinhole (b).

Time evolution of the effective T_e was obtained for three types of plasmas with the maximum current of about 8, 10, and 20 kA. The measurements were performed with one viewing chord (R_{tan} = 360 mm) and the energy spectra are shown in Fig. 4.20. It can be seen that count of HXR increases with time (and current), and higher energy photons tend to appear with time for all the plasmas. Linear part of each spectrum is fitted to a linear function and the slope is regarded as the effective T_e. The comparison between the effective T_e and the current is shown in Fig. 4.21, and a tendency, where effective temperature of fast electrons increases with plasma current, is shown.

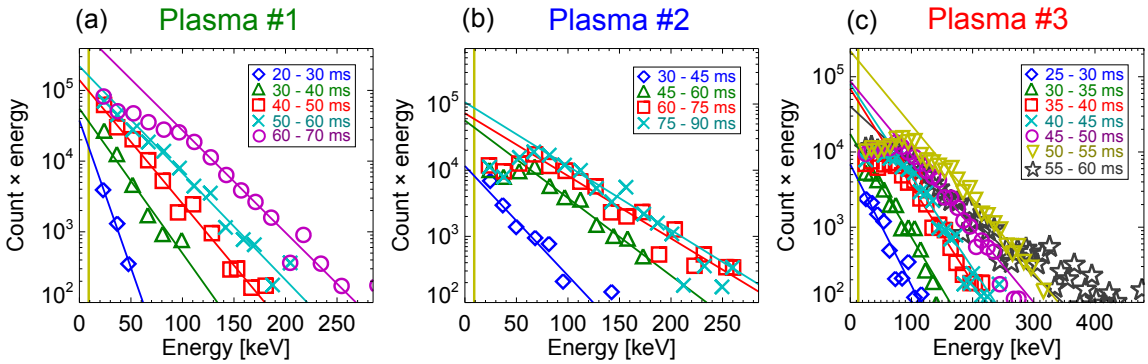

Fig. 4.20: Time evolution of energy spectra for plasmas with the maximum current of about 8 kA (a), 10 kA (b), and 20 kA (c).

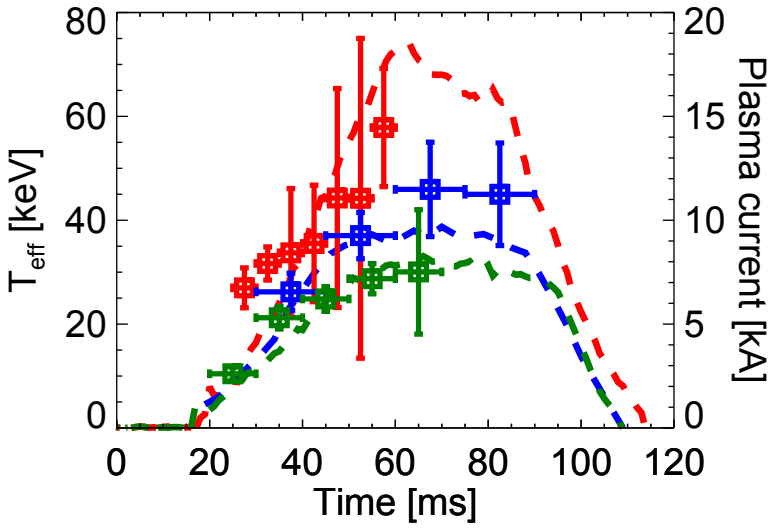

Fig. 4.21: Time evolution of effective temperature of fast electrons (squares) and plasma current (dashed curves) for three discharges indicated by different colors.

The central electron pressures for the bulk part of the velocity distribution function, which are obtained from the TS measurements, were around 1 Pa for various plasmas with plasma current of 5–25 kA. On the other hand, the total pressures for species including ion and tail part of electron, calculated from magnetic measurements and the EFIT code, 20–200 Pa at the plasma center. Since the typical ion temperature T_i is several eV according to spectroscopy [86], ion pressure should be lower than the electron pressures. Remaining fast electron temperature estimated by the HXR measurements are in the range of 10–100 keV, and thus it is suggested that minor fast electrons generated by LHWs are dominant in the equilibrium of the LHW-driven TST-2 plasmas [87].

Chapter 5

Thomson scattering measurements on QUEST

5.1 Experimental setup

In QUEST, a spherical tokamak device in Kyushu university, non-inductive plasma experiments have been performed to demonstrate a long pulse discharge by using ECW and to study steady state plasmas [21–24]. A photograph of QUEST is shown in Fig. 5.1. The nominal major radius and minor radius of QUEST are 0.65 m and 0.4 m, respectively, and TF coils and PF coils are equipped similarly to the arrangement of TST-2. Up to 0.25 T toroidal magnetic field at the plasma center is available. Four frequencies in the ECW range: 2.45, 8.2, 8.56, and 28 GHz are available. The 8.2 GHz ECW (up to 200 kW) and the 28 GHz ECW (up to 600 kW) are normally used for the plasma heating and the current drive. In addition, Ohmically heated plasmas are available by the use of the CS. In cooperative research with university of Hyogo, compact torus (CT) injection experiments have been performed aiming at efficient central fueling. The following two magnetic configurations are mainly studied: (1) limiter configuration, where plasmas are limited by the inboard limiter located at the R = 230.5 mm, and (2) inboard poroidal null (IPN) configuration, where an X point with null poloidal magnetic field is formed at the inboard side and high poloidal beta β_{p} is obtained.

A TS diagnostic system similar to that in TST-2 has been developed in QUEST [89]. Schematic of the system is shown in Fig. 5.2. We use a YAG laser with a repetition rate of 10 Hz, an energy of 1.65 J, and a pulse width of 6–8 ns. The nominal measurement range is from R = 350 mm to R = 1100 mm, and the scattering angle is 165–170°. Solid angle is 0.03–0.07 sr, which is smaller than that in the TST-2 TS system, while scattering length is longer (18–53 mm), resulting in a higher collection efficiency of TS light.

TS measurements for plasmas with various configurations and the CT injection have been performed [39]. Simultaneous TS measurements with 6 spatial points were performed for non-inductively sustained plasmas with IPN configuration. Then a hollow temperature profile and a peaked density profile were obtained.

In this study, a movable fiber array holder, which enables us to extend available spatial points, was developed to obtain more detailed profiles. Figure 5.3 shows a schematic diagram of the holder. Using the holder, TS measurements with 12 spatial points were performed for 8.2 GHz ECW-driven plasmas with limiter or IPN configuration. Moreover, a plasma current of 70 kA was sustained by 300 kW/28GHz ECW alone, and then the profiles were measured by the TS diagnostics. The current is more than twice higher than that of

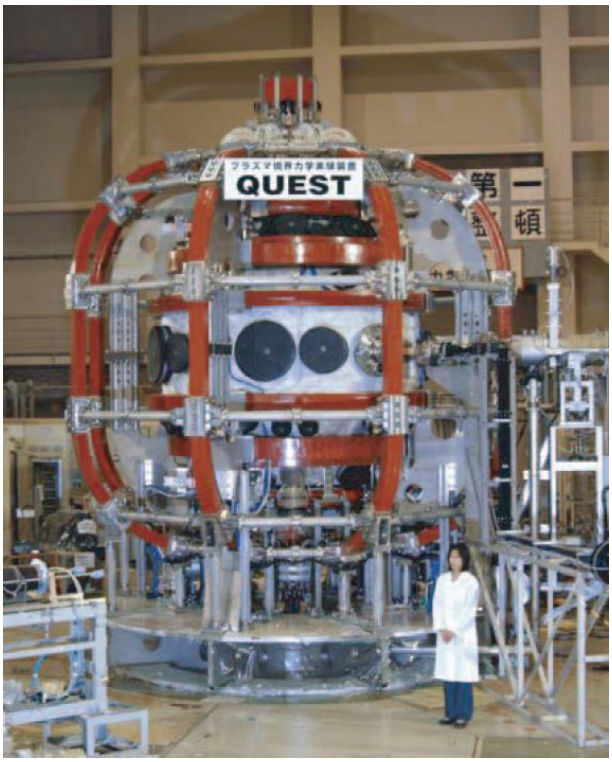

Fig. 5.1: Photograph of the vacuum vessel and TF and PF coils of QUEST [21].

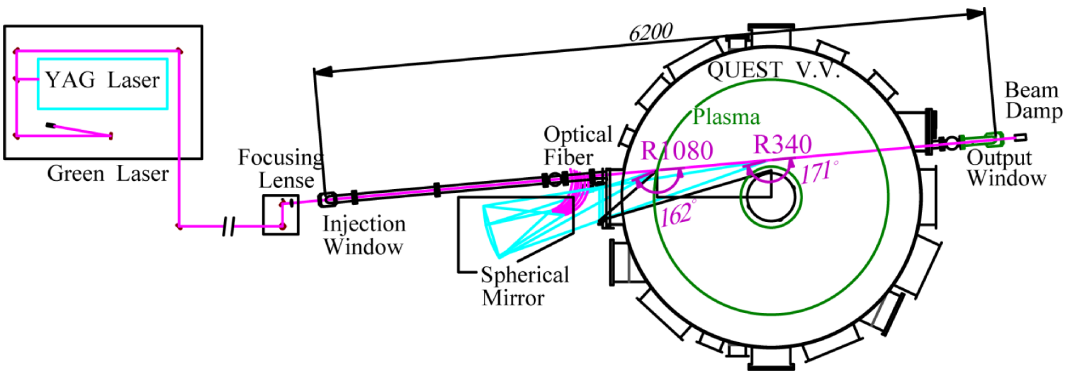

Fig. 5.2: Arrangement of the QUEST device and the TS system [89].

plasmas measured by the TS diagnostics in the past, and similar to that reported in MAST (73 kA) [20]. In MAST, after gas puffing, T_es obtained at the plasma center were 60–80 eV and peaks of up to 140 eV were found near an electron cyclotron resonance (ECR) radius. The n_e profiles were relatively flat with central values within 0.8–1.2 $\times 10^{18}$ m^{-3}. Before the gas puffing, central T_e of 210 eV and central n_e of 3 $\times 10^{17}$ m^{-3} were obtained by averaging TS signals. The difference of profiles between QUEST and MAST were investigated in the present experiments.

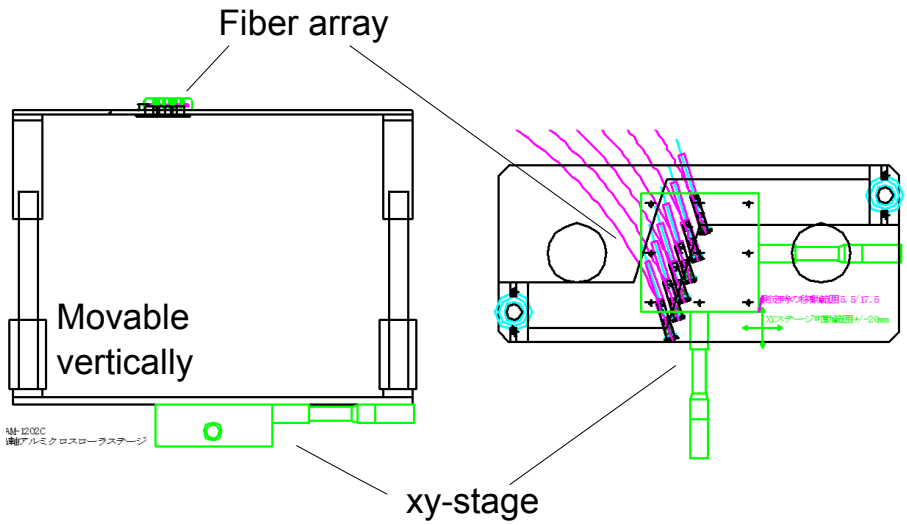

Fig. 5.3: Side view (left) and top view (right) of a fiber holder, which is movable in vertical and horizontal planes.

The plasma response against the CT injection is the order of microseconds. However, the TS measurements timing was not controlled and the time difference between the injection and the measurement could varies by ±50 ms. In order to solve the problem, a synchronization circuit was developed to control laser firing timing with the accuracy of less than 1 μs to the QUEST discharge sequence and the CT injection [40]. Figure 5.4 shows schematic diagram of the synchronization system. Detecting trigger signal from the QUEST sequencer, the synchronization circuit resets 10 Hz laser excitation lamp flashing with a given delay time. The CT injection timing is synchronized with the laser firing. Note that actual timing of the laser firing can be confirmed by using a photodiode located behind the laser path.

The following diagnostics were used to find out characteristics of plasmas. Photon emission with a wide energy range is measured by an AXUV photodiode monitor, and line emission of H_α and OII are measured by a spectrometer. Line-integrated density is measured by an interferometer, which is also used for n_e calibration of the TS measurement.

5.2 Non-inductive plasmas driven by 8.2 GHz ECW

TS measurements were performed for plasmas with limiter configuration sustained by 70 kW/8.2 GHz ECW. Figure 5.5 shows waveforms of a typical discharge. The cyclic rapid increases of H_α signal shown after $t = 3.5$ s are due to gas puffing from the inboard side. Red vertical lines represent the TS measurement timings. Since discharges in QUEST are

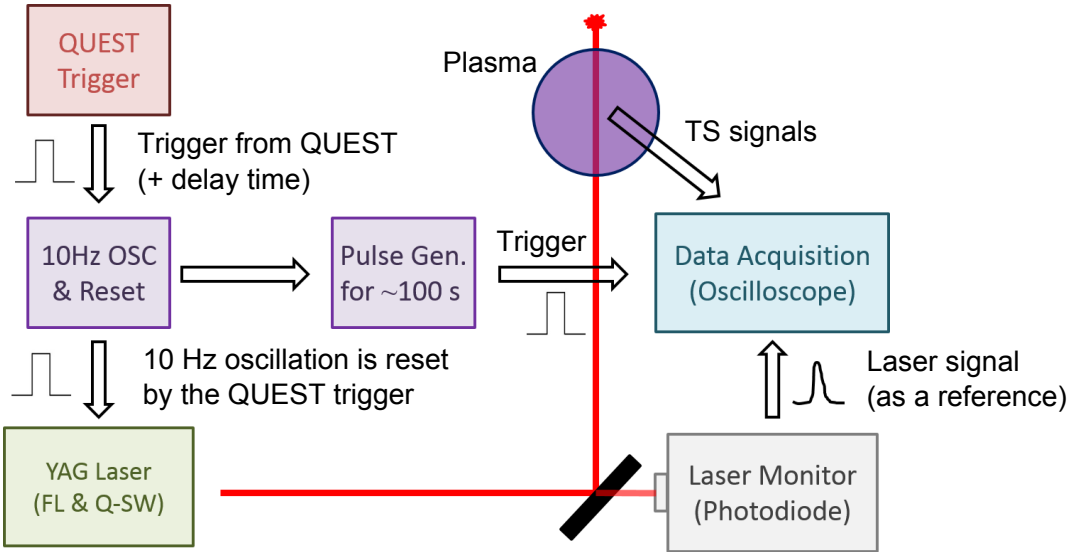

Fig. 5.4: Schematic diagram of synchronization between the QUEST operation system and the TS measurement system. Timing of the laser firing is controlled by a trigger signal in the operation [40].

much longer than those in TST-2, time evolution of electron temperatures and densities can be obtained with a sampling frequency of 10 Hz. Multiple plasmas with high reproducibility were averaged to improve the SNR. Resultant profiles with 12 spatial points are shown in Fig. 5.6. In this case, the experiments had been performed before the synchronization circuit was developed, and the results have time uncertainty of ±50 ms. Corresponding to the rapid increase of OII, H_α, and AXUV signals at just after t = 1.5 s, n_es at the inboard side become much higher at t = 1.5–1.6 s. After that, a trapezoidal n_e profile is observed at t = 1.8–1.9 s, indicating formation of the closed flux surfaces. Relatively high T_e is found near the ECR radius $R \sim 310$ mm at that time. At t = 3.6–3.7 and t = 6.5–6.6 s, each profile shows peaked shape, and the central values for T_e, n_e, and p_e are about 80 eV, 3×10^{17} m^{-3}, and 3 Pa, respectively. As shown in Fig. 5.7, each core parameter is kept stable during 3–9 s. Note that the second harmonic resonance of the ECW (here at $R \sim 620$ mm) is generally useful for the plasma heating, and higher temperature at the core may be sustained by the second harmonic heating.

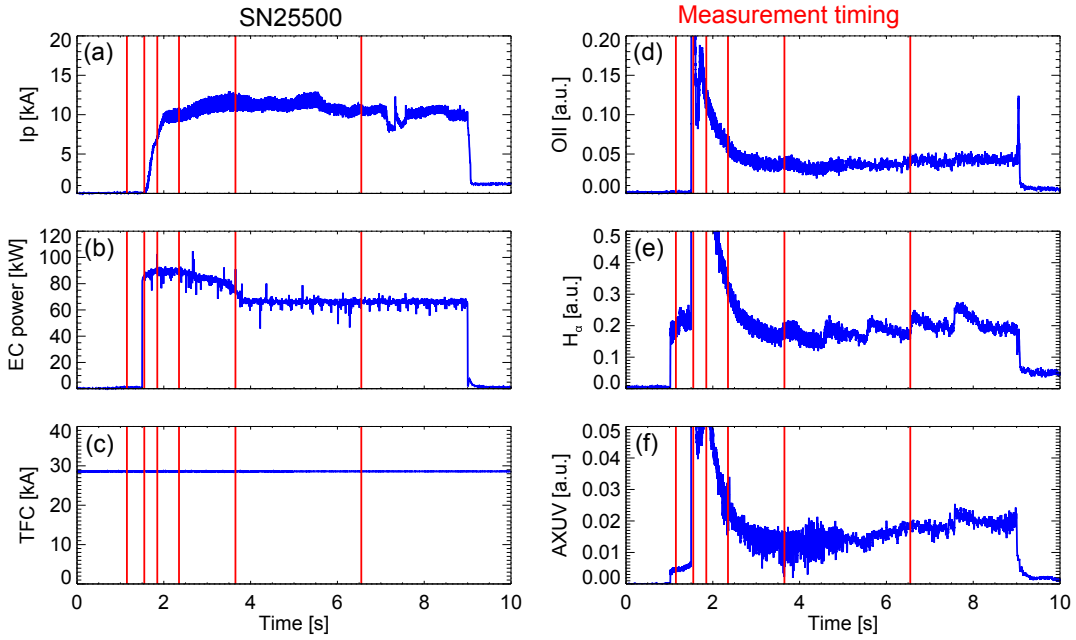

Fig. 5.5: Waveforms of a discharge with limiter configuration sustained by 8.2 GHz ECW: plasma current (a), ECW power (b), TF coil current (c), signals of OII (d) and H_α (e), and signal of AXUV (f). Vertical red lines represent the timings of measurements shown in Fig. 5.6.

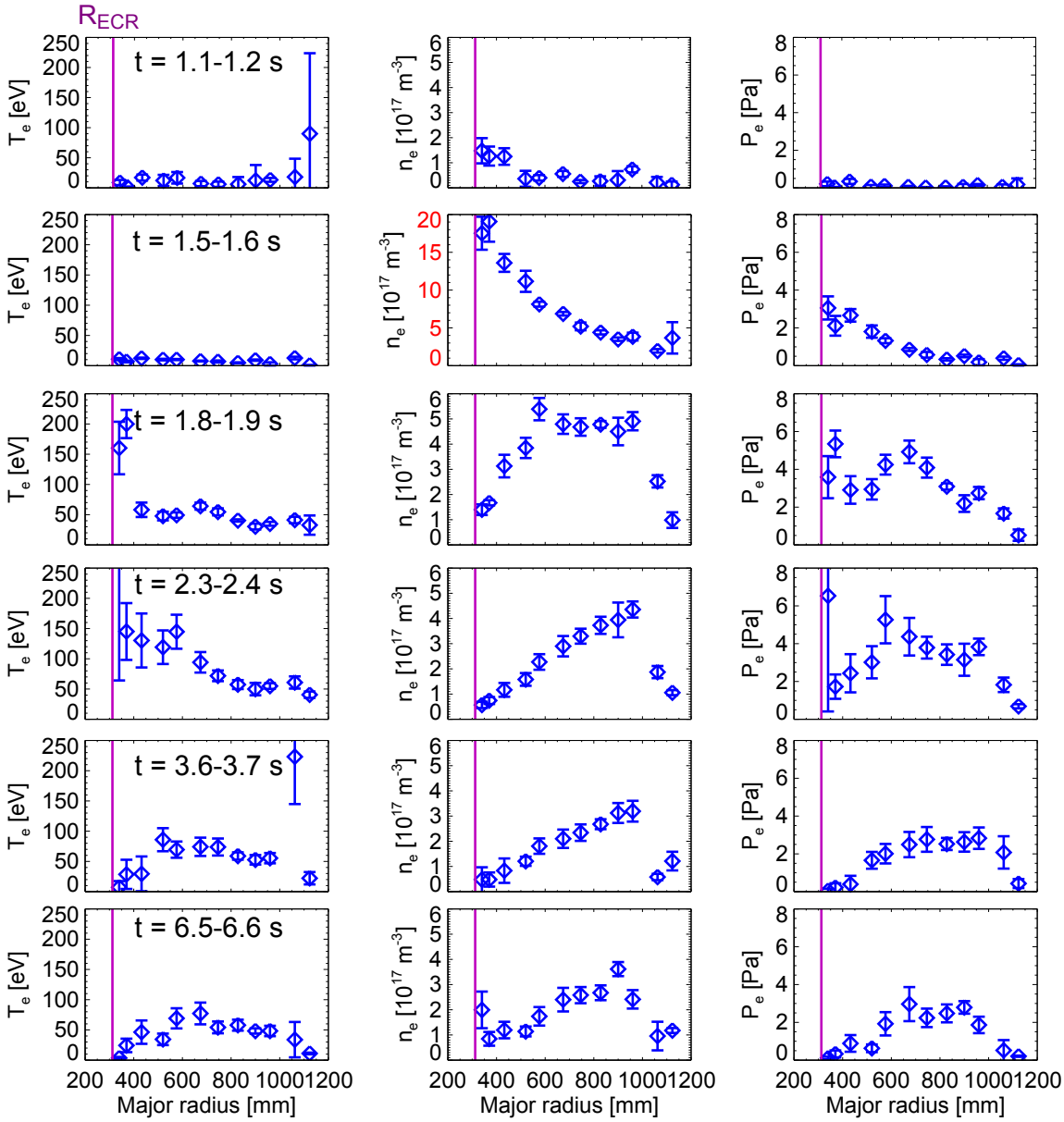

Fig. 5.6: Time evolution of profiles of the electron density (left), temperature (center), and pressure (right). Purple vertical lines show radii of electron cyclotron resonance. Note that the density scale at t = 1.5–1.6 s is different from the others.

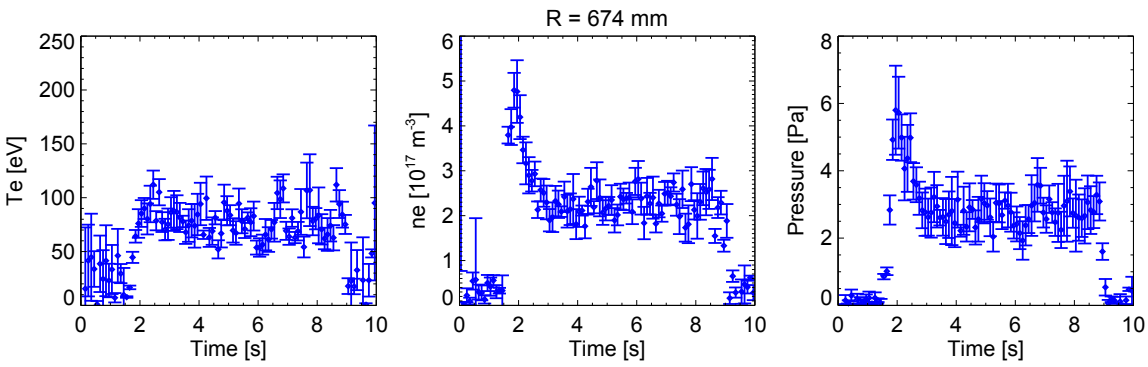

Fig. 5.7: Time evolution of T_e (left), n_e (center), and p_e (right) at R = 674 mm.

TS measurements were performed for plasmas with IPN configuration sustained by 60 kW/8.2 GHz ECW. Figure 5.8 shows waveforms of the discharges. Similarly to the previous TS measurements for plasmas with limiter configuration, reproducible plasmas were analyzed to obtain 12 spatial point profiles. Resultant profiles at t = 6.5–6.6 s are shown in Fig. 5.9, when the profiles seem to be quasi-stable. Unlike the profiles for limiter configuration, a T_e profile with higher temperature at the inboard side was found. This suggests that plasma heating occurs at the fundamental ECR layer rather than the second harmonic ECR layer. Such inboard-outboard asymmetric profile was also obtained in the n_e profile with high density near the ECR layer. Although these profiles cannot be expressed as a function of the magnetic surface, similar profiles were obtained in the previous experiments with IPN configuration [89]. Therefore, it is suggested that such a inboard-outboard asymmetric T_e profile is a characteristic one for the IPN configuration.

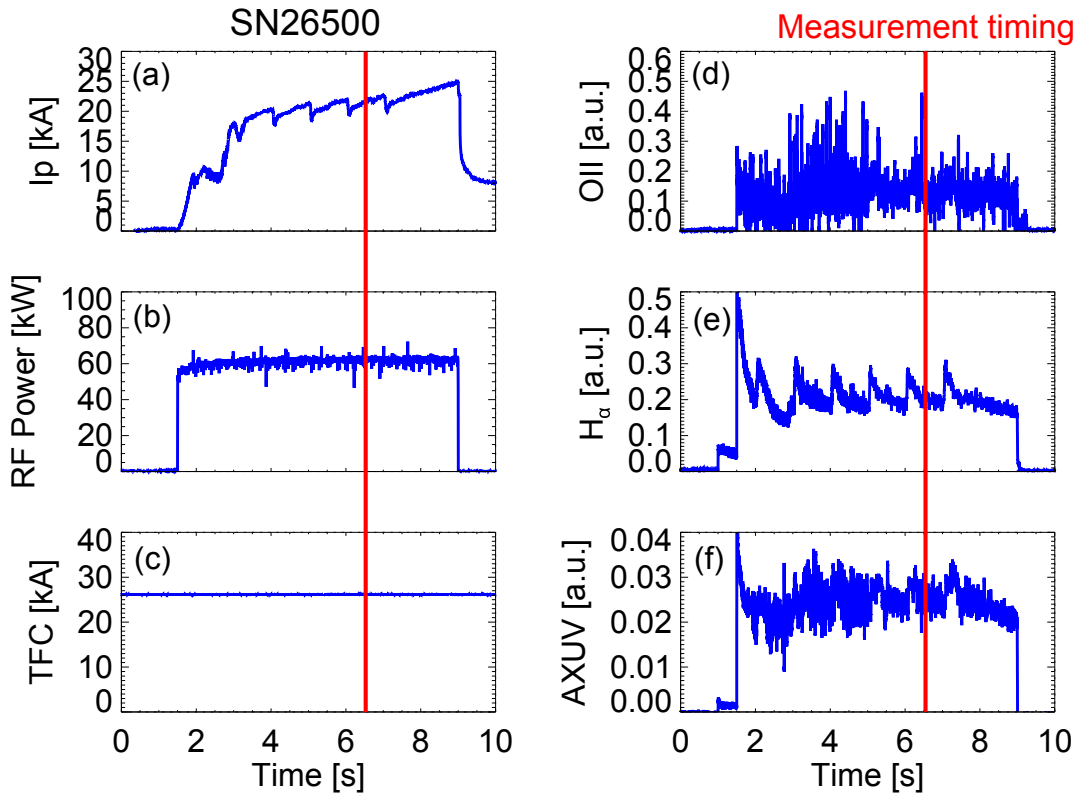

Fig. 5.8: Waveforms of discharge with the IPN configuration sustained by 8.2 GHz ECW: plasma current (a), ECW power (b), TF coil current (c), signals of OII (d) and H_α (e), and signal of AXUV (f). Vertical red lines represent the TS measurement timing corresponding to the profile in Fig. 5.9.

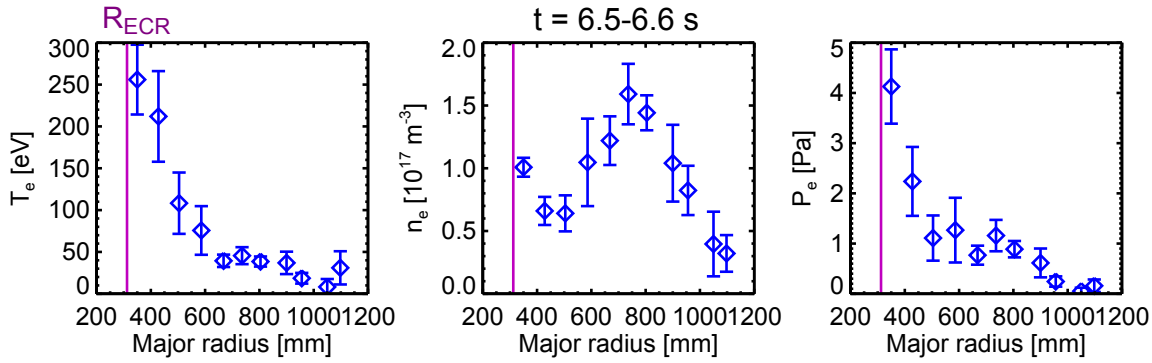

Fig. 5.9: Profiles of electron density (left), temperature (center), and pressure (right) in the discharges with IPN configuration. Purple vertical lines show radii of electron cyclotron resonance layer.

5.3 Non-inductive plasmas driven by 28 GHz ECW

TS measurements were performed for plasmas with the current of approximately 70 kA sustained by 8.2 GHz/28 GHz ECWs. Figure 5.10 shows waveforms of the discharge. 30 kW/8.2 GHz ECW is injected until t = 2 s, and 300 kW/28 GHz ECW injection continues during t = 1.8–2.8 s. Just after 8.2 GHz ECW is switched off at t = 2 s, the plasma current starts to increase with PF coil current, and the plasma current reached to approximately 70 kA. Profiles obtained at the three measurement timings (indicated by the vertical red lines in Fig. 5.10) are shown in Fig. 5.11. Since good reproducibility was not obtained in this experiments, only one discharge was analyzed, leading to poor SNRs at the peripheral region. At t = 2.0 s, the n_e profile has a peak value of about 0.2 $\times 10^{18}$ m^{-3} at $R \sim 470$ mm near the ECR radius for 8.2 GHz ECW. T_e at this point is around 100 eV. At t = 2.2 s without 8.2 GHz ECW, however, T_es inside the plasma decrease to less than 10 eV, while about twice higher n_e are obtained at $R \sim 470$ mm. Even though the plasma current reaches to more than 50 kA at t = 2.6 s, such low T_es are kept, but n_es become higher and the peak value is about 1.3 $\times 10^{18}$ m^{-3}. As a result, the bulk pressure p_e does not increase (but decrease), while the plasma current increases by more than five times from that of plasmas sustained by dual ECW. The value of n_e is similar to that obtained in MAST plasmas with 60 kW/28 GHz ECW and maximum current of 73 kA. On the other hand, more than ten times lower T_e at the core was found. It should be noted that the scheme in MAST is not an ordinary ECW heating and current drive scheme, but an EBW scheme using an O-X-B mode conversion technique.

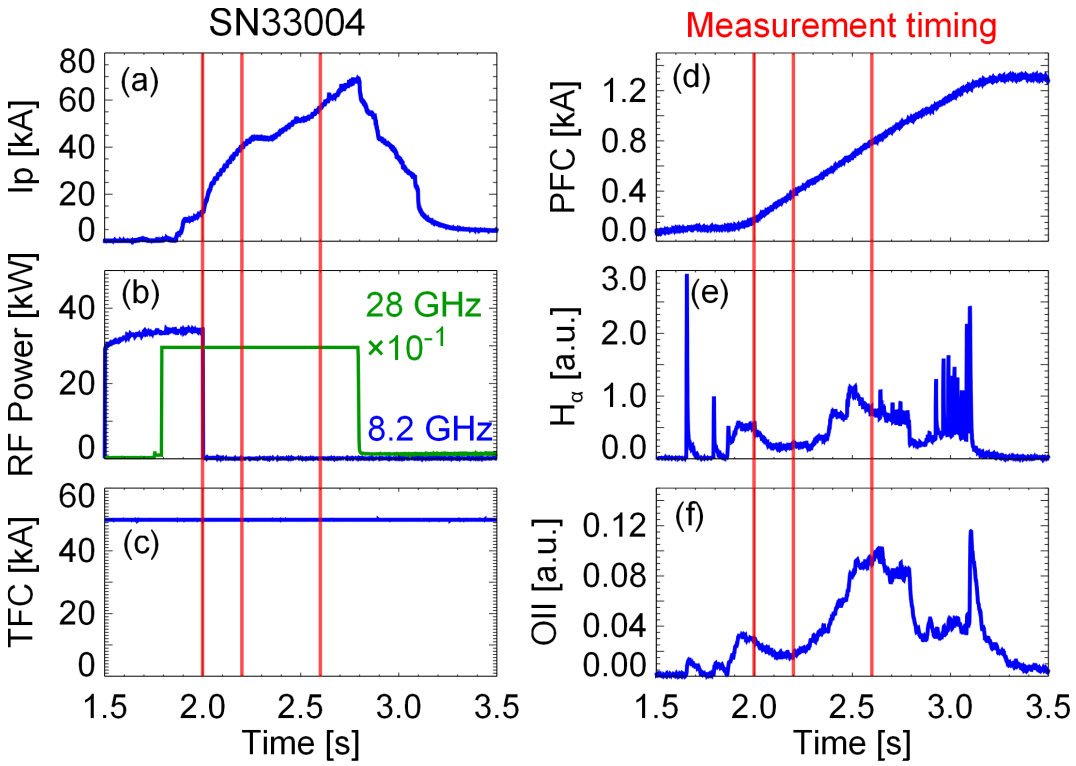

Fig. 5.10: Waveforms of a discharge sustained by 8.2 GHz/28 GHz ECWs: plasma current (a), 8.2 GHz ECW power (blue) and 28 GHz ECW power (green) (b), TF coil current (c), TF coil current (d), and signals of OII (e) and H_α (f). Note that waveform for 28 GHz ECW is just a input pulse to the ECW system and actual power is around 300 kW. Vertical red lines represent the TS measurement timings of the profiles shown in Fig. 5.11.

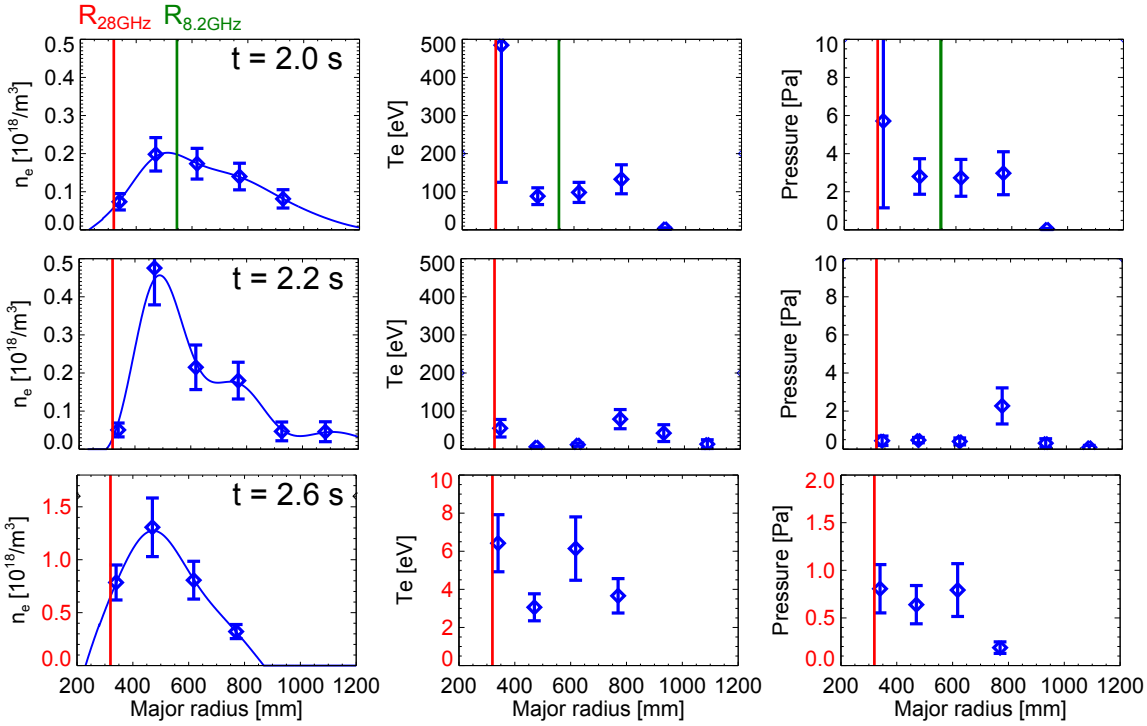

Fig. 5.11: Time evolution of profiles of the electron density (left), temperature (center), and pressure (right). Red and green vertical lines show radii of electron cyclotron resonance for 28 GHz and 8.2 GHz ECWs, respectively. Note that scale at t = 2.6 s is different from the others.

Contribution of bulk electrons to plasma equilibrium is considered here. The poloidal beta β_p is calculated by

$$\beta_p = \frac{\langle p \rangle}{B_\theta^2(a)/2\mu_0}, \tag{5.1}$$

where $\langle p \rangle$ is plasma pressure averaged over plasma volume and B_θ is magnetic field in the poloidal direction at the LCFS, which is approximated by

$$B_\theta = \frac{\mu_0 I_p}{2\pi a}. \tag{5.2}$$

In the IPN configuration, $\epsilon\beta_p = (a/R)\beta_p > 1.25$ is known [90]. Here, two types of β_ps are defined: β_p^{EQ}, which is calculated from plasma equilibrium, and β_p^{TS}, which is calculated from bulk electron pressure measured by TS diagnostics. In the previous study, $\epsilon\beta_p^{EQ}$ and $\epsilon\beta_p^{TS}$ were compared, and the resultant $\epsilon\beta_p^{EQ}$ was about 3, while $\epsilon\beta_p^{TS}$ was 0.015. In addition, HXR measurements gave us an effective temperature of about 40 keV for fast electrons. From these results, it is suggested that fast electrons generated by ECW power dominates the plasma equilibrium [39]. $\epsilon\beta_p^{TS}$s for the plasmas shown in this chapter were (1) $\epsilon\beta_p^{TS} \sim 0.1$ with limiter configuration using the 8.2 GHz ECW (Fig. 5.5), (2) $\epsilon\beta_p^{TS} \sim 0.01$ with the IPN configuration using the 8.2 GHz ECW (Fig. 5.8), and (3) $\epsilon\beta_p^{TS} \sim 0.001$ with limiter configuration using the 8.2 GHz and the 28 GHz ECWs (Fig. 5.10). According to the previous experiment with limiter configuration (I_p = 25 kA), equilibrium pressure was about 400 Pa and $\epsilon\beta_p^{EQ}$ was about 1.5. Therefore, these results obtained in the present experiments agree with the conclusion ($\epsilon\beta_p^{EQ} >> \epsilon\beta_p^{TS}$) obtained in the previous study.

5.4 Ohmically heated plasmas with compact torus injection

CT injection experiments were performed for two types of Ohmically heated plasmas with the plasma currents of 20 kA and 35 kA. First, CT injection experiments for plasmas with the I_p of about 20 kA are reported. In order to compare the effect and time evolution due to CT injection, three types of discharges are analyzed: (#1) a reference discharge without CT injection, (#2) a discharge with CT injection 2 ms before the TS measurement at t = 1.701 s, and (#3) a discharge with CT injection 70 μs before the TS measurement. Waveforms of the three discharges are shown in Fig. 5.12. It can be seen that good reproducibility is obtained. Here, ECW is injected for plasma ignition and current start-up to about 5 kA, and Ohmic heating starts at t = 1.3 s for current ramp-up to about 20 kA at the CT injection timing. H_α signal increases rapidly just after the CT injection, while OII signal starts to decrease slowly with a delay of about 2 ms. Result of the profile measurements is shown in Fig. 5.13. Although the errors in T_e are large due to the low density, similar n_e profiles can be seen at t = 1.601 s (before CT injection). At t = 1.701 s (just after CT injection), significant difference cannot be found between discharges #1 and #3. On the other hand, n_e values for discharge #2 increases to some extent compared with those for the other discharges. At t = 1.801 s, a few times higher densities than those for the reference discharge (#1) are obtained for the discharges with CT injection (#2 and #3). Thus, it is suggested that time response of n_e due to the CT injection is between 70 μs and 2 ms, and it is similar to

that (~ 3 ms) of H_α. With respect to the other parameters, T_es for discharges #2 and #3 are a few times lower than those for discharge #1 and p_es are the same level at t = 1.801 s.

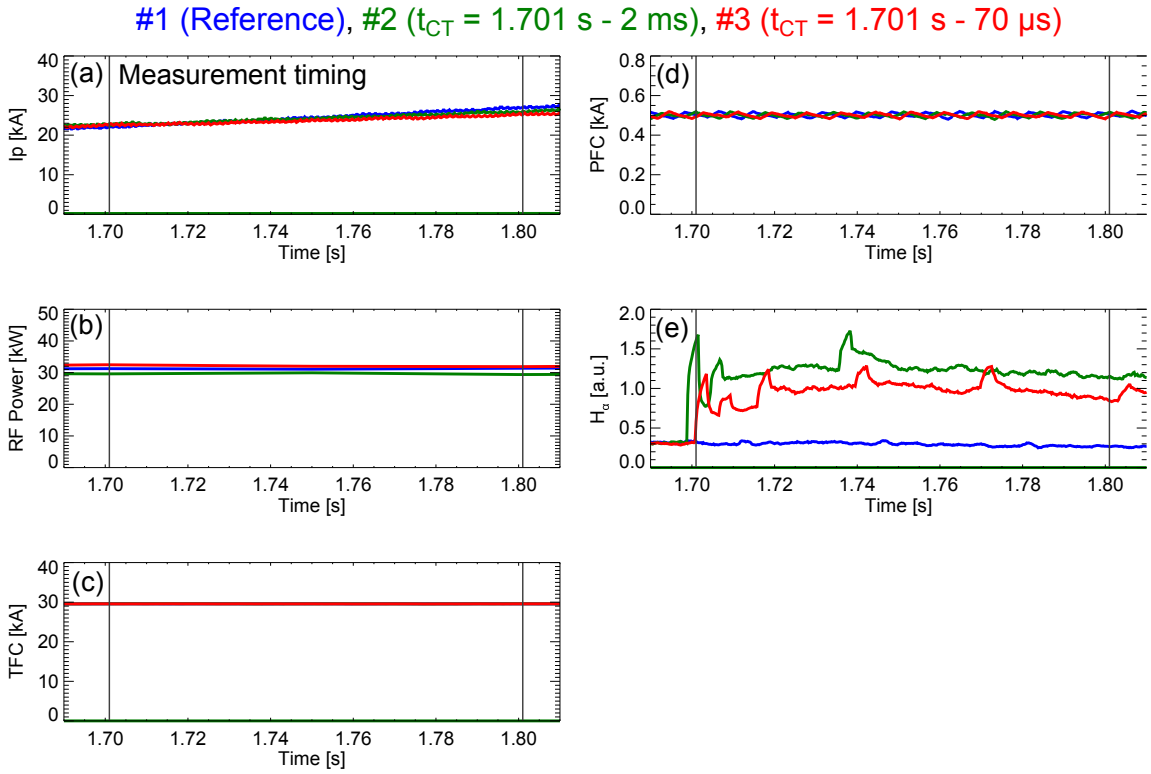

Fig. 5.12: Waveforms of three types of discharges: (#1) a reference discharge without CT injection (blue), (#2) a discharge with CT injection 2 ms before the TS measurement at t = 1.701 s (green), and (#3) a discharge with CT injection 70 μs before the TS measurement (red). The plotted curves are plasma current (a), 8.2 GHz ECW power (b), TF coil current (c), PF coil current (d), and signal of H_α (e). Black vertical lines represent the TS measurement timings.

Second, CT injection experiments for Ohmically heated plasmas with the current of about 35 kA were performed. Similarly to the previous experiments, ECW power is firstly injected to achieve plasma current of about 5 kA before Ohmic heating starts at t = 1.3 s. A reference plasma and a plasma with CT injection 2 ms before the TS measurement were analyzed. Figure 5.14 shows waveforms of the discharges. Comparing with the previous discharges, a larger increment in H_α signal can be seen. Decrease of the plasma current is found after a few milliseconds. With regard to OII emission, although the reproducibility is not good, the behavior after CT injection is completely different from that shown in the previous discharges. That is, OII emission increases just after CT injection during about 15 ms, and it decreases slowly after that. Obtained profiles are shown in Fig. 5.15. n_e profiles at t = 1.601 show more than twice higher peak value than that in the previous experiments. The peak position is also different and located at more outer side. T_es at the core region are several electron volts. Corresponding to the rapid change of the H_α signal just after the CT injection, a few times higher n_e profile is obtained at t = 1.701 s. At that time, T_es at the core region does not change so much, resulting in increments of p_es by a few times. At t

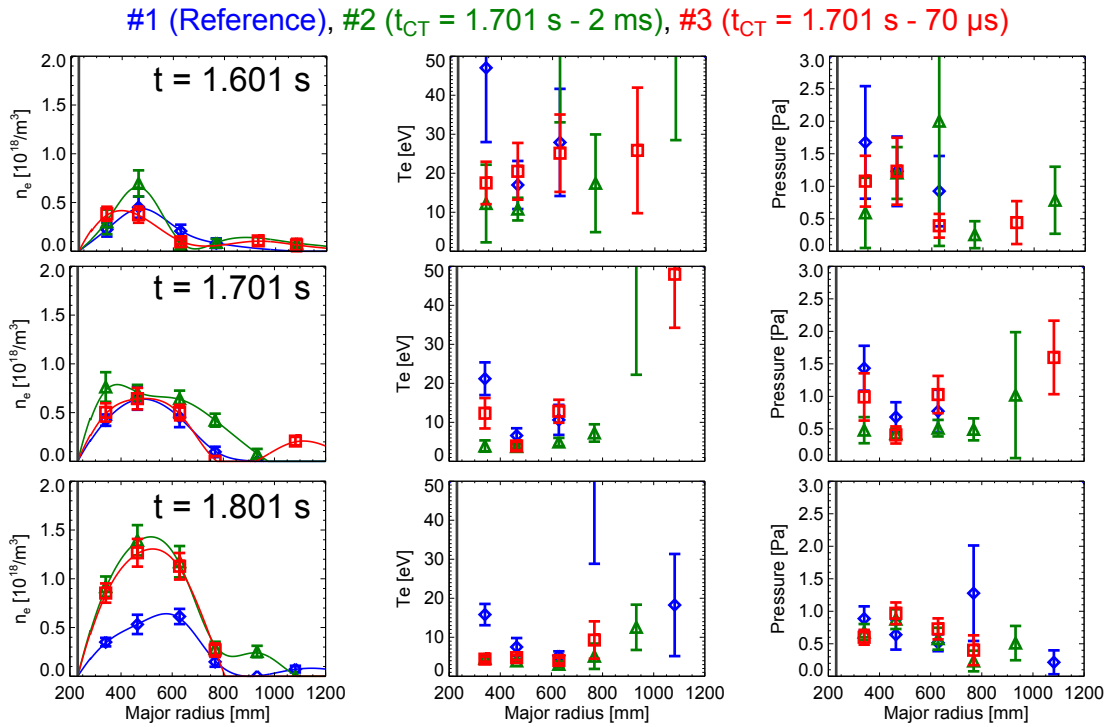

Fig. 5.13: Time evolution of profiles of the electron density (left), temperature (center), and pressure (right) in the three types of discharges corresponding to those in Fig. 5.12.

= 1.801 s, n_e decreases to the same level as that of the reference, where peak positions for both n_e profiles are different each other.

In the previous studies, increase of line-integrated density was observed in two tokamaks, STOR-M and JFT-2M [91, 92]. In the present CT injection experiments, time evolution of n_e and T_e profiles and successful core n_e increase have been measured by the TS diagnostics for the first time.

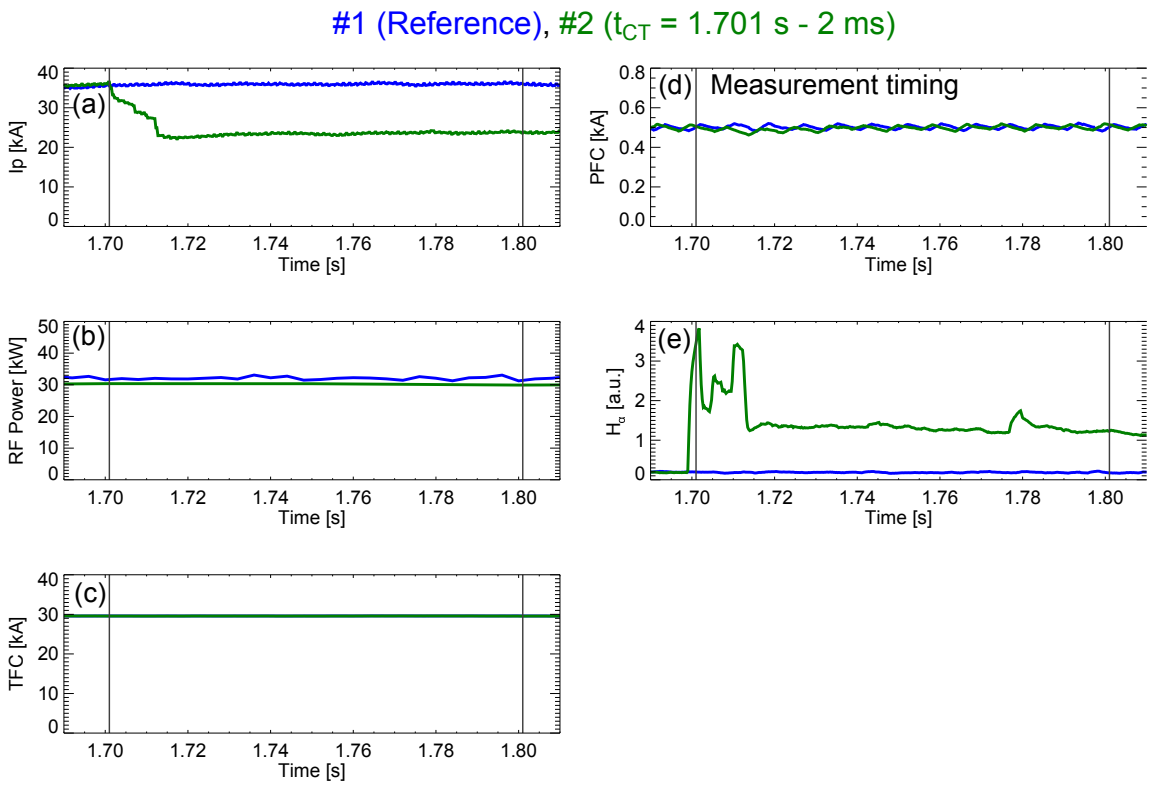

Fig. 5.14: Waveforms of two types of discharges: (1) a reference discharge without CT injection (blue) and (2) a discharge with CT injection 2 ms before the TS measurement at t = 1.701 s (green). The plotted curves are plasma current (a), 8.2 GHz ECW power (b), TF coil current (c), PF coil current (d), and signal of H_α (e). Black vertical lines represent the TS measurement timings.

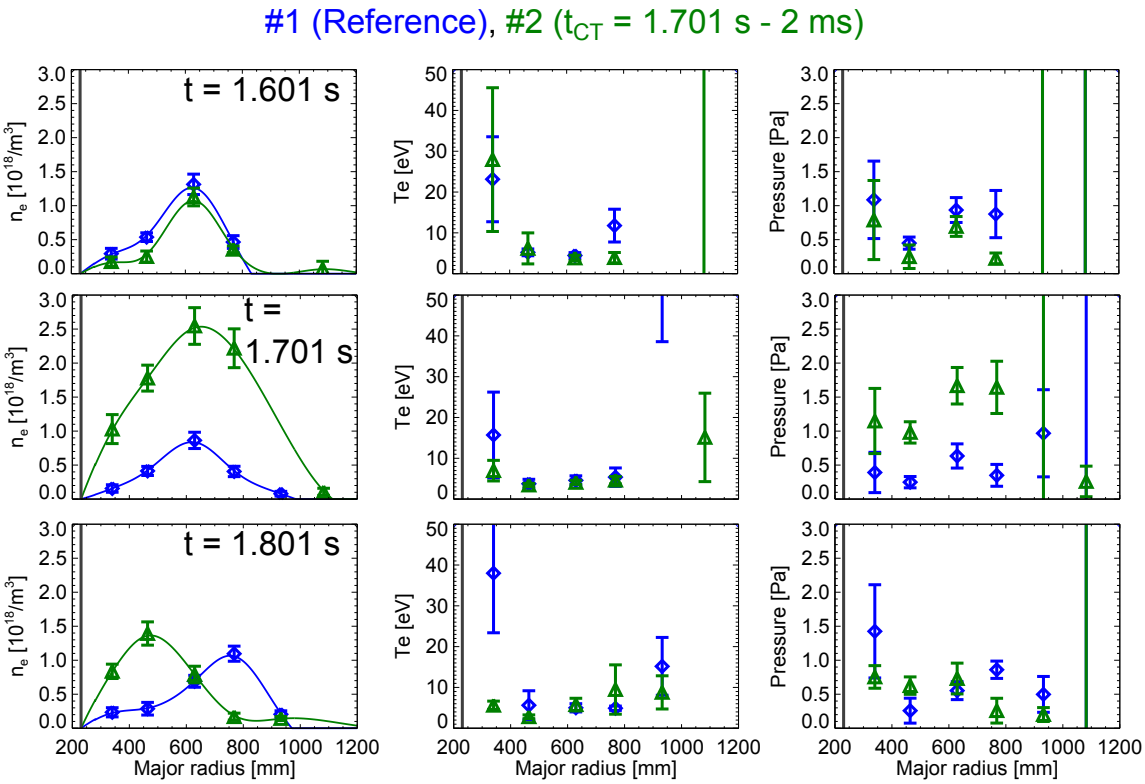

Fig. 5.15: Time evolution of profiles of the electron density (left), temperature (center), and pressure (right) in the reference discharge (blue) and the discharge with CT injection (green) shown in Fig. 5.14.

Chapter 6

Discussion

6.1 Bulk electron heating by fast electrons generated by the LHW in TST-2

The LHW-driven plasmas in TST-2 reported in this study show hollow electron temperature profiles in the order of 1–10 eV. Now plasma heating effect by fast electrons generated by LHW is investigated by calculating zero-dimensional model. Energy of bulk electrons is defined by the product of heating power $P_{\rm heat}$ and energy confinement time $\tau_{\rm E}$, i.e.,

$$\frac{3}{2}\overline{n_{\rm e}}\overline{T_{\rm e,calc}}V_{\rm p} = P_{\rm heat} \times \tau_{\rm E}\ [\rm J], \tag{6.1}$$

where $\overline{n_{\rm e}}$ and $\overline{T_{\rm e,calc}}$ are volume-averaged electron density and temperature, and $V_{\rm p}$ is plasma volume defined as $V_{\rm p} = 2\pi R \times \pi a^2\ [\rm m^3]$. Here, $T_{\rm i} \sim T_{\rm e}/2$ is assumed. Goal of the present calculation procedure is to obtain $\overline{T_{\rm e,calc}}$. Since fast electrons lose its energy through collisions with bulk electrons, the heating power $P_{\rm heat}$ is written by the cooling power of fast electrons averaged over Maxwellian velocity distribution function with the effective temperature of fast electrons $T_{\rm e,fast}$:

$$P_{\rm heat} = \left\langle \frac{m_{\rm e}{v_{\rm e,fast}}^2}{2}\frac{2}{\tau_{\rm s}}n_{\rm e,fast}V_{\rm p} \right\rangle\ [\rm W], \tag{6.2}$$

where $m_{\rm e}$ is electron mass, and $v_{\rm e,fast}$ and $n_{\rm e,fast}$ are velocity and density of the fast electrons, which are defined as

$$v_{\rm e,fast} = \sqrt{\frac{2eT_{\rm e,fast}}{\rm m_e}}\ [\rm m/s], \tag{6.3}$$

$$n_{\rm e,fast} = \frac{I_{\rm p}}{\pi a^2 e v_{\rm e,fast}}\ [\rm m^{-3}], \tag{6.4}$$

where $n_{\rm e,fast}$ is determined by assuming that the plasma current is generated entirely by the fast electrons. Slowing down time $\tau_{\rm s}$ for a fast electron with velocity $v_{\rm e,fast}$ is given by

$$\tau_{\rm s} = \frac{4\pi{\epsilon_0}^2{\rm m_e}^2{v_{\rm e,fast}}^3}{3\overline{n_{\rm e}}e^4\ln\Lambda}\ [\rm s], \tag{6.5}$$

where ϵ_0 is vacuum permittivity and $\ln\Lambda$ is Coulomb logarithm (~ 15). In the assumed distribution function, minimum energy of the existing fast electrons $E_{\rm min}$ is set so that distribution functions of bulk and fast electrons intersect each other at $E_{\rm min}$. $E_{\rm min}$ given here is in the order of 100 eV and calculated heating powers for different $E_{\rm min}$s are almost the same even if $E_{\rm min}$s are varied by a factor of two. Figure 6.1 shows slowing down time for fast electrons, and the heating power distribution $\Delta P_{\rm heat}$, and the distribution as a function of the energy of the fast electrons. The integrated power and integrated distribution function should yield $P_{\rm heat}$ (Eq. (6.2)) and $n_{\rm e,fast}$ (Eq. (6.4)), respectively. The energy confinement time $\tau_{\rm E}$ is given

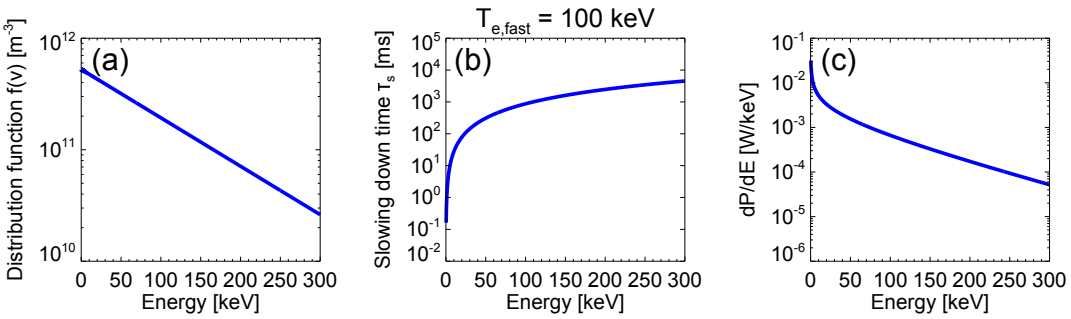

Fig. 6.1: Assumed distribution function of fast electrons (a), slowing down time (b), and the calculated heating power distribution dP/dE (c) as a function of energy of fast electrons.

by empirical scaling law based on data in various devices, and we adopted $\tau_{\rm E}$ for L-mode tokamak plasmas adopted in the design of ITER [1], which is written by

$$\tau_{\rm E} \equiv \tau_{\rm E}^{\rm ITER89-P} = 0.048\kappa^{0.5} B_{\rm t\,[T]}^{0.2} I_{\rm p\,[MA]}^{0.85} \hat{n}_{\rm e\,[10^{20}m^{-3}]}^{0.1} a_{\rm [m]}^{0.3} R_{\rm [m]}^{1.2} A^{0.5} P_{\rm heat\,[MW]}^{-0.5}\ [\rm s], \tag{6.6}$$

where $\hat{n}_{\rm e}$ is line-integrated electron density. From these parameters, resultant $\overline{T_{\rm e,calc}}$ is obtained.

According to Eq. (6.1) and Eq. (6.6), the following dependence is derived:

$$\overline{T_{\rm e,calc}} \propto I_{\rm p}^{0.85} \overline{n_{\rm e}}^{-0.9} P_{\rm heat}^{0.5} B_{\rm t}^{0.2}. \tag{6.7}$$

Electron temperatures for three types of discharges (#1–#3) with plasma currents of 5, 15, and 25 kA are calculated by this procedure. The profiles obtained by the TS measurements for the three types of plasmas are shown in Fig. 6.2. Note that discharge waveforms for #1 and #3 are shown in Fig. B.6 and 4.4, respectively. Given parameters (input) and the calculation results (output) are listed in Tab. 6.1. Here, effective temperatures for the fast electrons are determined based on the results of the HXR measurements shown in Fig. 4.21. Ratios of $n_{\rm e,fast}$ to $\overline{n_{\rm e}}$ are around 1 % and similar to those estimated by EFIT and some diagnostics (described first in this section). Averaged slowing down times $\langle\tau_{\rm s}\rangle$s are in the order of one millisecond and several tens of times shorter than discharge duration of about 100 ms. It is suggested from heating power $P_{\rm heat}$ that less than one percent of injected power $P_{\rm LHW}$ is used for the bulk electron heating. Energy confinement time $\tau_{\rm E}$ is around 10 ms. Resultant electron temperatures $\overline{T_{\rm e,calc}}$s are 36, 87, and 184 eV, respectively. Each calculated temperature $\overline{T_{\rm e,calc}}$ is several times higher than the measured temperature $\overline{T_{\rm e}}$. The bulk electron heating effect becomes stronger and the resultant electron temperature increases with the increase of the plasma current, because the number of fast electrons is proportional to

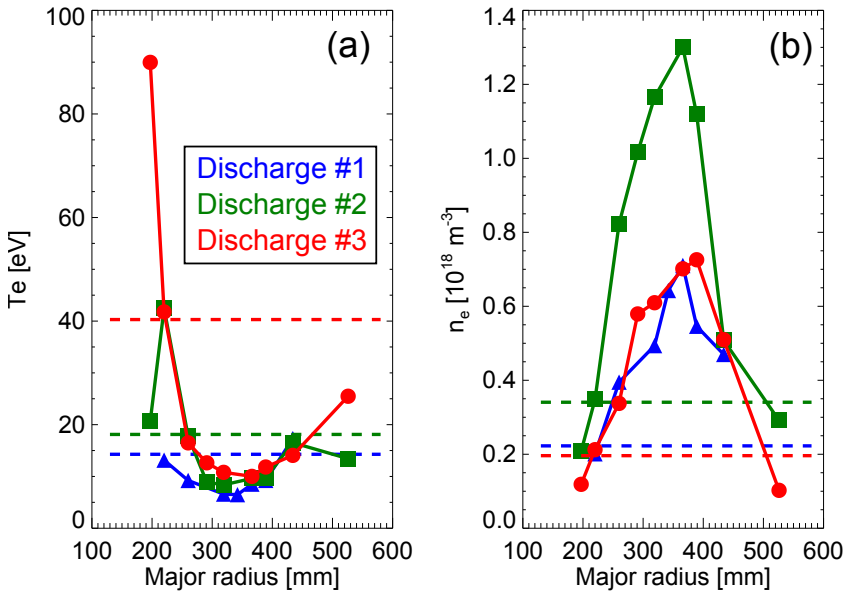

Fig. 6.2: Electron temperature and density profiles measured in discharges #1–3. Each dashed line represents the volume-averaged value.

Input	Discharge #1	Discharge #2	Discharge #3
I_p	5 kA	15 kA	25 kA
a	0.23 m	0.23 m	0.23 m
R	0.36 m	0.36 m	0.36 m
κ	1.4	1.4	1.4
B_t	0.08 T	0.10 T	0.15 T
$T_{e,fast}$	20 keV	60 keV	100 keV
P_{LHW}	20 kW	50 kW	80 kW
$\overline{n_e}$	$2.2 \times 10^{17} m^{-3}$	$3.4 \times 10^{17} m^{-3}$	$2.0 \times 10^{17} m^{-3}$
$\overline{T_e}$	14 eV	18 eV	40 eV
Output	**Discharge #1**	**Discharge #2**	**Discharge #3**
$\ln\Lambda$	14.5	14.6	15.6
E_{min}	116 eV	156 eV	314 eV
$n_{e,fast}$	$2.2 \times 10^{15} m^{-3}$	$3.9 \times 10^{15} m^{-3}$	$5.0 \times 10^{15} m^{-3}$
$\langle \tau_s \rangle$	0.7 ms	1.1 ms	4.7 ms
P_{heat}	200 W	353 W	215 W
$\tau_E^{ITER89-P}$	3.6 ms	7.6 ms	15 ms
$\overline{T_{e,calc}}$	36.2 eV	87.1 eV	184 eV

Tab. 6.1: Given parameters (input) and the calculated ones (output) for discharges #1–3.

the the plasma current in the present analysis.

Here we discuss I_p and n_e dependences of $\overline{T_{e,calc}}$ by comparing #1 & #3 and #1 & #2, respectively. In the case of #1 & #3, I_ps and B_ts show 5 and 2 times difference, respectively, and $\overline{n_e}$s are almost same. As a result, P_{heat}s are almost same. Using the I_p and B_t dependence (Eq. (6.7)), T_e should be proportional to $I_p^{0.85} B_t^{0.2} = 5^{0.85} \times 2^{0.2} \sim 5$, which agree with the ratio of $\overline{T_{e,calc}} = 184/36 \sim 5$. In the case of #1 & #2, we should consider the n_e and P_{heat} difference, and then we can explain the ratio of $\overline{T_{e,calc}}$: $I_p^{0.85} B_t^{0.2} \overline{n_e}^{-0.9} P_{heat}^{0.5} = 3^{0.85} \times 1.3^{0.2} \times 1.5^{-0.9} \times 1.7^{0.5} \sim 2.4$, which agree with the ratio of $\overline{T_{e,calc}} = 87/36 \sim 2.4$.

Here current dependence of $\overline{T_{e,calc}}$ and P_{heat} are investigated, where other parameters are fixed (same as those in discharge #3). Figure 6.3 shows the calculation result. Although

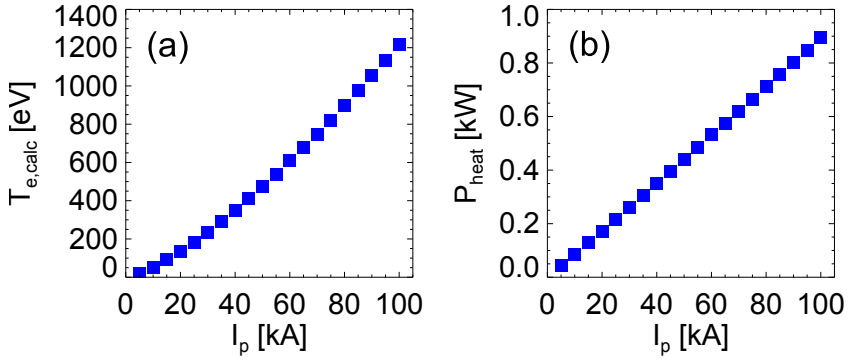

Fig. 6.3: Plasma current dependence of calculated electron temperature $\overline{T_{e,calc}}$ (a) and heating power P_{heat} (b) for given $\overline{n_e} = 2.0 \times 10^{17} m^{-3}$, and $T_{e,fast} = 100$ keV.

strong dependence is shown as expected, it seems due to strong current dependence of the energy confinement time τ_E. Figure 6.4 shows $T_{e,fast}$ dependence of $\overline{T_{e,calc}}$ and P_{heat}, and it is indicated that the heating effect becomes significant when $T_{e,fast}$ becomes lower. This is because the slowing down time τ_s is shorter at the lower energy, leading to rapid heating.

As a result, it is found qualitatively that the observed bulk electron temperatures of 10-100 eV can be explained by slowing down of the fast electrons generated by the LHW. This also implies that energy confinement time is not so far from that calculated from the ITER L-mode scaling law. Note that absorption profile of LHW, three-dimensional effect including diffusion and transport, velocity distribution function of fast electrons, and accurate energy confinement time should be given for further detailed investigation.

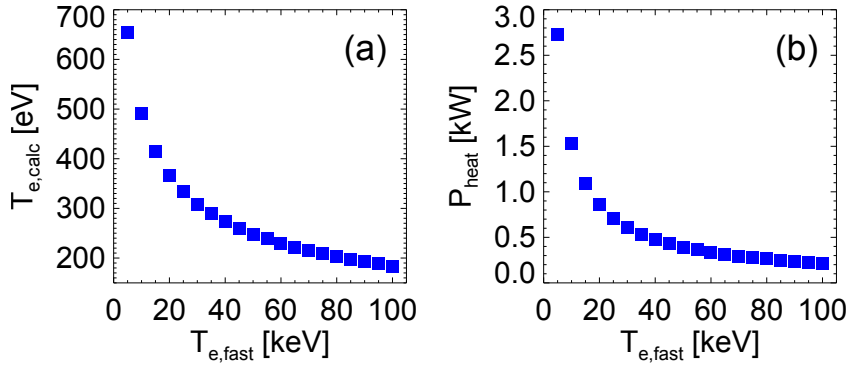

Fig. 6.4: Fast electron's temperature dependence of electron temperature $\overline{T_{\mathrm{e,calc}}}$ (a) and heating power P_{heat} (b). Here $\overline{n_{\mathrm{e}}}$ and I_{p} are $2.0 \times 10^{17}\mathrm{m}^{-3}$ and 25 kA.

6.2 Contribution of neutral particles in the formation of hollow temperature profiles

Here, we consider influence of neutral particles (deuterium here) on the electron temperature. Interactive processes between neutral particles and plasma particles (ions and electrons) are mainly (1) ionization, (2) charge-exchange, and (3) radiative recombination. Figure 6.5 shows schematic of each process. Ionization is a generation process of an electron

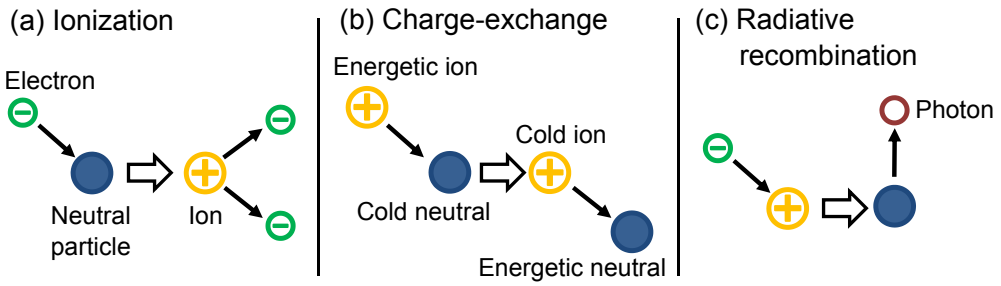

Fig. 6.5: Three types of processes between neutral particles and plasma particles (electrons and ions), i.e., ionization (a), charge-exchange (b), and radiative recombination (c).

and an ion due to collision between a neutral particle and an electron. Charge-exchange is a transfer process of an electron between a neutral particle to an ion. Radiative recombination process generates a neutral particle from an ion and an electron, leading to emission of light. These three types of processes in TST-2 plasmas are investigated. Profiles of electron temperatures and densities of Ohmically heated and LHW-driven plasmas (Fig. A.1 and 4.4). Those profiles are shown in Fig. 6.6. Here, quasi-neutrality ($n_e \sim n_i$) is assumed. Profile of ion temperature T_i for the Ohmically heated plasma is given as half value of the T_e profile, while T_i profile for the LHW-driven plasma is given as a flat one with 5 eV, which is typical according to the spectrometry measurements. Given density profile of neutral particles (deuterium gas) is plotted in Fig. 6.7. The flat profile is assumed and the value is roughly estimated based on the filling pressure. As shown in later, the flat shape is reasonable for the LHW-driven plasmas, but not reasonable for the Ohmically heated plasmas. According to Ref. [41], ionization and radiative recombination rates averaged over Maxwellian distribution function are given by

$$\langle \sigma_{\rm ion} v_e \rangle = \frac{2.0 \times 10^{-13}}{6.0 + T_e/13.6} \left(\frac{T_e}{13.6} \right)^{1/2} \exp\left(-\frac{13.6}{T_e} \right) \ [\mathrm{m^3 s^{-1}}], \tag{6.8}$$

$$\langle \sigma_{\rm rec} v_e \rangle = 0.7 \times 10^{-19} \left(\frac{13.6}{T_e} \right) \ [\mathrm{m^3 s^{-1}}]. \tag{6.9}$$

Charge-exchange rate $\langle \sigma_{\rm cx} v_i \rangle$ calculated from the cross section given in the reference is shown in Fig. 6.8. Source rate per unit volume in each process is obtained by

$$S_{\rm ion} = n_e n_n \langle \sigma_{\rm ion} v_e \rangle \ [\mathrm{m^{-3} s^{-1}}], \tag{6.10}$$

$$S_{\rm cx} = n_i n_n \langle \sigma_{\rm cx} v_i \rangle \ [\mathrm{m^{-3} s^{-1}}], \tag{6.11}$$

$$S_{\rm rec} = n_e n_i \langle \sigma_{\rm rec} v_e \rangle \ [\mathrm{m^{-3} s^{-1}}]. \tag{6.12}$$

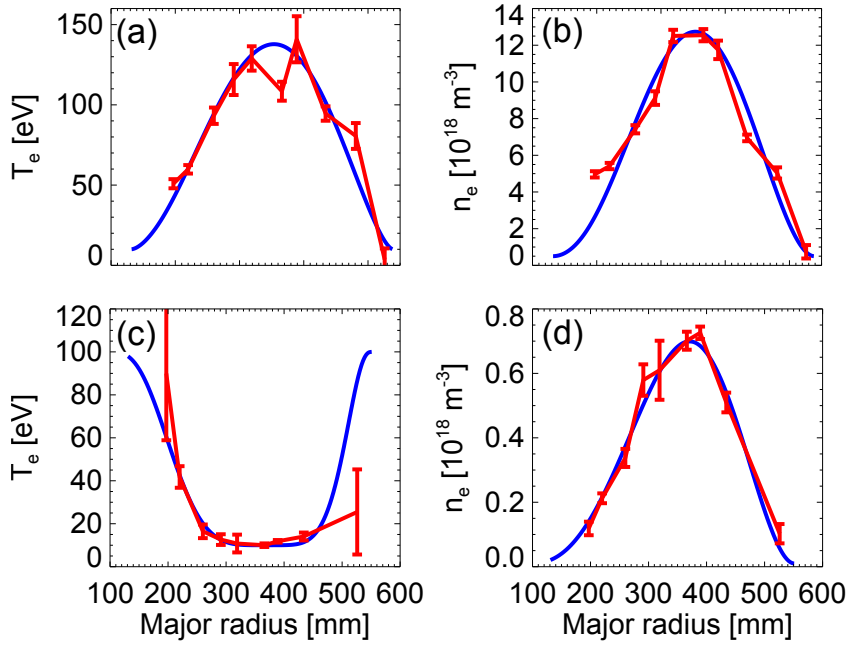

Fig. 6.6: Electron temperature and density profiles used in the calculation. (a) and (b) show profiles measured for Ohmically heated plasmas and (c) and (d) for LHW-driven plasmas. Red symbols represent the measurement values and blue ones are approximated profiles as a function of magnetic surface obtained from the EFIT code. Here, peak positions for (c) and (d) are shifted arbitrarily.

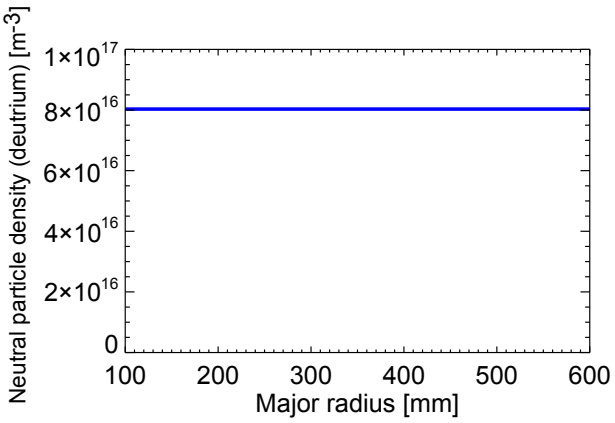

Fig. 6.7: Given density profile of neutral particles (deuterium gas).

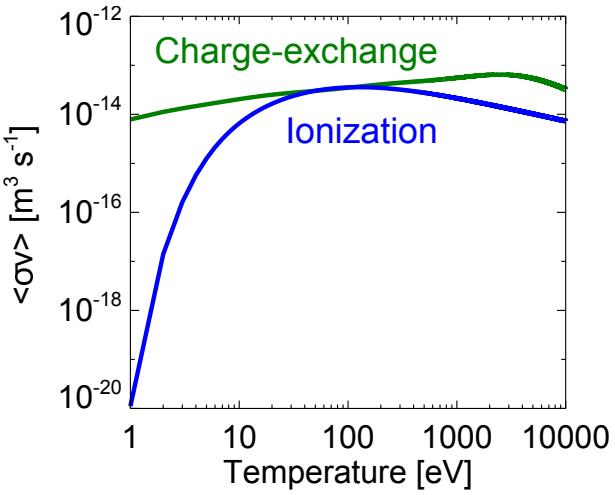

Fig. 6.8: Ionization rate $\langle \sigma_{\rm ion} v_{\rm e} \rangle$ (blue) and charge-exchange rate $\langle \sigma_{\rm cx} v_{\rm i} \rangle$ (green).

$S_{\rm ion}$ is the same as the source rate of electrons, and it is also the same as the extinction rate of neutral particles in the ionization process. $S_{\rm cx}$ indicates rates of decrease of ion's energy and increase of neutral particle's energy in the charge-exchange process. $S_{\rm rec}$ shows source rate of neutral particles and photons and extinction rate of electrons and ions in the radiative recombination process. Profiles of the source rates were calculated using the profiles shown in Figs. 6.6 and 6.7. Figure 6.9 shows the calculation result. As shown in the figure, source

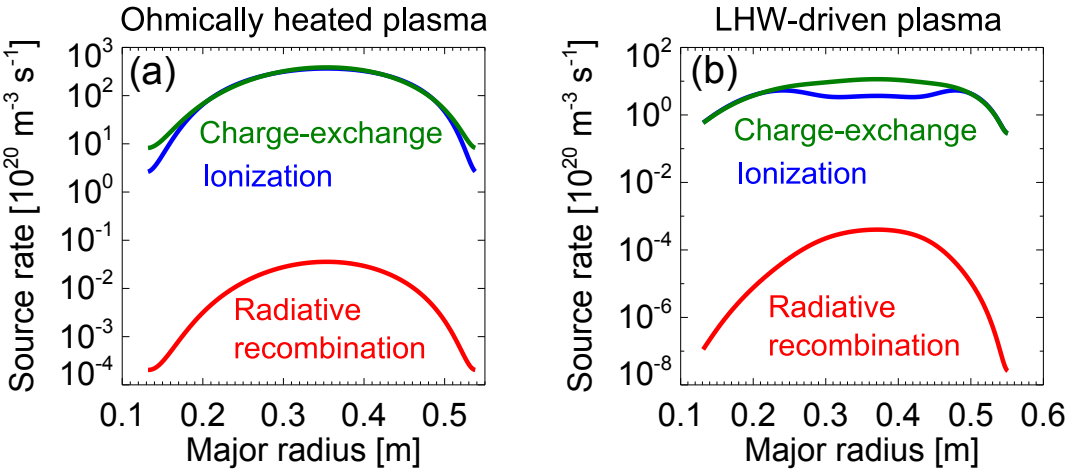

Fig. 6.9: Profiles of source rate of ionization $S_{\rm ion}$ (blue), charge-exchange $S_{\rm cx}$ (green), and radiative recombination $S_{\rm rec}$ (red) for the Ohmically heated plasma (a) and for the LHW-driven plasma (b).

rate of cold neutral particles in radiative recombination $S_{\rm rec}$ is quite smaller than the others and it is negligible in both Ohmically heated and LHW-driven plasmas. Mean-free-path in

each process is calculated by

$$\lambda_{\mathrm{ion}} = \frac{v_{\mathrm{n}}}{n_{\mathrm{e}}\langle\sigma_{\mathrm{ion}}v_{\mathrm{e}}\rangle}\ [\mathrm{m}], \tag{6.13}$$

$$\lambda_{\mathrm{cx,slow}} = \frac{v_{\mathrm{n}}}{n_{\mathrm{i}}\langle\sigma_{\mathrm{cx}}v_{\mathrm{i}}\rangle}\ [\mathrm{m}], \tag{6.14}$$

$$\lambda_{\mathrm{cx,fast}} = \frac{v_{\mathrm{i}}}{n_{\mathrm{i}}\langle\sigma_{\mathrm{cx}}v_{\mathrm{i}}\rangle}\ [\mathrm{m}],\ \text{and} \tag{6.15}$$

$$\lambda_{\mathrm{rec}} = \frac{v_{\mathrm{i}}}{n_{\mathrm{e}}\langle\sigma_{\mathrm{rec}}v_{\mathrm{e}}\rangle}\ [\mathrm{m}], \tag{6.16}$$

where the $\lambda_{\mathrm{cx,slow}}$ and $\lambda_{\mathrm{cx,fast}}$ denote mean-free-paths for charge-exchange process for initial cold neutral particles and energetic ones after the process, respectively. v_{n} is thermal velocity of neutral particles calculated from room temperature of 300 K. Since fuel gas is injected from the outboard side of the vacuum vessel in TST-2, each mean-free-path can be interpreted as the penetration length into a plasma. The profiles are shown in Fig. 6.10. In the Ohmically heated plasma, mean-free-paths for ionization and charge-exchange, i.e.,

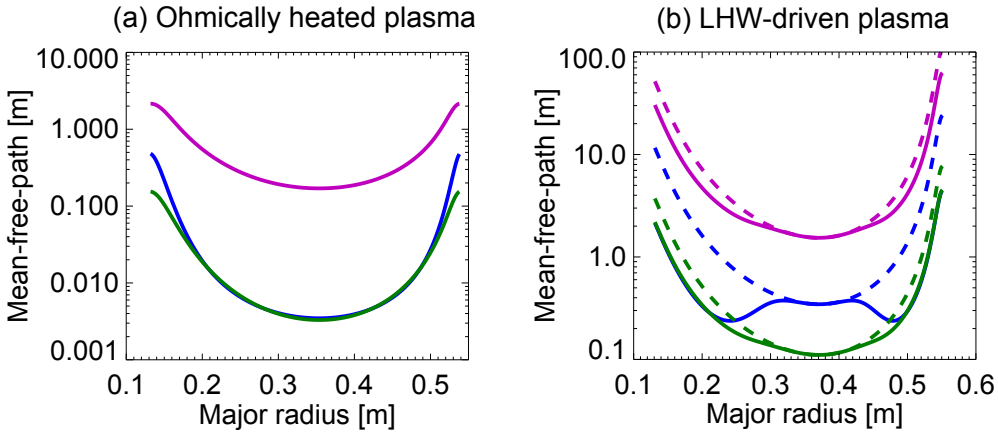

Fig. 6.10: Profiles of mean-free-paths for ionization (blue) and charge-exchange (green and purple for cold and energetic neutral particles, respectively) processes for the Ohmically heated plasma (a) and for the LHW-driven plasma (b). Dashed curves in (b) represent those in a 10 eV flat T_{e} profile. Note that mean-free-path in radiative recombination process for each plasma is more than 10^5 m.

λ_{ion} and $\lambda_{\mathrm{cx,slow}}$ are less than 1 cm at the core region, and it can be said that most of the cold neutral particles, which lead to energy loss of the plasma, are ionized at the peripheral region. In this case, shape of the profile of neutral particle density should be changed to a hollow. On the other hand, λ_{ion} and $\lambda_{\mathrm{cx,slow}}$ for the LHW-driven plasma are similar level to the plasma minor radius ($a \sim 0.23$ m), and it is suggested that neutral particles can move freely in the plasma, and energetic neutral particles generated by the charge-exchange process can run away from the plasma volume without ionization again. It may cause decrease of ion temperature. Dashed curves in Fig. 6.10 show mean-free-path profiles for a plasma with a 10 eV flat T_{e} profile. Neutral particles can move in the plasma freely even with the flat (not hollow) T_{e} profile. Note that mean-free-path in radiative recombination process for each plasma is more than 10^5 m.

Although charge-exchange process does not affect electron temperature directly, thermal relaxation occurs between ions and electrons, and it may lead to decrease of the electron temperature. Then the thermal relaxation time between ions and electrons is calculated by the following equation:

$$\tau_{\mathrm{eq}}^{-1} = \frac{n_{\mathrm{e}} Z^2 e^4 m_{\mathrm{e}}^{1/2} ln\Lambda}{3\pi(2\pi)^{1/2}\epsilon_0^2 \mathrm{m_i}(eT_{\mathrm{e}})^{3/2}}. \tag{6.17}$$

Figure 6.11 shows the result. τ_{eq} for the Ohmically heated plasma is in the order of several milliseconds, while τ_{eq} longer than 100 ms at the peripheral region and τ_{eq} of a few milliseconds at the core region are shown for the LHW-driven plasma. Similar tendency is shown for the LHW-driven plasma with a 10 eV flat temperature (shown as a dashed curve in the figure). Therefore, it is suggested that cooling down of electron temperature at the core region keeps the hollow T_{e} profile.

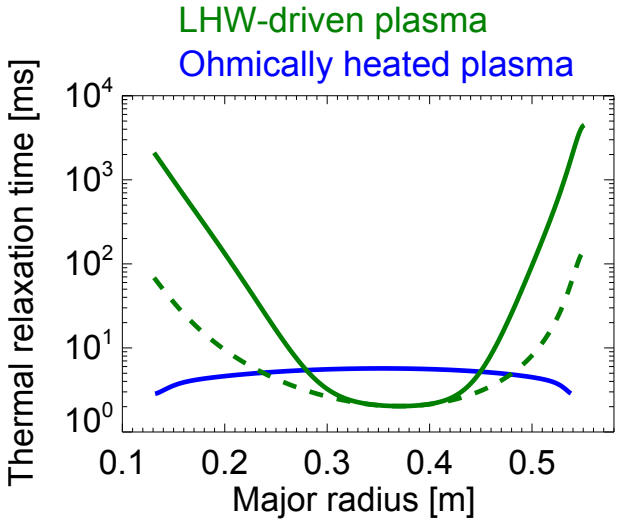

Fig. 6.11: Thermal relaxation time τ_{eq} between ions and electrons for the Ohmically heated plasma (blue) and for the LHW-driven plasma (green). Dashed curves represent τ_{eq} in a 10 eV flat T_{e} profile.

Influence of radiation due to collision of electrons with impurity ions is mentioned in the past. In experiments of JET with the ITER-like wall, tungsten impurities induce strongly peaked density and radiation profiles, leading to a hollow T_{e} profile [93]. In TST-2, total radiation power was estimated by using spectrometer and soft X-ray measurements independently, and both results were in the order of 100 W [94, 95]. Profile of radiated power is proportional to profiles of impurity ions and electrons. Thus, in TST-2 LHW-driven plasmas with peaked n_{e} profiles, significant energy loss at the core due to the radiation may occur.

Here, total power loss due to the charge-exchange process is calculated and compared with that due to the radiation. Volume-averaged source rate and the plasma volume are calculated to be $\langle S_{\mathrm{cx}} \rangle = 5 \times 10^{20}$ m^{-3} s^{-1} and $V_{\mathrm{p}} = 0.4$ m^3, respectively. Volume-averaged ion temperature is determined as $\langle T_{\mathrm{i}} \rangle = 5$ eV from the spectrometry. Then the total power is calculated as $P_{\mathrm{cx}} = \langle S_{\mathrm{cx}} \rangle \times V_{\mathrm{p}} \times \langle T_{\mathrm{i}} \rangle \times 1.6 \times 10^{-19} = 160$ W. This is the same order as the radiated power. Therefore, both processes can invoke the bulk electron cooling near the

center.

Similarly to the investigation of heating effect due to the fast electrons, calculation of the energy losses may include large ambiguity because of the simplicity of the adopted model and because of the lack of accurate parameters (e.g. density profile of neutral particles and ion temperature profile). As a result, total loss power due to the charge-exchange and the radiation is estimated to be same or higher level than the total heating power calculated in Sec. 6.1. Thus, detailed measurement and analysis are necessary to obtain accurate power balance and reveal the formation mechanism of the hollow T_e profile.

6.3 Simulation using GENRAY/CQL3D

In order to investigate T_e dependence of driven current, the ray-tracing code GENRAY and Fokker-Planck code CQL3D were utilized. The target plasma has an I_p of 25 kA and its waveforms are shown in Fig. 4.4. Result of equilibrium reconstruction by EFIT code and n_e profile obtained from the TS measurement are used as an input of the ray-tracing simulation. In order to see the effect of temperature profile, the following two types of T_e profiles are applied; #1: a hollow T_e profile with 10 eV at the core and 100 eV at the edge and #2: a 100 eV flat profile. In addition, it is assumed that LHW can propagate at the scrape-off-layer (SOL). Using these parameters and result of the ray-tracing, current density profile is simulated by the CQL3D, which calculates time evolution of the velocity distribution function of plasmas. Resultant current density profiles are shown in Fig. 6.12. Total plasma currents are calculated to be 53 and 101 kA for the cases #1 and #2, respectively. Therefore, it is suggested that absorption of LHW at the core region is preferred and central heating is desired to achieve higher plasma current. Although T_e profile obtained in the experiment is similar to that in case #1, the simulated plasma current is approximately 5 times higher than that in the experiment. This discrepancy may be caused because orbit width of the electrons is not taken into account in the CQL3D. In order to reveal the cause of the discrepancy, new diagnostics (e.g., a polarimeter and microwave scattering diagnostic) and/or extension of the simulation may be necessary.

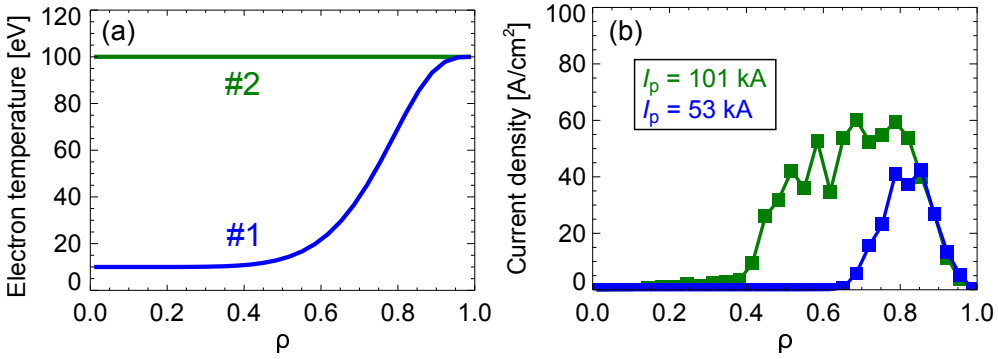

Fig. 6.12: T_e profiles used in the simulation (a) and resultant current density profiles (b). Each color of (a) and (b) corresponds.

The CQL3D also provides modeling of HXR measurement for the simulated plasma. Firstly, validity of the modeling is confirmed by comparing energy flux spectra between the simulation and theoretical value given by Eq. (3.1) and length of line-of-sight. Here CQL3D

calculates the spectrum of energy flux for a plasma with a 30 keV flat temperature profile and a flat density of $5\times10^{17}\mathrm{m}^{-3}$. The comparison is shown in Fig. 6.13 and good agreement is confirmed.

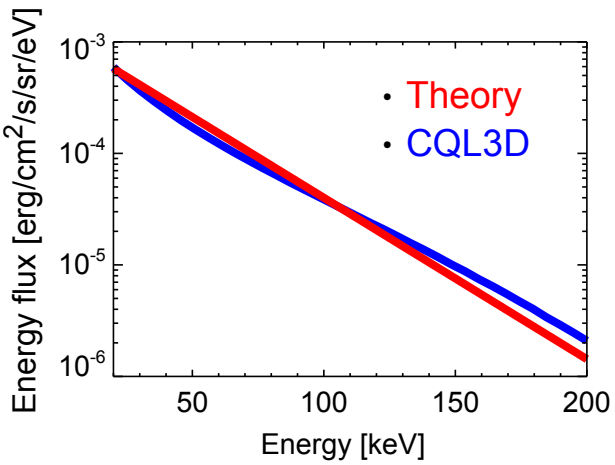

Fig. 6.13: Comparison of energy flux spectra between the simulation (CQL3D) and theoretical value calculated from Eq. (3.1). The target plasma has a 30 keV flat temperature profile and a flat density profile with $5\times10^{17}\mathrm{m}^{-3}$, and the lecgth of the line of sight is 0.64 m.

Secondly, profiles of energy flux between the simulation and the experiment are compared. Given parameters (i.e., profiles of temperature and density, EFIT calculation result including magnetic surfaces) are based on those in the experiment shown in Fig. 4.15 (t = 45 ms) and the measurement chords are the same as those in the experiment. Similarly to the profiles measured so far, a hollow T_e profile with 10 eV at the core and 50 eV at the edge and a peaked n_e profile with $5\times10^{17}\mathrm{m}^{-3}$ at the center are assumed. Figures 6.14 and 6.15 show the resultant current density profile and the energy flux profile, respectively. Comparison of energy spectra at R_tan = 360 mm between the simulation and the measurement is shown in Fig. 6.16. Energy fluxes for both cases are the same level at a few tens of keV, but effective temperatures are quite different (3.7 keV and 26 keV for the simulation and the experiment, respectively). Comparison of energy flux profiles integrated over 15–100 keV is shown in Fig. 6.17. Flux in the experiment is about 5 times higher than that in the simulation. Since each value is smoothed due to the finite solid angle in the experiment, similar effect is added to the simulated profile (solid red lines in Fig. 6.17) to compare the results with each other. As a result, similar tendency between the simulation and the experiments is indicated: flux at the inboard side is higher than that at the outboard side. In addition, energy flux in the SOL is seen only in the experiment, and it is suggested that significant LHW power is absorbed in the SOL. Thus it may be necessary to extend CQL3D code to obtain correct current density and energy flux profiles. Note that the simulated plasma current of 46 kA is about 5 times larger than that in the experiment, while the simulated energy flux is much lower than the experimental value. This discrepancy may occur when strong radiation outside the LCFS and/or toroidal asymmetry of the radiation exist.

Shape of current density profile is considered here. Various profiles are given and the line-integrated values in viewing chords are calculated as a energy flux profile to compare with the flux profile obtained experimentally. Figure 6.18 shows the examples. In order

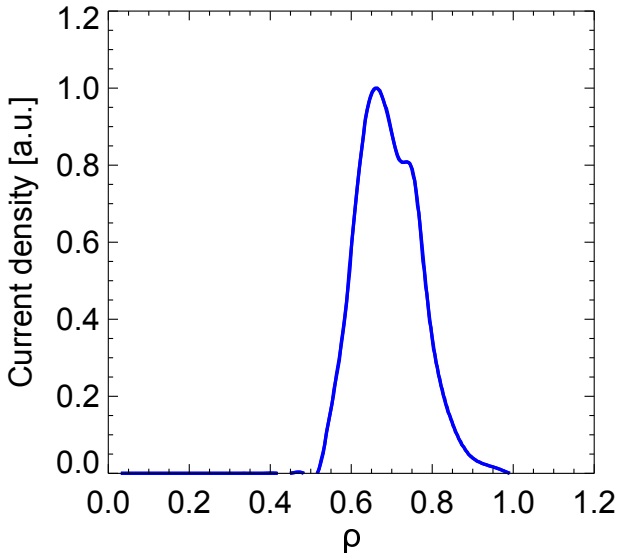

Fig. 6.14: Toroidal current density profile simulated by the CQL3D code for the plasma shown in Fig. 4.15 at t = 45 ms.

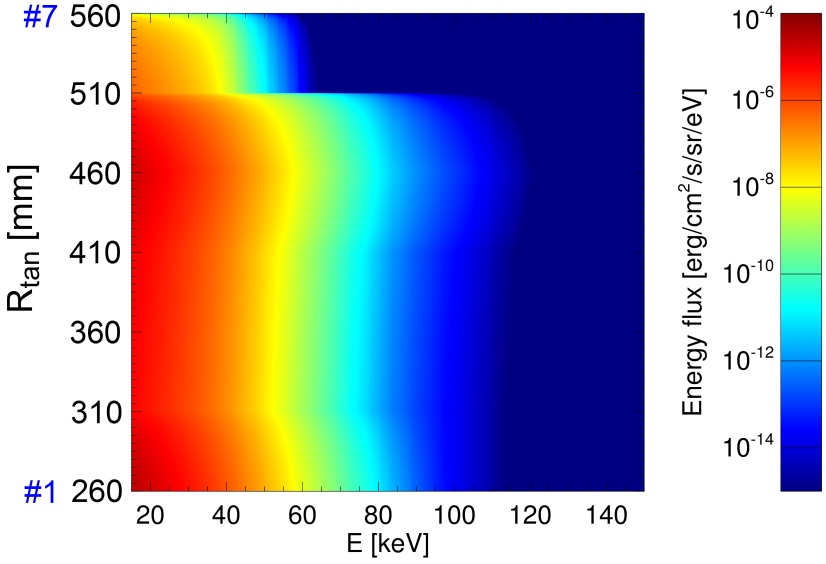

Fig. 6.15: Simulated energy flux profile.

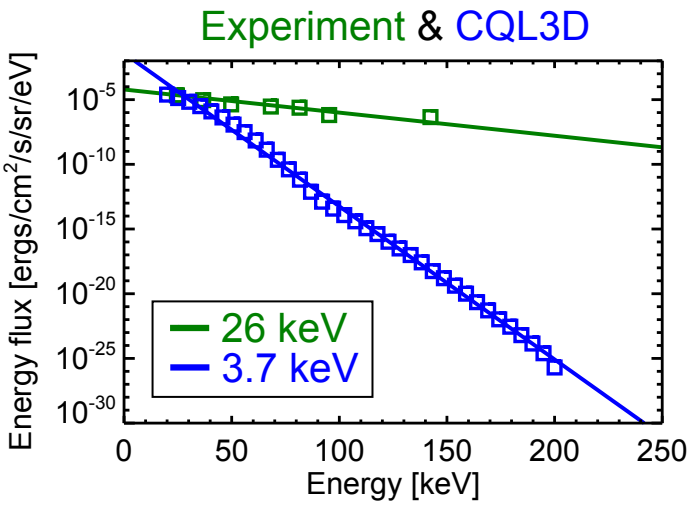

Fig. 6.16: Energy flux spectra for the experiment (green) and the simulation (blue).

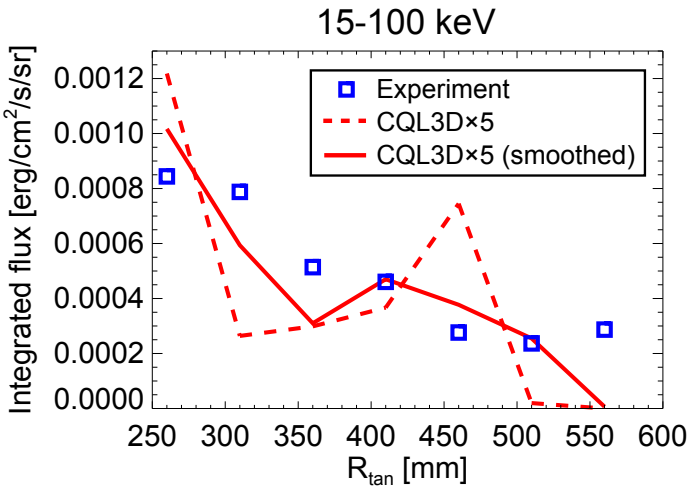

Fig. 6.17: Profiles of energy flux integrated over 15–100 keV. Blue squares and red broken lines represent experimental and simulated results, respectively. Simulated result including smoothing effect due to the finite solid angle is represented as red lines.

to roughly simulate the effect of the finite solid angle, each result is calculated as average of line-integrated values calculated in three viewing chords with 0 and ±85 mrad at the midplane. Right figures in (a) and (b) show profiles of calculated line-integrated values in two cases, where current density is localized at the peripheral region (a) and the core region (b). Both profiles are quite different from the experimental result, and it is suggested that actual current density profile does not have a steep single peak. Although similar tendency with the experiment is shown in (c) with a flat current density profile, more close profile is obtained in the case (d) with current density profile with two peaks at SOL and the inner side of the plasma. In the case (e) without current at the SOL, discrepancy with the experiment can be seen at the outer region. Figure (f) shows one of the examples indicating that similar profile is reproducible by preparing multi-peak current density profiles with various peak amplitudes and the widths. Note that detailed shape of the energy flux profile cannot be revealed by this analysis because angular distributions of Bremsstrahlung (shown in Fig. 3.1), which can modify the energy flux profile somewhat, is not taken into account in the calculation. Also in the experimental side, spatial resolution in the present system is not so high and this increases the ambiguity of the flux profile estimation. The use of a smaller pinhole and extension of viewing chords including poloidal angle will give us more detailed information.

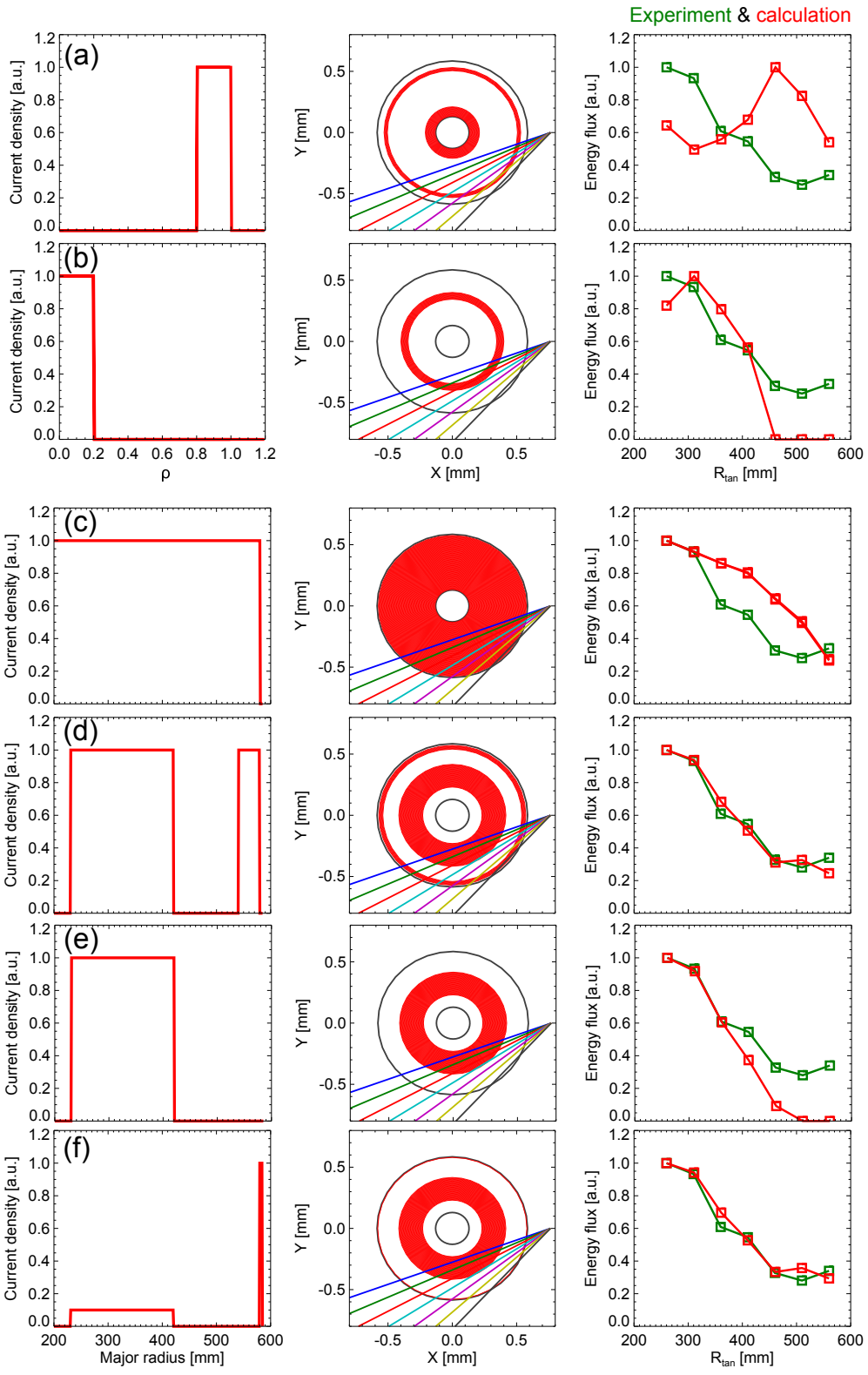

Fig. 6.18: Examples of calculation of normalized energy flux profile (i.e., profile of line-integrated value of current density). Given current density profiles (left), two-dimensional current density profiles and viewing chords (center), and normalized energy flux profiles for the calculation and the experiment (right) are shown.

6.4 Proposal of EBW central heating by X-B scenario

In JT-60 and ASDEX, temperature dependence of the lower hybrid current drive efficiency was shown [96]. In TST-2, it is suggested from simulation by using GENRAY/CQL3D that central heating is important to improve the efficiency. Then, additional central heating and current drive scenario by the use of electron Bernstein wave (EBW) is considered. Various frequencies in plasmas are defined by the following equations [98]:

$$\omega_{\mathrm{pc}} = \sqrt{\frac{e^2 n_{\mathrm{e}}}{\epsilon_0 m_{\mathrm{e}}}}, \tag{6.18}$$

$$\Omega_{\mathrm{ce}} = \frac{eB}{m_{\mathrm{e}}}, \tag{6.19}$$

$$\omega_{\mathrm{R}} = \frac{\Omega_{\mathrm{ce}} + \sqrt{\Omega_{\mathrm{ce}}^2 + 4\omega_{\mathrm{pc}}^2}}{2}, \tag{6.20}$$

$$\omega_{\mathrm{L}} = \frac{-\Omega_{\mathrm{ce}} + \sqrt{\Omega_{\mathrm{ce}}^2 + 4\omega_{\mathrm{pc}}^2}}{2}, \tag{6.21}$$

$$\omega_{\mathrm{UH}} = \sqrt{\Omega_{\mathrm{ce}}^2 + \omega_{\mathrm{pc}}^2}, \tag{6.22}$$

$$\tag{6.23}$$

where ω_{pc} is plasma cutoff frequency, Ω_{ce} is electron cyclotron frequency, ω_{R} and ω_{L} are right-hand and left-hand cutoff frequencies, and ω_{UH} is upper hybrid resonance frequency. Since EBW is a kind of longitudinal wave and cannot propagate in vacuum, it should be converted from ECW. There are two types of modes in ECW, i.e., O-mode and X-mode of which electric fields are parallel and perpendicular to the magnetic field, respectively. Figure 6.19 shows the profiles of various frequencies calculated from the profiles of toroidal magnetic field and electron density at the midplane for the discharge shown in Fig. B.6. Consider injection of 2.45 GHz ECW from the outboard side at the midplane. In O-mode

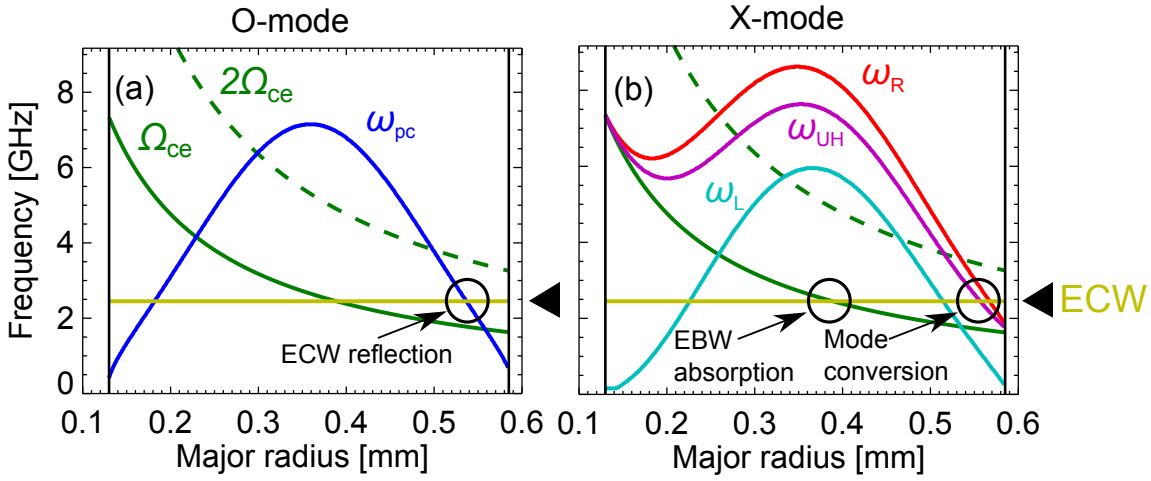

Fig. 6.19: Profiles of frequencies to O-mode (a) and X-mode (b) calculated for a discharge shown in Fig. B.6 at $t = 85$ ms.

injection, ECW is reflected by the plasma cutoff at $\omega_{EC} = \omega_{pc}$, and thus cannot propagate inside the plasma. Such plasma is called an over-dense plasma. ECW in X-mode faces right-hand cutoff and a part of the power passes through as an evanescent wave. If the density gradient is steep and the distance between the positions of $\omega_{EC} = \omega_R$ and $\omega_{EC} = \omega_{UH}$, is sufficiently short, a mode conversion of ECW to EBW occurs. Here, maximum conversion efficiency C_{max} is given by [97]

$$C_{max} = 4e^{-\pi\eta}(1 - e^{-\pi\eta}), \tag{6.24}$$

$$\tag{6.25}$$

where

$$\eta \sim \frac{\omega_c L_n}{c\alpha}[\sqrt{1+\alpha^2} - 1]^{1/2}, \tag{6.26}$$

$$\alpha = (\omega_p/\omega_c)\,|_{UHR}\ . \tag{6.27}$$

$$\tag{6.28}$$

In this situation, $\eta \sim 0.6$ and C_{max} is about 50 %. Since there is no cutoff for EBW, it is absorbed near the electron cyclotron resonance layer after passing through the left-hand cutoff. Although it is a very rough estimation, this scenario is a possible candidate of additional central heating and current drive. Note that a similar EBW experiments have been performed successfully for Ohmically heated over-dense plasmas in TST-2 [15]. In addition, EBW scenario using 8.2 GHz and 28 GHz ECWs has been considered in QUEST, but the maximum conversion efficiency was 2% because it is difficult to make an over-dense plasma with steep density profile only by ECW [39]. In the case of TST-2 LHW-driven plasma, the plasma can be over-dense for the ECW (2.45 GHz), and high C_{max} is expected.

Chapter 7

Conclusions

As a possible candidate of fusion reactors, tokamak has been studied. In particular, spherical tokamak (ST) has high efficiency and stability in the plasma confinement, but plasma current has to be started-up non-inductively and the scenario has not been established. In order to reveal the features of bulk and fast electrons, which play critical roles in RF start-up and to elucidate the characteristics peculiar to RF start-up plasmas, two diagnostic systems were developed and applied to TST-2 and QUEST.

A coaxial multi-pass TS diagnostic system developed in the previous study in TST-2 was upgraded, resulting in reduction of the loss per round trip from 30 % to 20 %. Then, twice higher SNR than that in the first pass is expected. By applying new APDs with higher sensitivity around YAG wavelength, SNR was improved by 2.4 times as expected.

Non-inductive plasma current start-up experiments with the maximum current of 25 kA by using an outboard-launch CCC antenna were performed in TST-2. Using the TS diagnostic system, T_e and n_e profiles were obtained for the first time in LHW-driven ST plasmas. As a result, hollow T_e profiles with around 10 eV at the core and around 50 eV at the inboard side and peaked n_e profiles were obtained. Magnetic axis estimated from the TS measurements is slightly different from that calculated by EFIT code, while good agreement is shown in Ohmic discharge. From TS measurements for some types of plasmas with different plasma current, it is suggested that T_e increases with the increase of the plasma current. Current start-up experiments with the current of 12 kA using a top-launch CCC antenna were performed, and similar profiles were obtained. Existence of temperature anisotropy was investigated by applying coaxial double-pass TS scheme, and the resultant temperatures parallel and perpendicular to the magnetic field were isotropic within about 10% error.

An HXR diagnostic system was developed and the measurements were performed for LHW-driven plasmas in TST-2. It was implied that effective temperature of fast electrons increases with plasma current. Energy flux profile of HXR (integrated over 15–100 keV) measured for plasmas with $I_p \sim 10$ kA showed that flux at the inboard side is higher than that at the outboard side. Modeling of the HXR measurement by the use of GENRAY/CQL3D codes including results of the TS measurements and the EFIT calculation was carried out. As a result, shape of the calculated energy flux profile was roughly similar to that in the experiments but the effective temperature was about seven times lower. Here, toroidal current density profile was simulated, and it is indicated that fast electrons contributing to the current are generated at a region of $\rho = 0.5$–1.0.

Bulk electron pressures obtained by the TS measurements were around 1 Pa, while equilibrium plasma pressures calculated by the EFIT code were in the range of 20–200 Pa.

Taking ion temperatures of several electron volts and effective temperatures of fast electrons of about 10–100 keV into consideration, it is suggested that minor fast electrons contribute to the plasma pressure.

Detailed profiles for QUEST plasmas with IPN configuration were obtained by the upgraded TS diagnostic system with up to 12 spatial points. Each T_e profile shows a peak near the ECR layer, and the result agrees with that obtained in the previous study. Approximately 70 kA current drive was achieved by 300 kW/28 GHz ECW. Nevertheless, measured T_e and p_e were quite low, i.e., less than 10 eV and 1 Pa, respectively. Thus, plasma equilibrium similar to that in TST-2, where fast electrons are dominant, is suggested. CT injection experiments were performed in QUEST after a synchronization system had been developed. Time evolution of the n_e profile before and after the CT injection was measured for the first time, and core density increase was observed.

It is thought that the top-launch CCC antenna enables sufficient core absorption, higher plasma current, and central heating, but these are not observed in the preliminary experiments. This is probably because this antenna was designed by ray-tracing using GENRAY for plasmas generated by the outboard-launch antenna and such plasmas cannot be created by the top-launch antenna alone. Therefore, current ramp-up is expected by applying dual-antenna scheme. Additionally, in order to achieve further increment in LHW-driven plasma current, central heating by the use of EBW was considered. In a rough one dimensional calculation, it is expected that when X-mode ECW is injected from the low-field side at the midplane, the mode conversion efficiency (from ECW to EBW) can be as high as 50 %. The EBW is absorbed near the plasma center if magnetic field strength is selected so that ECR layer is located at the center.

In summary, high performance coaxial multi-pass TS diagnostic system was developed and the performance was evaluated by Raman scattering measurement. The HXR diagnostic system was developed and effective temperature of fast electrons and energy flux profile were obtained successfully in TST-2. Applying the developed high performance TS measurement system to LHW-driven ST plasmas in TST-2, the T_e and n_e profiles were measured for the first time. Here, no significant anisotropy was shown near the plasma center. As a result, it is suggested that plasma equilibrium is different from that in the conventional tokamaks, and minor fast electrons are dominant in the equilibrium. Similar equilibrium is obtained in QUEST. For detailed understanding of LHW-driven plasmas, it is necessary to establish a theory such as three-fluid axisymmetric equilibrium model [99].

Acknowledgments

This thesis was completed with help and advice from many people. Firstly, I would like to express my gratitude to my supervisor Associate Professor Akira Ejiri for his continuous support on my Ph.D study through five years at the university of Tokyo. I learned from him about many things that are necessary to be a good scientist. I would also like to offer my special thanks to Professor Yuichi Takase for his invaluable help and moral support. Thanks to this, I was able to enjoy Ph.D life among good colleagues. I would additionally like to thank Assistant Professor Naoto Tsujii for his technical help, that is, setup and guidance of various code modules including EFIT, GENRAY/CQL3D, IDL functions, and so on.

I would also like to extend my appreciation to members of Thomson scattering measurement team in TST-2 including the past members, Dr. Takashi Yamaguchi, Dr. Junichi Hiratsuka, Mr. Keishun Nakamura, Mr. Hiroto Homma, Mr. Kazuya Toida, Mr. Naoki Matsumoto, and Dr. Hiroshi Tojo at QST. Without their persistent help this thesis would not be possible. I would also like to thank the rest of members of the TST-2 team including the past members, Dr. Masateru Sonehara, Dr. Takahiro Shinya, Dr. Hirokazu Furui, Mr. Satoru Yajima, Mr. Yusuke Yoshida, Mr. Kenta Nakamura, Mr. Toshihiro Takeuchi, Mr. Wataru Takahashi, Mr. Hibiki Yamazaki, Mr. Akichika Kitayama, Mr. Akito Sato, Mr. Yuki Takei, Mr. Yoshiyuki Tajiri, and Dr. Roidl Benedikt.

I am very grateful to Professor Hideki Zushi, Professor Kazuaki Hanada, Professor Hiroshi Idei, Associate Professor Yoshihiko Nagashima, Assistant Professor Makoto Hasegawa, Dr. Takumi Onchi, all the members of QUEST team at Kyushu university, Associate Professor Naoyuki Fukumoto and Professor Masayoshi Nagata at university of Hyogo, for giving me many opportunities to carry out experiments in QUEST. I have also had the support and encouragement of Associate Professor Takuma Yamada, Assistant Professor Makoto Sasaki, and Dr. Osamu Watanabe at Kyushu University.

Assistant Professor Shuji Kamio at NIFS, Dr. Kotaro Yamasaki at Kyushu university, and the members of the UTST team, especially Mr. Takenori G Watanabe and Mr. Tomohiko Ushiki have helped and encouraged me throughout the Ph.D course.

Lastly, my deepest appreciation goes to my family for their continuous love and support. Without their encouragement, this thesis would not have materialized. Thank you.

This work was supported by JSPS Grant-in-Aid for Scientific Research (S) No. 21226021 and (DC2) No. 16J05471, by NIFS Collaborative Research Program Nos. NIFS14KOCR001 and NIFS12KUTR078, and by JSPS A3 Foresight Program ‘Innovative Tokamak Plasma Startup and Current Drive in Spherical Torus’.

Bibliography

[1] J. Wesson, *Tokamaks 3rd* Oxford Univ. Press, New York (2004).

[2] J. Citrin *et al.*, Nucl. Fusion **50**, 115007 (2010).

[3] R. C. Wolf *et al.*, Nucl. Fusion **41**, 1259 (2001).

[4] Y-K. M. Peng, Physics of Plasmas **7**, 1681 (2000).

[5] F. Troyon *et al.*, Plasma Phys. Control. Fusion **26**, 209 (1984).

[6] Jeffrey Freidberg, *Plasma Physics and Fusion Energy*, Cambridge Univ. Press, New York (2007).

[7] Y.R. Lin-Liu and R.D. Stambaugh, Nucl. Fusion **44**, 548 (2004).

[8] Y-K. M. Peng and D. J. Stickler, Nucl. Fusion **26**, 769 (1986).

[9] M. Greenwald, Nucl. Fusion **28**, 2199 (1988).

[10] D.A. Gates *et al.*, Nucl. Fusion **46**, S22 (2006).

[11] S. Kubo *et al.*, Phys. Rev. Lett. **50**, 25 (1983).

[12] A. Ando *et al.*, Nucl. Fusion **26**, 1 (1986).

[13] F. Jobes *et al.*, Phys. Rev. Lett. **52**, 12 (1984).

[14] Y. Takase *et al.*, J. Plasma Fusion Res. **78**, 8 (2002).

[15] S. Shiraiwa *et al.*, Phys. Rev. Lett. **92**, 3 (2004).

[16] M. Uchida *et al.*, J. Plasma Fusion Res. **80**, 2 (2004).

[17] T. Maekawa *et al.*, Nucl. Fusion **45**, 1439 (2005).

[18] M. Uchida *et al.*, Proc. 25th Inc. Conf. on Fusion Energy 2012, EX/P6-18 (2012).

[19] V. F. Shevchenko *et al.*, Nucl. Fusion **50**, 5 (2010).

[20] V. F. Shevchenko *et al.*, EPJ Web of Conferences **87**, 02007 (2015).

[21] K. Hanada *et al.*, Plasma Fusion Res. **5**, S1007 (2010).

[22] H. Zushi *et al.*, Proc. 25th Inc. Conf. on Fusion Energy 2012, EX/P2-14 (2012).

[23] H. Idei *et al.*, Proc. 25th Inc. Conf. on Fusion Energy 2014, EX/P1-38 (2014).

[24] M. Ishiguro *et al.*, J. Phys. Conf. Ser. **511**, 012041 (2014).

[25] S. Tashima *et al.*, Nucl. Fusion **54**, 023010 (2014).

[26] Y. Takase *et al.*, Nucl. Fusion **53**, 063006 (2013).

[27] T. Shinya *et al.*, Nucl. Fusion **55**, 073003 (2015).

[28] V.V. D'yachenko *et al.*, Plasma Phys. Rep. **39**, 189 (2013).

[29] V.K. Gusev *et al.*, Nucl. Fusion **55**, 104016 (2015).

[30] H. Tanabe *et al.*, Phys. Rev. Lett. **115**, 215004 (2015).

[31] T. Yamada *et al.*, Plasma Fusion Res. **5**, S2100 (2010).

[32] R. Raman *et al.*, Nucl. Fusion **47**, 792 (2007).

[33] K. Tobita *et al.*, JAEA-Research 2010-019, (2010).

[34] K. Tobita *et al.*, Nucl. Fusion **47**, 892 (2007).

[35] S. Kainaga, Doctoral Thesis, Graduate School of Science, Univ. of Tokyo (2008).

[36] S. Kainaga *et al.*, Plasma Fusion Res. **3**, 027 (2008).

[37] T. Yamaguchi *et al.*, Plasma Fusion Res. **5**, S2092 (2010).

[38] J. Hiratsuka, Doctoral Thesis, Graduate School of Science, Univ. of Tokyo (2013).

[39] T. Yamaguchi, Doctoral Thesis, Graduate School of Frontier Sciences, Univ. of Tokyo (2015).

[40] H. Homma, Master Thesis, Graduate School of Frontier Sciences, Univ. of Tokyo (2016).

[41] R. J. Goldston and R. H. Rutherford, *Plasma Physics*, Institute of Physics Publishing (1995).

[42] T. Matoba *et al.*, Jpn. J. Appl. Phys. **18**, 1127 (1979).

[43] N. J. Peacock *et al.*, Nature **224**, 488 (1969).

[44] K. J. Gibson *et al.*, Plasma Phys. Control. Fusion **52**, 124041 (2010).

[45] H. Salzmann *et al..*, Rev. Sci. Instrum. **59**, 1451 (1988).

[46] T. N. Carlstrom *et al.*, Rev. Sci. Instrum. **63**, 4901 (1992).

[47] A. Ejiri *et al.*, Plasma Fusion Res. **5**, S2082 (2010).

[48] H. Togashi *et al.*, JINST **10**, C12020 (2015).

[49] C.M. Penny *et al.*, Opt. Spc. Am. **64**, 712 (1974).

[50] I. Yamada, K. Narihara, and H. Hayashi, Rev. Sci. Instrum. **74**, 1675 (2003).

[51] C. M. Penney, J. Opt. Soc. Am. **59**, 34 (1969).

[52] S.C. McCool *et al.*, Report No. DOE/ET/53042-7, FRCR 234, University of Texas (1981).

[53] Exelis Visual Information Solutions, Inc. (http://www.harrisgeospatial.com).

[54] M. Yu. Kantor *et al.*, Rev. Sci. Instrum. **72**, 1159 (2001).

[55] M. Yu. Kantor *et al.*, Plasma Phys. Control. Fusion **51**, 055002 (2009).

[56] A. H. Morton, Appl. Opt. **16**, 1588 (1977)

[57] T. Hatae *et al.*, Rev. Sci. Instrum. **83**, 10E344 (2012).

[58] R. Yasuhara *et al.*, Rev. Sci. Instrum. **83**, 10E326 (2012).

[59] M. Yoshikawa *et al.*, Plasma Fusion Res. **8**, 1205169 (2013).

[60] H. Togashi, Master Thesis, Graduate School of Frontier Sciences, Univ. of Tokyo (2014).

[61] H. Togashi *et al.*, Plasma Fusion Res. **9**, 1202005 (2014).

[62] H. Togashi *et al.*, Rev. Sci. Instrum. **85**, 11D846 (2014).

[63] H. Togashi *et al.*, Rev. Sci. Instrum. **85**, 056103 (2014).

[64] J. Hiratsuka *et al.*, Plasma Fusion Res. **6**, 1202133 (2011).

[65] J. Hiratsuka *et al.*, Plasma Fusion Res. **7**, 2402092 (2012).

[66] J. Hiratsuka *et al.*, Plasma Fusion Res. **10**, 1402007 (2015).

[67] H. Tojo *et al.*, Plasma Fusion Res. **6**, 1302018 (2011).

[68] H. Tojo *et al.*, Journal of Instrumentation **7**, C05004 (2012).

[69] H. Tojo *et al.*, Journal of Instrumentation **7**, P04005 (2012).

[70] H. Tojo *et al.*, Rev. Sci. Instrum. **85**, 11D865 (2014).

[71] I.H. Hutchinson, *Principles of Plasma Diagnostics*, Cambridge Univ. Press, New York (2005).

[72] K. Ogura *et al.*, J. Phys. Soc. Jpn **55**, 1 (1986).

[73] S. Texter *et al.*, Nucl. Fusion **26**, 10 (1986).

[74] G.M. Wallace *et al.*, Nucl. Fusion **51**, 083032 (2011).

[75] S. Muto *et al.*, Rev. Sci. Instrum. **74**, 1993 (2013).

[76] W. W. Heidbrink, Rev. Sci. Instrum. **57**, 1769 (1986).

[77] N. Pu *et al.*, Journal of Instrumentation **10**, P12013 (2015).

[78] Y. Takase *et al.*, Nucl. Fusion **41**, 1543 (2001).

[79] L.L. Lao *et al.*, Nucl. Fusion **25**, 11 (1985).

[80] D. Johnson *et al.*, Rev. Sci. Instrum. **70**, 776 (1999).

[81] C. J. Barth *et al.*, Rev. Sci. Instrum. **72**, 1138 (2001).

[82] R. Scannell *et al.*, Rev. Sci. Instrum. **79**, 10E730 (2008).

[83] T. Shinya, Doctoral Thesis, Graduate School of Frontier Sciences, Univ. of Tokyo (2016).

[84] T. Shinya *et al.*, Plasma Fusion Res. **9**, 1202133 (2014).

[85] T. Shinya *et al.*, Nucl. Fusion **57**, 036006 (2016).

[86] S. Tsuda *et al.*, Plasma Fusion Res. **10**, 1202064 (2015).

[87] H. Togashi *et al.*, Plasma Fusion Res. **10**, 1202082 (2015).

[88] K. Mishra *et al.*, Nucl. Fusion **55**, 083009 (2015).

[89] T. Yamaguchi *et al.*, Plasma Fusion Res. **8**, 1302001 (2013).

[90] S.A. Sabbagh *et al.*, Phys. Fluids B **3**, 2277 (1991).

[91] C. Xiao *et al.*, Phys. Plasmas **11**, 4041 (2004).

[92] M. Nagata *et al.*, Nucl. Fusion **45**, 9 (2005).

[93] P.C. de Vries *et al.*., Plasma Phys. Control. Fusion **54**, 124032 (2012).

[94] T. Takeuchi, Master Thesis, Graduate School of Science, Univ. of Tokyo (2016).

[95] S. Yajima, Master Thesis, Graduate School of Science, Univ. of Tokyo (2016).

[96] K Ushigusa, Plasma Phys. Control. Fusion **38**, 1825 (1996).

[97] H.P. Laqua, Plasma Phys. Control. Fusion **49**, R1(2007).

[98] T.H. Stix, *Waves in plasmas*, AIP, New York (1992).

[99] A. Ishida *et al.*, Plasma Fusion Res. **10**, 1403084 (2015).

Appendices

A TS measurements for Ohmically heated plasmas in TST-2

TS measurements for TST-2 Ohmically heated plasmas have been performed [37]. More detailed time evolution of the profiles was measured in the present experiments. Particularly, the improved detection circuit enables us to measure lower density plasmas. Reliability of the TS diagnostics and the EFIT code was also investigated.

Firstly, single pass TS measurements were performed in 14 reproducible plasma discharges as shown in Fig. A.1. 10 spatial points were measured at 7 timings. Figure A.2 shows the result. The plasma current and the line-integrated density start to increase rapidly just after t = 16 ms. Hollow profiles of n_e, T_e, and p_e are shown at t = 17 ms. Plasma current continues to increase and the shape of n_e profile changes from a hollow profile to peaked one, while T_e keeps the hollow profile until t = 21 ms. Such a hollow profile in T_e implies that the toroidal current is firstly formed as a skin current, and then diffuses into the plasma. High temperatures after t = 21 ms in the TS measurements are consistent with the decrease of the H_α radiation and the increase of the SBD signal with the polypropylene film. The purple vertical lines in Fig. A.2 show magnetic axes calculated by the EFIT code. In a plasma equilibrium state, magnetic surfaces surrounding the center called the magnetic axis are formed, and the values of n_e, T_e, and p_e are constant on each surface. It can be seen that the center positions indicated by each profile agree with the magnetic axis positions calculated from the EFIT code. Figure A.3 shows the magnetic surfaces in a Ohmically heated plasma calculated from the EFIT code. The profiles at t = 25 ms are plotted as a function of normalized minor radius ρ in Fig. A.4. Here, ρ is the radius normalized by the minor radius, and it is a label to define each flux surface. Black curve in Fig. A.4 shows the total pressure calculated from the EFIT code.

It should be noted that the absolute density calibrated by the Raman scattering measurement is 2–2.5 times lower than that estimated from the line integrated density measured by an interferometer. Although the reason is not clear, all the absolute values of the electron density used in this study are adjusted by a factor, so that the line integrated densities agree with that measured by the interferometer.

Secondary, the coaxial double-pass system, which has been developed in this study, was applied to the TS measurement. In the normal operations in TST-2, the plasma current flows clockwise when it is viewed from the top, and thus the (blue shifted) velocity distribution function measured in the backward path in the double-pass TS scheme is the components contributing to the plasma current. In the past, (non-coaxial) double-pass TS measurements were performed for Ohmically heated plasmas with the plasma current of around 100 kA. Two spatial points: one in the plasma edge (R = 220 mm) and another in the core (R = 389 mm) were selected in the study, and then anisotropies of around 50 percents for the edge and

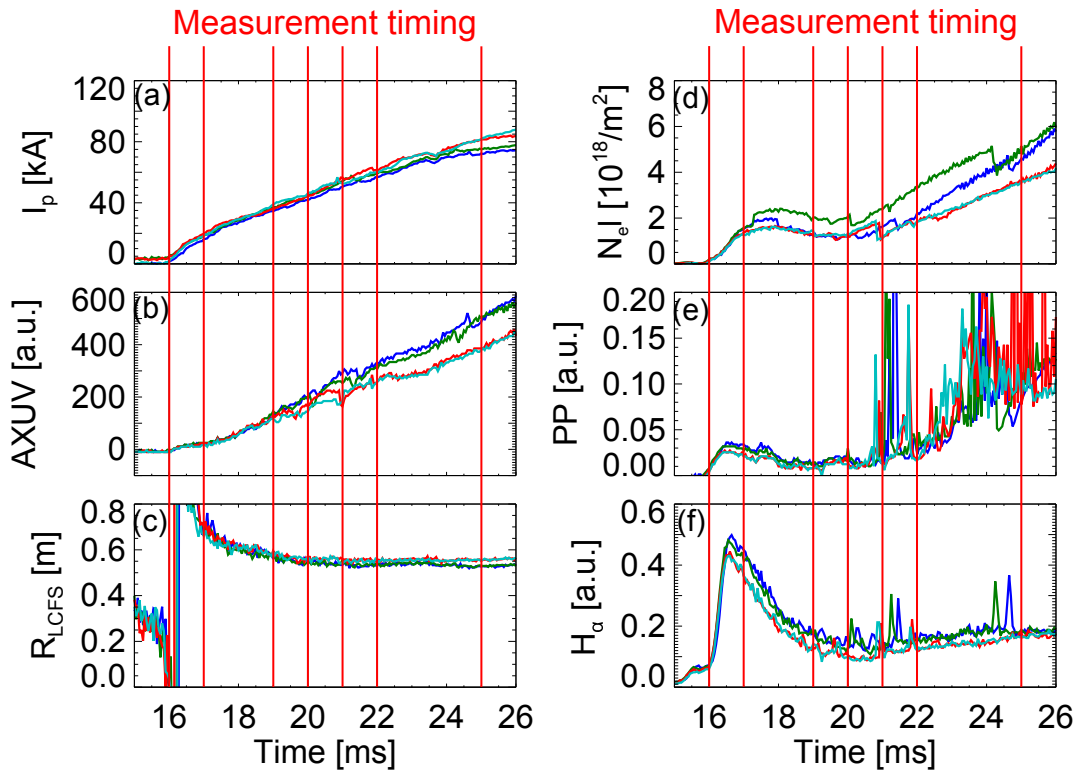

Fig. A.1: Waveforms of discharges for Ohmically heated plasmas, where single pass TS measurements are performed: plasma currents (a), AXUV signals (b), radii of the LCFS at the midplane (c), line-integrated densities at the midplane (d), SBD signals with thin films of polypropylene (e), signals of H_α radiation (f). Vertical red lines show the TS measurement timings.

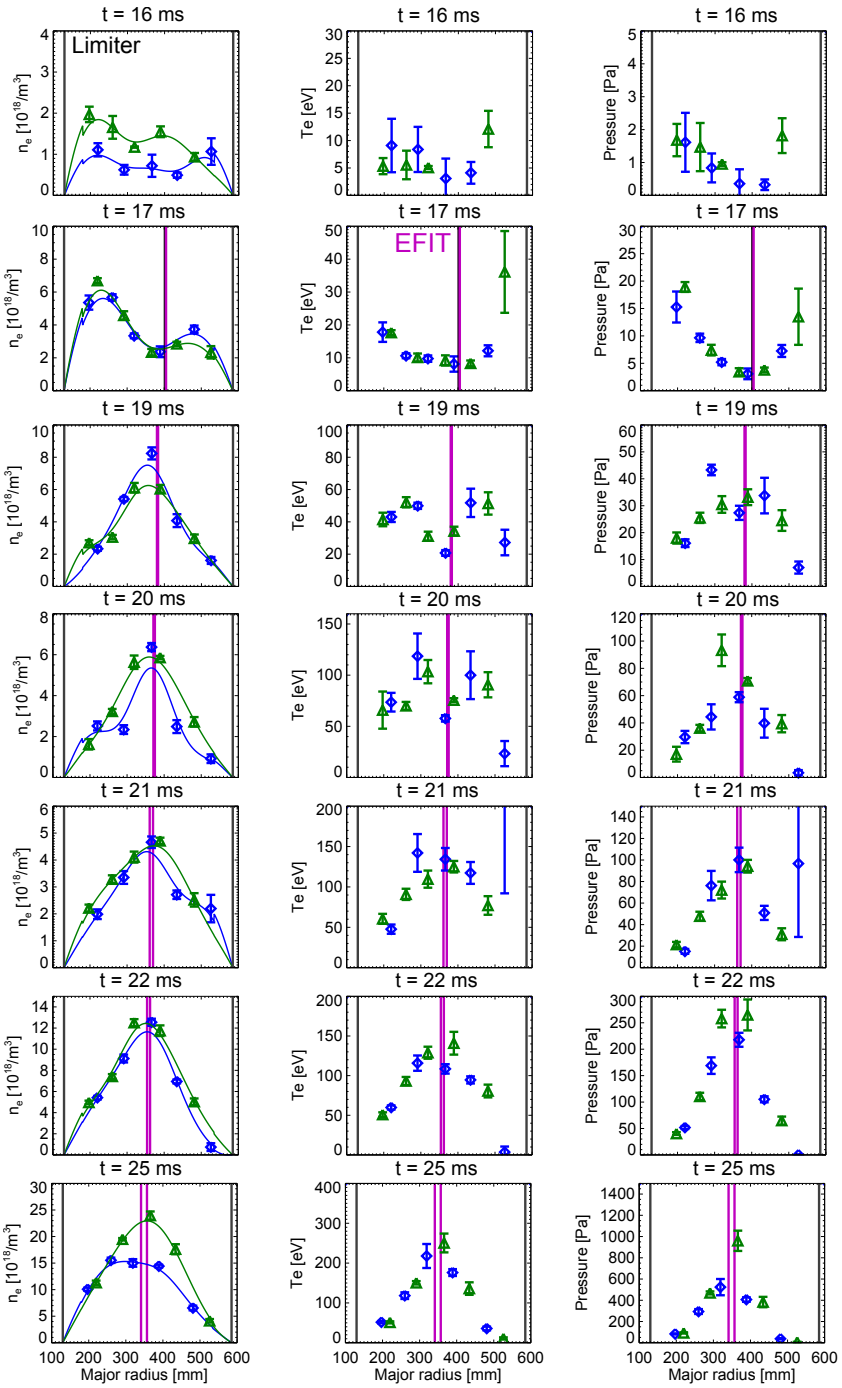

Fig. A.2: Time evolution of profiles of the electron density (left), temperature (center), and pressure (right). Different colors (green and blue) indicate the difference of discharges, because we can measure 5 of 10 spatial points simultaneously. Purple vertical lines show magnetic axes calculated by the EFIT code.

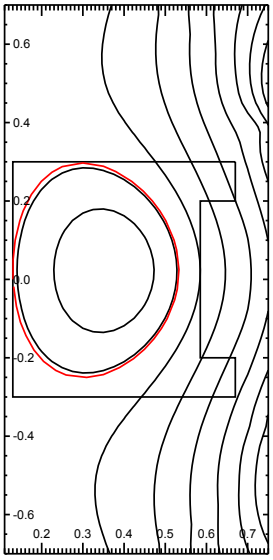

Fig. A.3: Contour of magnetic surfaces calculated by the EFIT code for a TST-2 Ohmically heated plasma at t = 25 ms. The red ellipse represents the LCFS.

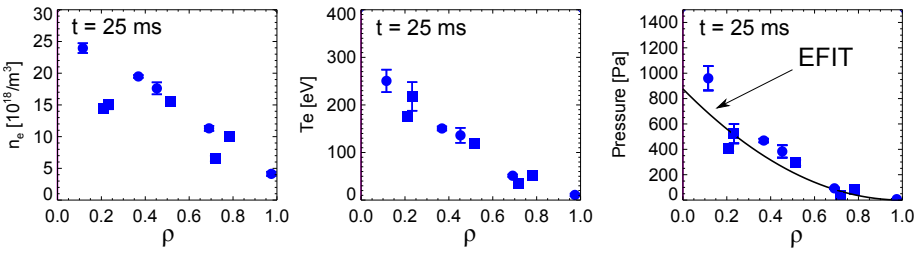

Fig. A.4: Profiles of the electron density (left), temperature (center), and pressure (right) at t = 25 ms as a function of a normalized minor radius ρ. The black curve in the right figure shows the pressure profile calculated by the EFIT code.

several percents for the center were found [66]. In almost all the measurements, the electron temperature in current contributing side was higher than that the opposite side.

Figure A.5 show results of the coaxial double-pass TS measurements for the Ohmically heated plasmas similar to that shown in Fig. A.1. It can be seen that the temperature of the parallel components (green symbols) is higher than that of the perpendicular components (blue symbols). This feature is the same as that shown in the past experiments using the non-coaxial double-pass scheme.

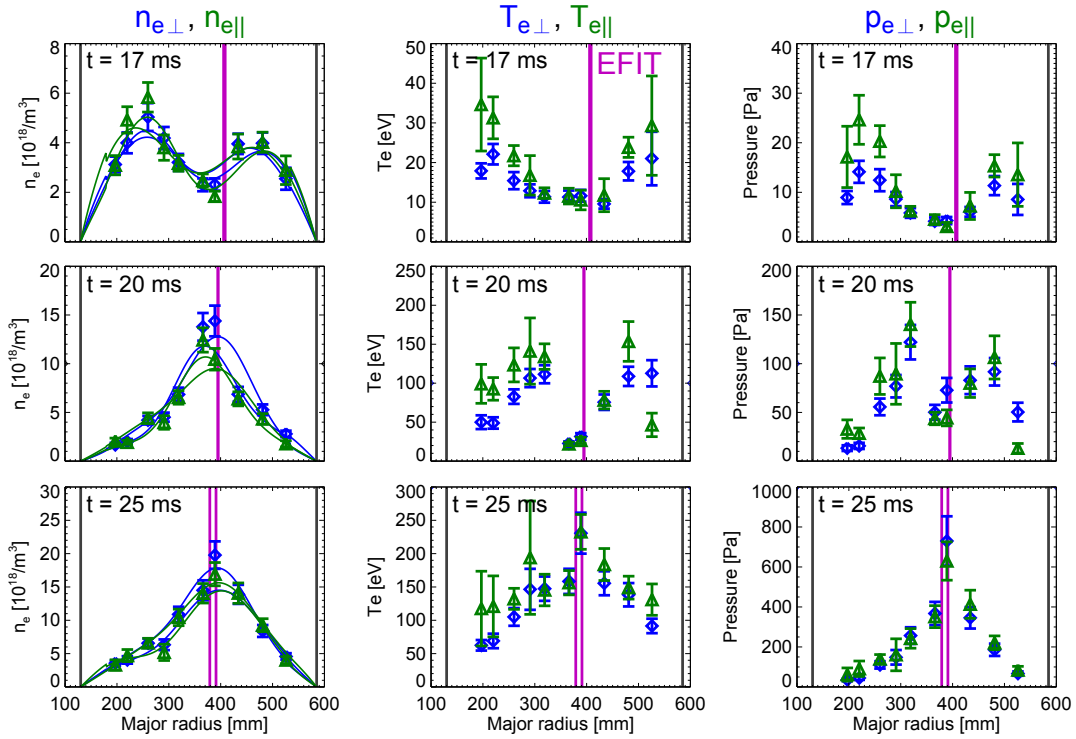

Fig. A.5: Time evolution of profiles of the electron density (left), temperature (center), and pressure (right) obtained by the coaxial double-pass TS measurements. Blue and green symbols in each figure represent the values obtained in the forward and backward paths in the double-pass TS scheme, which measures the distribution functions perpendicular and parallel to the electrons carrying the plasma current, respectively. Purple vertical lines indicate magnetic axes calculated by the EFIT code.

B Non-inductively driven plasmas by LHW using outboard-launch CCC antenna with I_p = 5 kA

Single pass TS measurements were performed for TST-2 plasmas sustained by lower hybrid waves excited using the outboard-launch CCC antenna alone [87]. In order to improve the signal-to-noise ratio in the TS measurement for such low-density plasmas, multiple TS signals obtained from reproducible discharges were averaged. Waveforms of the discharges are shown in Fig. B.6. A 2 kW/2.45 GHz ECW is injected for plasma ignition, and the plasma current is started-up and sustained by a 20 kW/200 MHz LHW. The plasma current

I_p increases up to approximately 5 kA. The line-integrated density $n_e l$ obtained by interferometry is approximately 1.3×10^{18} m^{-2} ($l \sim 0.45$ m) and that is several tens of times lower than that for the Ohmically heated plasmas such as that shown in Fig. A.1. The traces of I_ps and radiation signals indicates good reproducibility. Since the plasmas at $t = 85$ ms seem to be stable, TS measurements (laser firings) were performed at this timing. 10 plasma discharges enable us to perform 10 TS measurements with 4 spatial points, and the obtained TS signals for each point were averaged. Similar measurements were performed for another set of spatial points, and then a profile with total 8 spatial points was obtained. Note that old-type APDs with lower sensitivity (S8890-30) were used in the experiments.

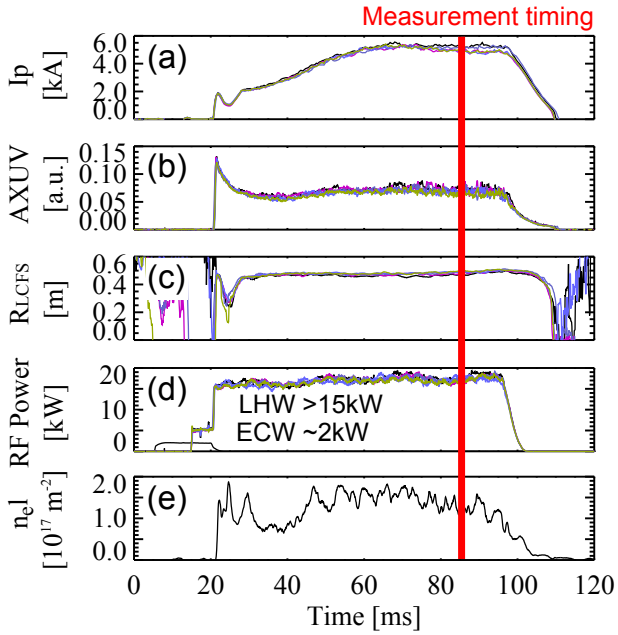

Fig. B.6: Waveforms of plasma currents (a), AXUV signals (b), outboard radii of the LCFS (c), and LHW and ECW injected powers (d) for 5 discharges. (f) shows a typical line-integrated density at the midplane.

Figure B.7 shows TS signals at $R = 342$ mm averaged over 10 TS signals. Here, the background including the stray light was subtracted. Since the stray light at this point is quite small, clear peaks in the three wavelength channels close to the YAG wavelength of 1064 nm can be seen. The signals are fitted well to a Maxwellian distribution function. Resultant profiles for T_e and n_e are shown in Fig. B.8. Note that one spatial point ($R = 459$ mm) is significantly affected by the stray light and the results are not shown. T_e values in the central region are under 10 eV and the profile is hollow, while n_e shows a bell-shaped profile with a peak value of $n_e \sim 6 \times 10^{17}$ m^{-3} near $R = 342$ mm. Purple vertical lines in the figure show the magnetic axes obtained from the EFIT code. Unlike results in the Ohmic plasma experiments, each center position estimated from the profile seems to be located slightly inner side compared with the magnetic axis.

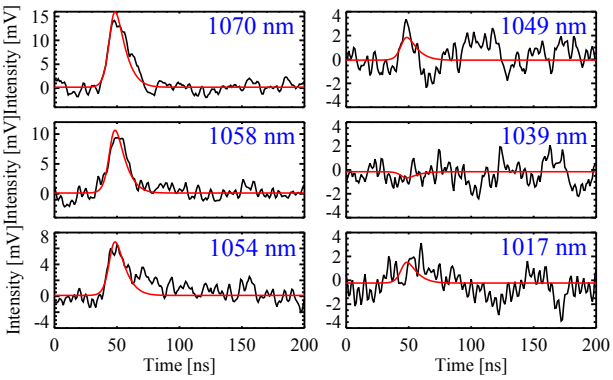

Fig. B.7: TS signals and the fittings at R = 342 mm. The center wavelength of the transmission band of each interference filter is printed in blue [87].

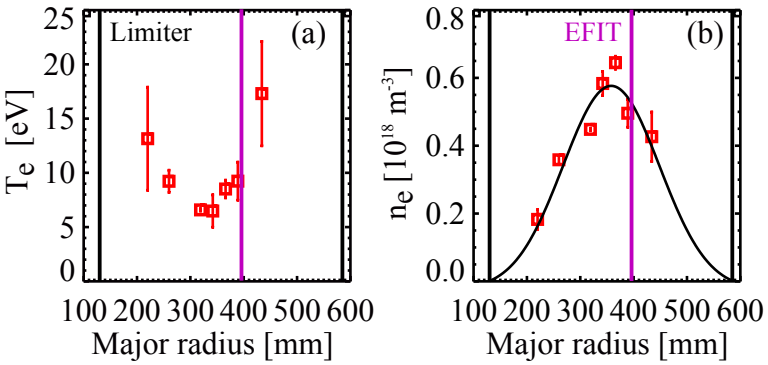

Fig. B.8: Profiles of electron temperature T_e (a) and electron density n_e (b) are plotted in red open squares. Black lines represent the inboard and outboard limiter positions and purple lines show the magnetic axes obtained from the EFIT code. The solid curve in (b) shows a Gaussian fit.